BIOS Lab on a Chip group

UNIVERSITY OF TWENTE.

Master Thesis

Microfluidic pump based on arrays of rotating magnetic microspheres

Archive number: 2012-1
May 2012

Wesley van den Beld
Master Electrical Engineering
Microsystems and Microelectronics
EEMCS, University of Twente

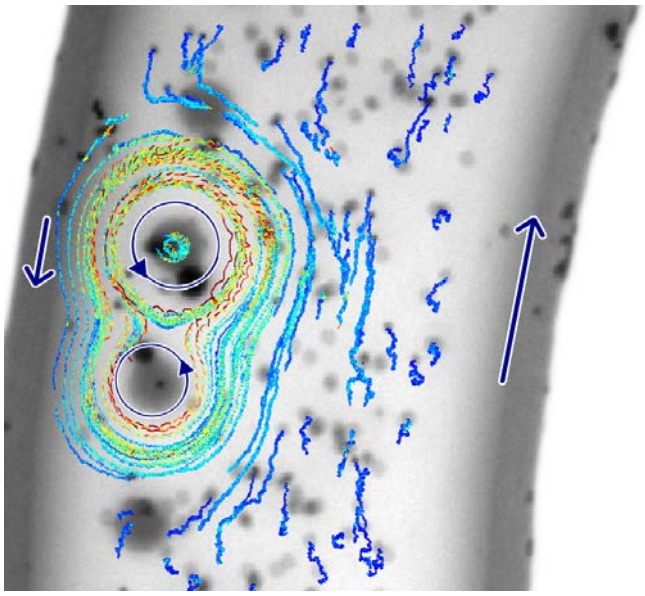

Graduation committee:
Prof.Dr. Jan C.T. Eijkel
Dr.Ir. Leon Abelmann
Ir. Eddy L. de Weerd
Dr. Devaraj van der Meer

Voorwoord

Dit is het verslag van mijn afstudeeropdracht bij BIOS, de lab-on-a-chip vakgroep van de Universiteit Twente. Deze opdracht is het afsluitende onderdeel van mijn master Electrical Engineering. In 2010 vond een exploratieve opdracht plaats naar roterende magnetische bolletjes. Naar aanleiding van de resultaten hiervan is in overleg met Jan Eijkel deze afstudeeropdracht tot stand gekomen. Een nieuwe manier wordt onderzocht om vloeistof in microkanalen te pompen. Het pompen gebeurt met behulp van roterende magnetische microbolletjes rond een reeks magnetische schijfjes.

Graag bedank ik Jan Eijkel voor de mogelijkheid om af te studeren bij de BIOS-groep en tevens voor de vrijheid die ik gekregen heb binnen het samenstellen en uitvoeren van de opdracht. Ook voor de prettige begeleiding waaronder de wekelijkse gesprekken gedurende de gehele afstudeeropdracht, en omdat ik altijd binnen kon lopen om vragen te stellen. Ook bedank ik graag Eddy de Weerd, Leon Abelmann en Devaraj van der Meer voor het deelnemen in mijn afstudeercommissie en voor de discussies. Daarnaast bedank ik graag Albert van den Berg voor het mogelijk maken van mijn afstuderen bij BIOS.

Voor de technische ondersteuning bedank ik als eerste Johan Bomer, hij heeft alle chips geproduceerd rekening houdend met alle besproken specificaties. Ik bedank ook Jan van Nieuwkasteele, Hans de Boer en Paul ter Braak voor de chipholder en alle andere technische ondersteuning. Daarnaast bedank ik graag Thijs Bolhuis voor alle ondersteuning bij alle metingen met de VSM, het lenen van de quadrupole en de kepco. Ook bedank ik Marcel Schwirtz voor het lenen van de tweede kepco. Verena Stimberg bedank ik voor het uitleggen en voordoen van het lijmen van de chips.

Alle medestudenten bedank ik voor de gezelligheid en goede sfeer, in het bijzonder mijn buurvrouw Annemarie voor de nodige afleiding tussen het harde werken door. Ik bedank de gehele BIOS-groep voor de discussies en de leuke periode tijdens mijn afstuderen. Tenslotte bedank ik mijn flatgenoten, vrienden en familie voor alle ondersteuning en afleiding tijdens mijn afstuderen.

Abstract

Microfluidic pump based on arrays of rotating magnetic microspheres

We demonstrate a novel, flexible and biocompatible method to pump liquid through microchannels without the use of an external pump. The pumping principle is based on the rotation of superparamagnetic microspheres around permalloy disks, driven by an external in-plane rotating magnetic field. By placing the permalloy disks close to the edge of the channel, a net flow of 9 um/s was generated in the middle of the channel. A possible use of this pumping principle could be to recirculate the medium of a cell culture chamber, which will create new possibilities for closed cell culturing systems on chip with controllable flow rates [23].

The principle of controllable movement and positioning of magnetic particles using permalloy patterns has been demonstrated by Gunnarsson et al [20]. We apply this technique to rotate magnetic microspheres around an array of permalloy disks, positioned close to the edge of a circular microfluidic channel. Due to their position near the edge of the channel, the drag caused by the channel wall will cause an asymmetry in liquid displacement, resulting in a net pumping motion (Figure 1). The effect is multiplied by using an array of magnetic disks.

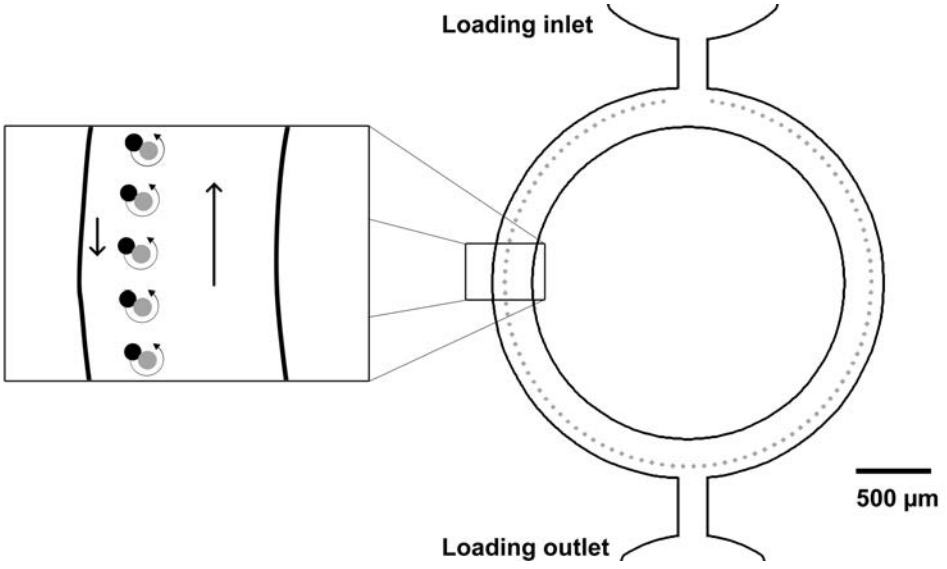

Figure 1: The closed pumping channel with permalloy disks (gray) and magnetic microspheres (black). The arrows indicate the direction of flow. Since the disks are placed closed to the edge of the channel, the net flow is upwards.

To fabricate the structure a 480 nm permalloy film was sputtered on a silicon wafer and patterned using conventional lithography and etching, yielding an array of disks with a diameter of 25 μm. The 37 μm deep microchannels were wet etched in a borofloat glass wafer. To get tightly sealed channels, both wafers are bonded anodically at 425 ^{o}C. The disadvantage of this heating step is that it increases the coercivity of the permalloy (Figure 2). However the hysteresis loop of the permalloy film after heating (Figure 2, left), shows that the increase in coercivity is limited to 6 $\frac{kA}{m}$, which can still be easily reached with conventional electromagnets.

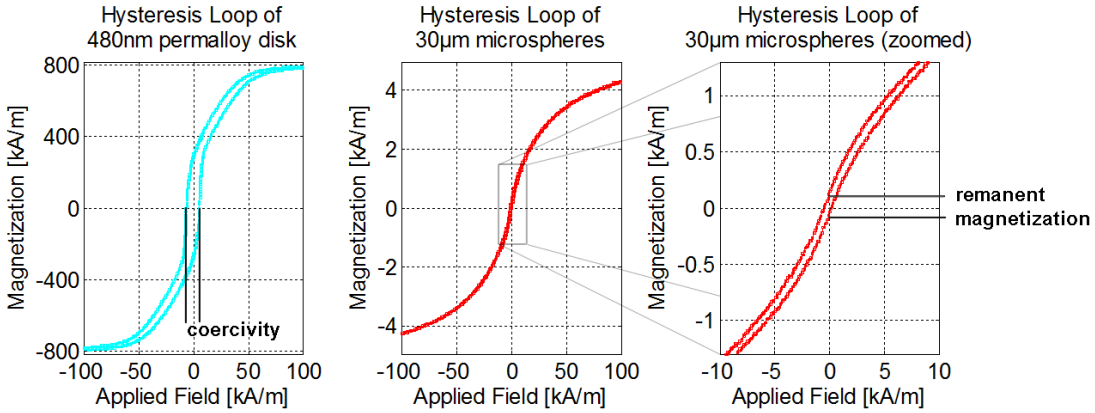

Figure 2: The magnetization curves of the permalloy disks (left) and the superparamagnetic microspheres (middle and right). The remanent magnetization of the magnetic microspheres is small.

Pumping experiments were performed using biocompatible, 30 μm superparamagnetic microspheres [33]. Their hysteresis loop (Figure 2, right) shows that the remanent magnetization of the microspheres is very small, which will prevent permanent sticking of the particles to the disk or each other. The external magnetic field was generated by a magnetic quadrupole electromagnet, with a field of 95 $\frac{kA}{m}$ at rotating frequencies of up to 10 Hz. Red polystyrene microspheres of 3 μm [38] were added to visualize the flow in a microscope.

The rotation frequency of the microphores could be controlled well up to 6 Hz, resulting in a maximum microsphere velocity of 470 $\frac{\mu m}{s}$. Above this frequency the microspheres do not perform exclusively a circular motion but also spin around their own axis or stop moving completely. Even though coverage of the disks by beads was only partial in our setup, the pumping principle works well. Figure 3 shows an analysis of the recorded paths of the indicator microphores. There is a net flow in the middle of the channel with an average velocity of 9 $\frac{\mu m}{s}$. We expect that further optimization of the geometry and microsphere coverage can lead to a significant increase of the flow rate.

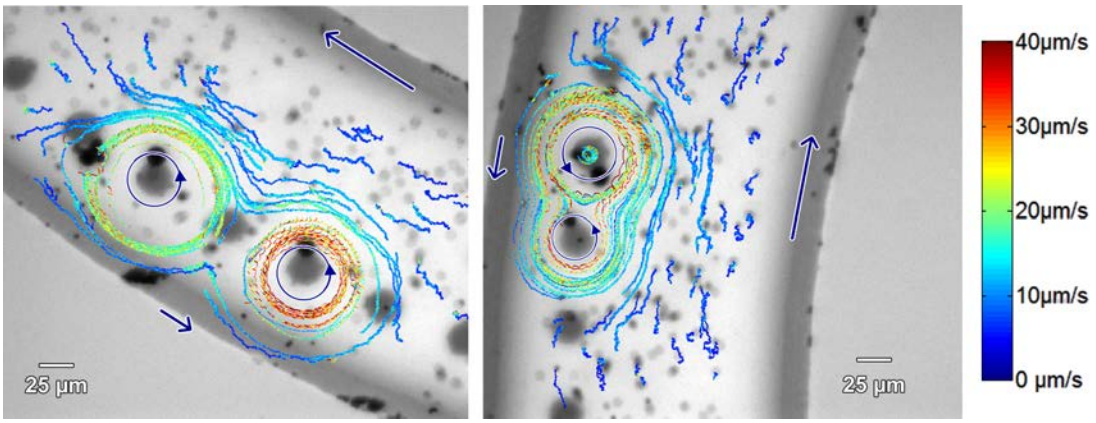

Figure 3: The observed movement of the indicator microspheres at magnetic field frequency of 5 Hz, indicating a net liquid flow in the channels. The maximum velocity of 40 m/s is limited by the particle tracking algorithm.

List of abbreviations and constants

Abbreviations

Abbreviations	Description
BIOS	Biomedical and Environmental Sensor systems
BSA	Bovine serum albumin
IPA	Iso-Propyl Alcohol
LOC	Lab on a chip
MESA+	Nanotechnology Research institute of University of Twente
NOA	Norland Optical Adhesives
PCR	Polymerase chain reaction
TST	Transducers Science and Technology
UV	Ultraviolet
VSM	Vibrating Sample Magnetometer

Constants

Constant	Description	Value	Unit
ϵ_0	Vacuum permittivity	8.85×10^{-12}	F/m
μ_0	Vacuum permeability	$4\pi \times 10^{-7}$	N/A^{-2}
c	Speed of light	3×10^8	m/s
η_w	Viscosity of water	10^{-3}	$kg/m\ s$

Symbols

Symbol	Description	Unit
ϵ_0	Vacuum permittivity	F/m
μ_0	Vacuum permeability	N/A^2
F	Mechanical force	N
B	Magnetic induction	T
H	Magnetic field	A/m
H_c	Magnetic coercivity	A/m
M	Magnetization	A/m
M_s	Saturation magnetization	A/m
μ	Permeability of a medium	-
μ_r	Relative permeability of a medium	-
χ	Magnetic susceptibility	-
I	Electrical current	A
ρ_m	Magnetic field volume charge density	A/m^2
ρ_s	Magnetic field surface charge density	A/m^2
q_m	Magnetic point charge	$A \cdot m$
m	Dipole moment	$A \cdot m^2$
r	Displacement vector	m
A	Surface area	m^2
h	Height	m
l	Length	m
w	Width	m
N	Number of turns	-

Symbol	Description	Unit
Re	Reynolds number	-
ρ_f	Fluid density	kg/m^3
u	Fluid velocity	m/s
η	Viscosity	$kg/m \cdot s$
p	Pressure	Pa
R	Radius	m

Contents

Chapter 1

Aim and thesis outline

In this thesis a study is performed on the feasibility of pumping liquid in microchannels with use of arrays of rotating magnetic beads. Magnetic microspheres (also called beads) are rotated using an external in-plane rotating magnetic field. Fluid is pumped in a closed system without the use of external tubing, which reduces the size of the microfluidic control drastically. This new pumping method creates new opportunities for an easy to use and programmable pumping operation as part of a new pumping platform.

1.1 New pumping platform

A microfluidic platform provides a set of fluidic operations, which are designed for easy combination within a well-defined fabrication technology. A microfluidic platform creates a generic and consistent way for miniaturization, integration, automation and parallelization of (bio-)chemical processes like on-chip PCR. Microfluidic structures may be employed to manipulate the cellular microenvironment in order to improve the understanding of cell biology or to build and mimic cellular models and assays. A microfluidic unit operation is a basic functionality in a fluidic system, for example pumping and mixing. A microfluidic platform should offer a number of microfluidic unit operations that can be combined easily with existing methods to enable quick implementation. The platform does not need to provide a complete set of all the unit operations, it is far more important that the different elements are connectable by a well-defined interconnection process. Automation and portability combined with a large set of unit operations may create new opportunities for the implementation of analyses on chip. [30, 32]

This thesis focuses on microfluidic pumping with rotating magnetic beads, and the unit operation pumping of this novel fluidic pumping platform is studied. Applying a low flow rate is useful for revealing cell or bacteria dynamics, which generate for example concentration gradients. Cells depend on constant transport and exchange of oxygen and carbon dioxide [30]. In the system furthermore effective mixing is performed by the stirring action of the beads, which is a more effective way than only diffusive mixing. The possibility of valving should theoretically also be possible by creating locally a strong magnetic field which accumulates magnetic beads. However this unit operation valving is not investigated in this thesis.

The fluidic pumping operation is based on the asymmetry in the volume displacement of the forward and backward stroke of the magnetic beads, which causes a net pumping motion as shown in Figure 1.1. The rotational frequency of the external magnetic field controls the movement of the magnetic beads and therefore the generated net fluid flow. This principle creates the possibility of an external programmable flow in a closed microfluidic system, which could be integrated into an automated platform for biochemical analysis [32]. The advantage of such a magnetic actuation is furthermore that it reduces the size of the microfluidic control drastically, because during the pumping no tubing or syringe pump is required. The total setup can be reduced to the chip in a chipholder and a magnetic control device, hence a small portable programmable pumping system with an inexpensive driving setup is obtained. With

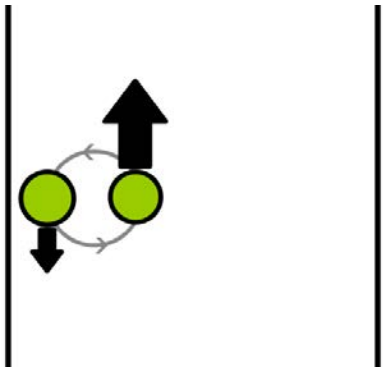

Figure 1.1: The asymmetric bead setup, the stroke in the middle of the channel displaces more fluid than the stroke near the wall.

an external pump connected to a chip by tubing, problems with air bubbles and dead volume are often experienced. These can be circumvented be using a closed fluidic pump on chip.

1.1.1 Previous studies

A number of studies in the field of pumping with rotating beads around their axis have been performed. A possible method is where the bead is trapped and rotated optically or magnetically, which causes a fluid flow. A method for generating flow within a microfluidic channel using an optically driven pump is shown in ref. [26]. The pump consists of two counter rotating particles trapped and driven by optical tweezers. The particles were 6 μm in diameter and rotated with 9 Hz in a 15 μm deep channel. The traced path of a 1 μm silica particle is shown in Figure 1.2, a net flow of 8 $\mu m/s$ is generated.

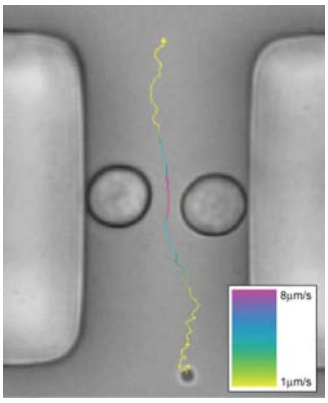

Figure 1.2: The traced path of the particle is drawn, due to the pumping effect it first accelerates and then decelerates through the channel. [26]

Also the controlled displacement of magnetic beads in microchannels (without explicit pumping action) is investigated in different studies. Magnetic beads can be moved in a microchannel using for example an external permanent magnet or coils on chip [37, 40]. Another option is the use of magnetic elements which deform an external magnetic field. An example of this method is programmable motion of single magnetic particles on patterned magnetic surfaces [20].

Permalloy ellipses with a thickness of 0.1 μm are exposed to in-plane magnetic fields. The net magnetization of the elements will rotate in-plane, following the external magnetic field. The stray field of the nearly saturated ellipses attracts the magnetic particles, causing the beads to move as shown in Figure 1.3.

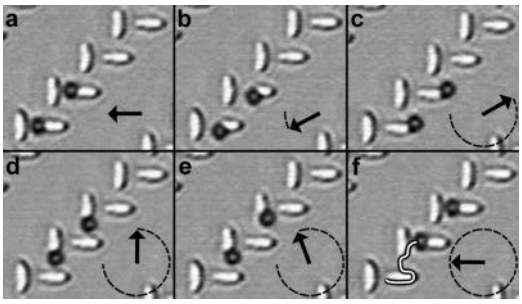

Figure 1.3: The external in-plane magnetic field is rotated which magnetizes the ellipses, attracting the magnetic particle (diameter of 2.8 μm). [20]

1.2 Objective and general approach

In this study both concepts are combined, magnetic beads are circulating around a soft magnetic material controlled by an externally created rotating magnetic field causing a net fluid flow, as shown in Figure 1.4. The soft magnetic disks are placed near the wall of the channel, causing an asymmetry in the volume displacement of the rotating beads. In the middle of the channel more liquid is displaced than near the wall, which generates a net fluid flow. A rendered image of the magnetic bead in the microchannel is shown in Figure 1.5.

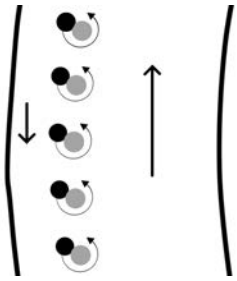

Figure 1.4: The pumping principle with the fluid flow and the rotational movement of the bead around the disks indicated.

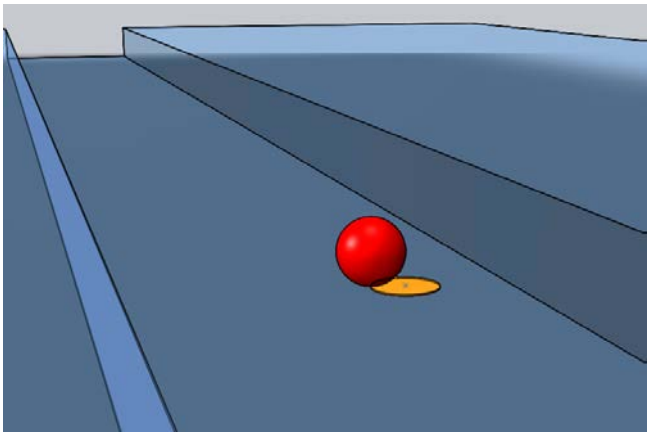

Figure 1.5: A magnetic bead (red) near a magnetic disk (yellow) in the microchannel.

The objective is to investigate whether it is possible to generate a significant net fluid flow using an array of rotating magnetic beads. Using an external rotating in-plane magnetic field the magnetic elements of the array are magnetized, causing a force on the magnetic beads. Calculations and simulations are performed to give some predictions about the net fluid flow

and pumping profile. Experiments with self-designed chips are performed to show whether it is possible to generate a net fluid flow using this principle.

A literature research on the controlled movement of magnetic beads and pumping with the use of rotating beads was performed. With the obtained knowledge a chip was designed to test the feasibility of the pumping principle. With the manufactured chip some experiments were carried out, first with a self-build controlling and amplification circuit. Later on larger setup was used to have better control and a wider range for the magnetic field. Also the magnetic properties of the used magnetic materials were studied using VSM measurements, to relate the performance in the microfluidic channel to magnetization curves.

1.3 Brief overview

The theoretical analysis of the problem of this thesis is divided into two chapters, in Chapter two the magnetic part is discussed. The properties of possible suitable magnetic materials are investigated, the forces in the system are analyzed and the magnetic field control is calculated. The fluidic part is discussed in Chapter three. The fluid flow and fluid displacement are analyzed and the influences on the maximum achievable rotation frequency are listed.

With this theory a chip is designed and manufactured. The design choices and the problems occuring during manufacturing are then discussed in the Chapter four. With this chip experiments are performed, and photos of the used setups and used protocols are shown in Chapter five. In Chapter six the results of the experiments are shown: the measured magnetic properties, the optically observed motion of beads and fluid displacement. Chapter seven gives the conclusion and recommendations of this thesis, including an outlook to optionally implement extra features to the system. The appendix includes supplementary theory, mask design, and additional fabrication information.

Chapter 2

Magnetism

In this chapter the magnetic phenomena relevant for this thesis are analyzed. Properties of magnetism in different types of materials and the concept of a magnetization curve are discussed according to definitions for the magnetic fields. The magnetic moments and forces of the system are calculated to get an estimation for the force exerted on the bead by the magnetized disk. The magnetic field control is studied in the last section.

Magnetic effects occur when electric charges are moving, this can be an electrical current through a wire or circular currents in materials. These circular currents can be caused by electrons which are orbiting around the atomic nucleus (orbital) or are rotating around their own axes (spin). Whether a material feels an attractive or repulsive force is material dependent [28]. The analysis on the atomic level is very complex and will not be done. As a basis for the description of properties on macroscopic level Maxwell's equations can be used, and in Appendix A.1.3 the inductive force of a conduction ring in a changing magnetic field is explained.

2.1 Definitions

In order to analyze magnetic fields the definitions of three fields are required. First the magnetic field $\vec{H}$ is defined, which is the field applied externally to a material, with the unit ampere per meter (A/m). In vacuum this field is equal to the magnetic induction $\vec{B}$ in tesla (T) times the magnetic permeability of free space μ_0. The magnetic induction can directly be measured with a Hall sensor. When the magnetic field $\vec{H}$ is applied to a certain object with certain magnetic properties it becomes magnetized. In the material occurs a magnetization field $\vec{M}$ in ampere per meter (A/m). This magnetization is a measure of the magnetic moment per volume of material. Thus to describe the magnetization process of a piece of material three magnetic vectors are required: the magnetic field $\vec{H}$, the magnetization $\vec{M}$, and the magnetic induction $\vec{B}$.

The definition of ampere is the steady current that when flowing in straight parallel wires of infinite length and negligible cross section, separated by a distance of one meter in free space, produces a force between the wires of $2 \cdot 10^{-7}$ newton per meter of length [42]. The equation for this force is

$$F = \frac{\mu_0 \ I^2}{2 \ \pi \ r} = \frac{\mu_0 \ 1^2}{2 \ \pi \ 1} = 2 \cdot 10^{-7} \tag{2.1}$$

Hence the value of μ_0 is defined to be exactly $4 \ \pi \ 10^{-7} \ N/A^2$ and is called the magnetic permeability of free space. Using Maxwell's equations and the definition of the H-field the relation between the speed of light, permittivity and the permeability of vacuum can be defined

$$c = \frac{1}{\sqrt{\mu_0 \ \epsilon_0}} \tag{2.2}$$

Depending on the properties of a material it feels a repulsive or an attractive force to an applied magnetic field. The relative permeability describes this magnetic behavior of the

material, and is defined by the relative permeability μ_r (dimensionless). The permeability of free space μ_0 multiplied by the relative permeability μ_r is the permeability μ of the medium:

$$\mu = \mu_0 \cdot \mu_r \tag{2.3}$$

There exist different definitions for the magnetic field $\vec{H}$. For a discussion about this definition and conversion ratios between the different systems see Appendix A.1. The definition of the magnetic field $\vec{H}$ which will be used in this report is the SI-definition

$$\vec{B} = \mu_0(\vec{H} + \vec{M}) \tag{2.4}$$

The resulting magnetic induction $\vec{B}$ depends on the applied magnetic field $\vec{H}$ added to the material magnetization $\vec{M}$ times the free space permeability μ_0. For most substances the magnetization $\vec{M}$ is proportional to the applied magnetic field $\vec{H}$. This holds on the condition that the applied field is not too strong, else it could saturate and become independent of the applied field. In most materials a proportionality constant between the magnetization $\vec{M}$ and the applied field $\vec{H}$ can be defined, called the magnetic susceptibility χ_m. This is a dimensionless quantity that varies from one substance to another. It is positive for paramagnets (attractive force) and negative for diamagnets (repulsive force). For linear media holds

$$\vec{M} = \chi_m \vec{H} \tag{2.5}$$

In linear media the magnetization $\vec{M}$ is proportional to the magnetic field $\vec{H}$, therefore the magnetic induction $\vec{B}$ is also proportional to the magnetic field $\vec{H}$.

$$\vec{B} = \mu_0(\vec{H} + \vec{M}) = \mu_0(1 + \chi_m)\vec{H} = \mu\vec{H} \tag{2.6}$$

Thus for the relation between the permeability and susceptibility holds

$$\mu \equiv \mu_0(1 + \chi_m) = \mu_0 \ \mu_r \tag{2.7}$$

In vacuum the susceptibility is zero, so the permeability μ is equal to the permeability of free space μ_0. The relative permeability μ_r is equal to the magnetic susceptibility χ_m plus one.

2.2 Magnetic materials

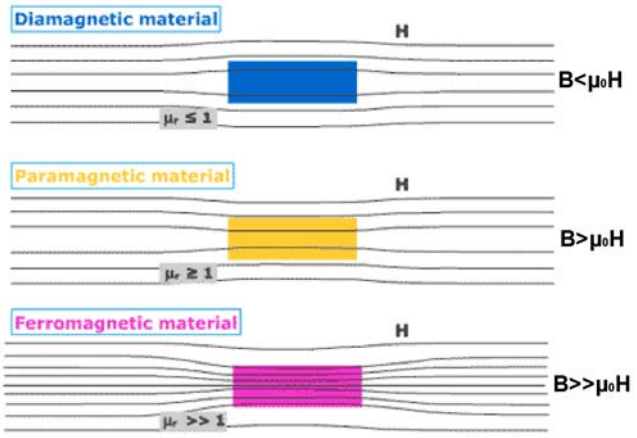

Figure 2.1: Three types of magnetic effects. [1]

There exist several types of magnetic effects. Which type is observed not only depends on the properties of the material but also on the temperature. Three common magnetic effects are shown in Figure 2.1.

- **Diamagnetism**. The material is repulsed by the magnetic field. This is a very weak effect. It will not be observed when also other types of magnetic effects are involved.
- **Paramagnetism**. The material is attracted to the field. This is also a weak effect, but stronger than diamagnetism. A special form is **superparamagnetism**, which has similar properties but with a much higher relative permeability.
- **Ferromagnetism**. The material experiences a strong force. Certain materials can retain magnetization in absence of an external field, these materials are suited for permanent magnets. [15, 28]

2.2.1 Different types of magnetic effects

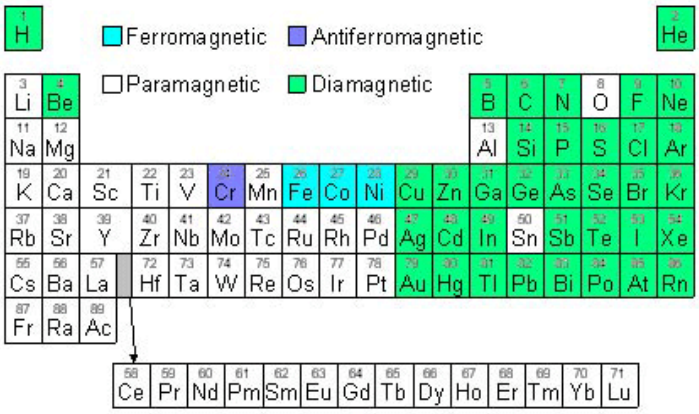

Figure 2.2: Periodic system of the elements with their magnetic properties at room temperature. [11]

An overview of the elements and their magnetic behavior at room temperature can be seen in Figure 2.2. The different types of magnetic effects are more elaborately discussed in Appendix A.2. Dia- and paramagnetism are not suited for generating the required force for the pumping action, because these magnetic effects are very weak. The two stronger magnetic effects are superparamagnetism and ferromagnetism.

A superparamagnetic particle is so small that the thermal energy is larger than the magnetic energy, therefore there is no remanent magnetization left when the external field is removed. The advantage of superparamagnetism is the large susceptibility compared to ordinary paramagnetism. An example is small magnetite Fe_3O_4 particles.

Ferromagnetic materials align (almost) all atomic moments causing a large susceptibility. These materials have a hysteresis loop, meaning a minimum field is required to demagnetize the materials. When the external field is removed still a remanent magnetization is present. The saturation magnetization of a ferromagnetic material is usually very high. Ferromagnetic materials are iron, cobalt and nickel. These materials behave ferromagnetic up till their Curie temperature, and for higher temperature become paramagnetic, which is a reversible effect. The lanthanides neodymium (Nd), samarium (Sm) and gadolinium (Gd) have a Curie temperature below room temperature. However, in for example an alloy with a ferromagnetic material with a high Curie temperature they could become a strong permanent magnetic at room temperature. A magnetic effects with a similar atomic interaction force as ferromagnetism is antiferromagnetism. However this exchange interaction between neighboring atoms leads to an anti-parallel alignment of the magnetic moments. The net susceptibility of an antiferromagnetic material is therefore of the same order as a paramagnetic material.

2.2.2 Domains

The theory of ferromagnetism is based on electrical exchange forces as discussed in Appendix A.2. A piece of ferromagnetic material is magnetized due to the exchange forces, and magnetization occurs gradually in domains as shown in Figure 2.3. These domains, called Weiss domains, require a certain magnetic field in order to change their magnetization direction into a certain direction, which is called the coercitive field H_c. When the magnetic field is removed there is still a magnetization present, which is called the remanent magnetization M_r. The existence of Weiss domains is hinted at by the observation that some magnetic properties, and in particular coercivity and remanence vary greatly with grain size. The maximum coercivity for a given material occurs within its single domain range (see Figure A.3). For large grain sizes, coercivity decreases as the grain subdivides into domains. For very small grain sizes, coercivity also decreases, but now due to the randomizing effects of thermal energy, which is an explanation for superparamagnetism.

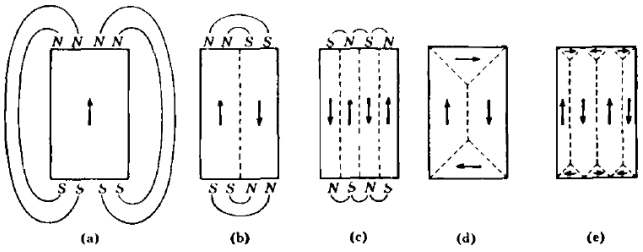

Figure 2.3: The formation of domains in a single crystal of iron. [15, p 37-4]

The maximum magnetization of a material is called the saturation magnetization M_s. The magnitude of this saturation magnetization is known from theory, but the exchange force does not relate to the direction of the saturation magnetization. For a homogeneous sample at constant temperature, the magnitude of M_s is uniform, but the direction in general is not uniform from one region to another, as shown in Figure 2.4. Uniformity of direction is achieved only by applying a large enough field. We can define a magnetic energy in a piece of material. This magnetic energy is the sum of the energy of the magnetization of the domains and the energy of the walls between the different domains. These energies are both dependent on the grain size and isotropy of the domains. This difference in required magnetization energy is causing the steps in the magnetization curve shown on the right in Figure 2.4, which shows that a piece of material is magnetized domain by domain. A uniform soft magnetic material will have domains which are easy to magnetize and therefore have a low coercivity H_c. [15, 36]

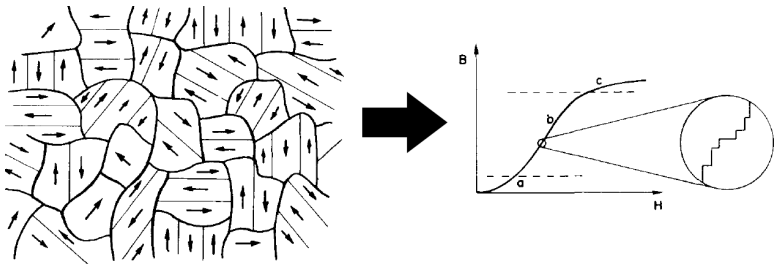

Figure 2.4: On the left the microscopic structure of an unmagnetized ferromagnetic material is shown. Each crystal grain has an easy direction of magnetization and is broken into domains. On the right the magnetization curve for this piece of polycrystalline iron is shown. [15]

A study on the magnetization of thin permalloy disks, especially relevant for this thesis, is shown in ref. [8]. In this study a layer of 40 nm permalloy ($NiFe$) was sputtered with an

in-plane magnetic field of 60 $\frac{kA}{m}$, and subsequently small shapes were patterned using ion beam milling, yielding disks with radii of 20, 25, and 50 μm. The basic state of the magnetization in such a disk is a vortex. When a magnetic field is applied, magnetic domains are formed depending on the anisotropy, domain wall, and pole energies. This will create magnetized domains as shown in Figure 2.5. The exact domain structure depends also on the magnetic history of the material. The disk is saturated when sufficient magnetic energy is applied to the disk, in this case only one large magnetic domain is present in the disk. [8]

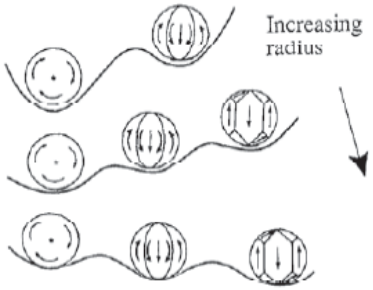

Figure 2.5: The domain energy landscape for different radii disks. [8]

2.2.3 Magnetization curve

Dia- and paramagnetic materials have a constant magnetic susceptibility χ, not reaching saturation, and the magnetization curve of these materials is just a straight line though the origin, see Figure 2.6. The magnetization curve of an antiferromagnetic material is similar to that of a paramagnetic material. The susceptibility χ of a superparamagnetic material is much higher, and with a large enough applied field H, the material reaches saturation.

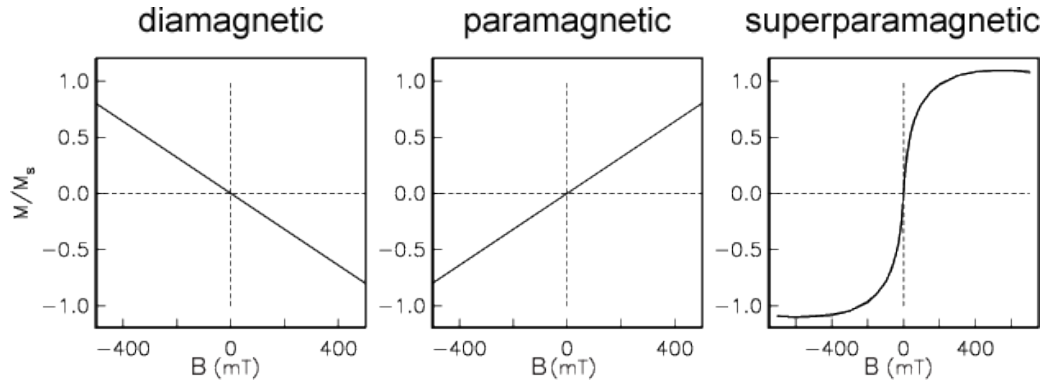

Figure 2.6: The normalized magnetization curves for dia-, para- and superparamagnetic materials [2].

If magnetic hysteresis is present in the material, a certain magnetic field is required to demagnetize the material as shown in Figure 2.7. The required magnetic field to demagnetize the material is called the coercivity H_c. The remanence or remanent magnetization M_r is the magnetic field still present when the external magnetic field is removed. The surface closed by the hysteresis loop is a measure for the energy required to flip the magnetization.

A permanent magnet has a large remanence and a very large coercivity, a large permanent magnetization which is not easily altered. For transformers soft magnetic materials are required, so the magnetization is easily reversed, and an enormous magnetization results from applying a small applied field. To arrange this, a pure material is required, which has very few dislocations

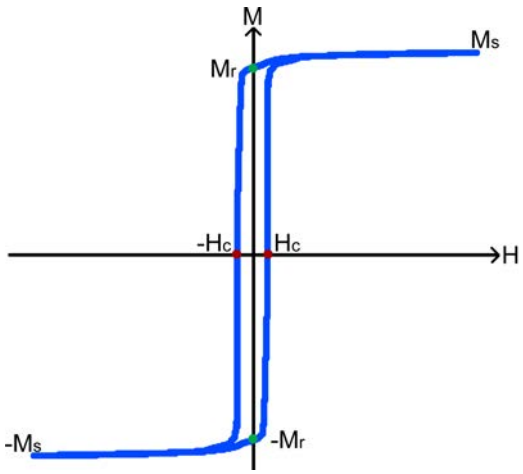

Figure 2.7: Concepts belonging to the hysteresis loop of a ferromagnetic material.

and impurities so that the domain walls can move easily. A small anisotropy would be profitable for a soft magnetic material, since the hysteresis curve is the same for all angles. It turns out that this occurs for an alloy of nickel and iron. Somewhere between 70 and 80 percent nickel a soft magnetic material is obtained. These alloys are called permalloys. These permalloys are used in this thesis as disk material, and their properties are therefore quite important.

Permalloys must be very carefully manufactured and handled. The magnetic properties of a piece of permalloy are drastically changed if it is stressed beyond its elastic limit, so stress in the material must be avoided. The permeability of a film of permalloy is reduced by the dislocations and slip bands (very thin sheet grains lowering the internal stress). Grain formation is the cause that the domain wall can no longer move easily. Thus mechanical deformations will decrease the magnetic quality of permalloy. High permeability can be restored by annealing the bulk material at high temperatures [15, p 37-11].

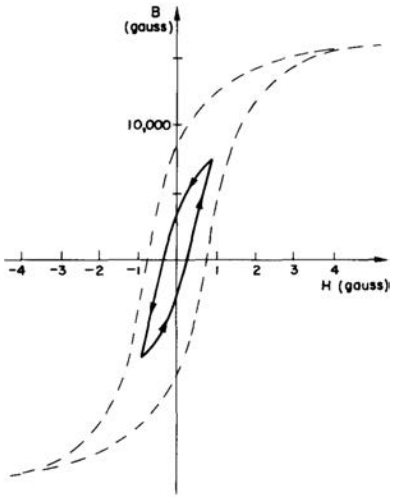

Figure 2.8: A hysteresis loop that does not reach saturation. [15]

When a ferromagnetic material is only used for relatively small magnitudes of applied field, then the hysteresis curve can be approximated as a linear susceptibility, see Figure 2.8. This effective susceptibility is dependent on the range of magnetic fields which are applied to the material.

2.2.4 Material requirements

A number of parameters can be modified in order to optimize the magnetic properties of the materials used in this thesis. For the magnetic beads it is required to have a high susceptibility to be able to apply a sufficiently large force on the bead. The second requirement is a low remanent magnetization to prevent the beads from forming aggregates. The type of magnetic material best suited, which is also available in the form of beads is superparamagnetic material.

For the disks it is important to make use of a soft magnetic material with a large saturation magnetization. The required magnetic field to flip the magnetization must be small, and the material must be isotropic. The type of magnetic material best suited for the disk is a ferromagnetic material with a very low magnetic coercivity H_c, and a good option chosen in this thesis is permalloy ($NiFe$).

2.3 Interaction force between disk and bead

In the previous section choices are made for the types of magnetic material which will be used for the experiments. Based on the properties of these materials, mathematical models of the physics can be made to obtain some insight in the working mechanisms. The concept of magnetic charge and magnetic dipoles are used to get an estimation of strength of the forces between the disk and bead.

2.3.1 Superparamagnetic bead

The beads which are used in the experiments constist of superparamagnetic material. The manufacturers of the magnetic beads are not completely clear on the exact composition of the beads. The most beads consist of a non-magnetic matrix with small trapped magnetite particles. A possible structure is shown in Figure 2.9.

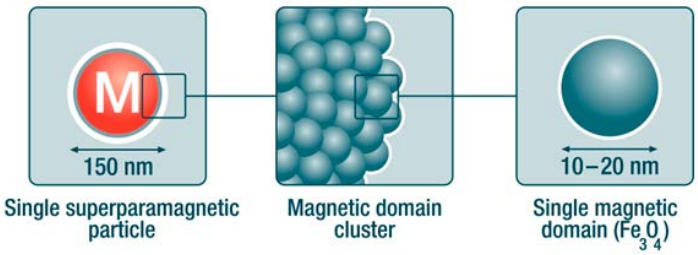

Figure 2.9: Structure of a superparamagnetic bead. [29]

In the experiments the magnetic beads have to circulate around the soft magnetic disks. Therefore a torque on the bead is unwanted, since it will disturb the circular motion. On the magnetic bead this unwanted torque can be exerted which could have different causes. The beads can be magnetically anisotropic, caused by non-uniform distribution of the magnetic material. Another option is that not all magnetic domains can follow the changing magnetic field due to magnetic imperfections [16]. This torque is for our application unwanted, because this prevents the beads from following the magnetization in the disk.

2.3.2 Magnetic charge

First of all it must be stated that physically there is no such thing as magnetic charge. The source of magnetism is circulating currents within the atoms, either from the spinning electrons or from the motion of electrons in atoms. The concept of magnetic charge however is used to describe the macroscopic effect of magnetism with variables and techniques known from electrostatic, which makes it more convenient to evaluate the fields. Together with this concept comes magnetic poles, helping to understand the magnetic problems. An artificial analogy with the electrical charges can be made, by defining a magnetic charge density ρ_m [15, page 36-2].

The divergence of the magnetization field $\vec{M}$ is related to the magnetic charge density by the following equation

$$\vec{\nabla} \cdot \vec{M} = -\rho_m \tag{2.8}$$

where the magnetic charge ρ_m is purely mathematical. In Appendix A.3 an example is evaluated how a magnetic object can be approximated by two opposite magnetic charges. The disadvantage of this method is that close to large surface poles the model can not be applied, but further away it will be a good approximation (see Figure 2.14). Another option would be to calculate the magnetic field by integrating over all the magnetic charge density using the Coulomb law. The disadvantage of this method is that the differential equations to calculate the charge distribution are complicated to solve and can only be determined numerically using a Finite Element Method, which gives much less insight than a mathematical description.

2.3.3 Magnetic forces

Magnetism always occurs in dipoles, and there is no evidence for the existence of magnetic monopoles or net magnetic charge. To keep calculations feasible and obtain some insight into the forces which are playing a role, the magnetized disk and sphere employed in this thesis can be approximated with magnetic dipoles to calculate the force between the disk and bead when the distance is large. For smaller distances other assumptions are made.

Force and torque

The force on a magnetic charge in a magnetic field $\vec{B}$ is analog to the force of an electric charge exerted by an electric field, which is the charge times the field.

$$\vec{F_m} = q_m \ \vec{B} \tag{2.9}$$

A dipole in an object is bound to a certain distance d, and it contains two equal opposite charges q_m. Multiplying these two dipole properties leads to a dipole moment m.

$$\vec{m} = q_m \ \vec{d} \tag{2.10}$$

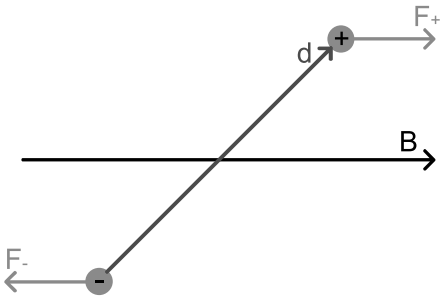

Figure 2.10: Two opposite charges feel opposite forces in a uniform magnetic field.

The torque on such a dipole is the cross product between the displacement vector $\vec{r}$ and the force $\vec{F}$. Therefore the force on a dipole can be calculated by filling in Eq. 2.9 for the force, see also Figure 2.10. This leads to the general expression for the torque on a magnetic dipole.

$$\tau_m = r \times F = 2 \ \tfrac{1}{2} \ \vec{d} \times \vec{B} \ q_m = d \ q_m \ B \ \sin(\alpha) = m \ B \ \sin(\alpha) \tag{2.11}$$

On the dipole a torque is exerted until it is aligned with the external field. Suppose the magnetic dipole is placed in a non-uniform magnetic field, then the positive and negative charge will experience a different force due to the magnetic field gradient, see Figure 2.11. When the

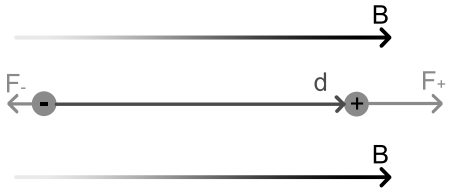

Figure 2.11: Two opposite charges feel different opposite forces in a non-uniform magnetic field, resulting in a net force.

distance d between the two magnetic charges is small, the difference in magnetic field strength is the gradient of the magnetic field $\nabla\vec{B}$ times the distance d.

$$\vec{F}_{md} = \Sigma\ \vec{F}_m = q_m\ \vec{d}\ \nabla\vec{B} = q_m\ \vec{d}\cdot\nabla\vec{B} = (\vec{m}\cdot\nabla)\vec{B} \tag{2.12}$$

If the magnetization $\vec{m}$ is not dependent of place, this expression for the force on a magnetic dipole could also derived using the energy equation

$$\vec{F} = \nabla U_{mag} = \nabla(\vec{m}\cdot\vec{B}) \mathrel{\widehat{=}} (\vec{m}\cdot\nabla)\vec{B} \tag{2.13}$$

This is the general expression for the force of a magnetic dipole [7, 41]. When the magnetic field is not linear and the separation distance d is large, the forces on the two opposite charges can be calculated separately to make a better estimation of the net force.

The far-field force

For calculating the far-field force of the disk on the bead, twice a dipole approximation is made. First the field of the magnetized disk is evaluated using a standard expression for the far-field of a dipole. Next the force on the bead placed in this field is calculated.

In Appendix A.4 the magnetic moment of an in-plane magnetized disk is calculated, the result is

$$m_d = M_{sd}\ h\ R^2\ \pi = M_{sd}\ V_d \tag{2.14}$$

where M_{sd} is the saturation magnetization of the disk, h is the disk thickness, R is the disk radius, and V_d is the volume of the disk. Using this expression the magnetic field at large distance of the magnetic dipole along the dipole axis can be calculated. The far-field expression for the dipole magnetic field is

$$B_d = \frac{\mu_0}{4\ \pi}\frac{m_d}{r^3} \tag{2.15}$$

where r is the distance from the disk. The assumption is made that the magnetic bead is not used in the saturation region, since this requires a very large magnetic field. The magnetization of a superparamagnetic bead is $\vec{M}_b$ and the difference between the susceptibility of the magnetic bead and water is $\triangle\chi$. For this bead placed in a magnetic field $\vec{B_{ext}}$ holds

$$\vec{M}_b = \frac{1}{\mu_0}\frac{\triangle\chi}{(1+\triangle\chi)}\ \vec{B_{ext}} = \frac{\chi_{eff}}{\mu_0}\ \vec{B_{ext}} \tag{2.16}$$

where χ_{eff} is the effective magnetic susceptibility of the bead. The dipole moment of the bead is the magnetization times the volume of the bead

$$\vec{m_b} = M_b\ V_b = \frac{V_b\ \chi_{eff}}{\mu_0}\ \vec{B_{ext}} \tag{2.17}$$

The force on a magnetic dipole is dependent on the magnetization of the bead and the gradient of the magnetic field (see Eq. 2.13). The magnetic field generated by the disk can be

used for the external field of the bead magnetization equation. The force on the bead can be calculated by

$$\begin{aligned}\vec{F}_b &= (\vec{m}_b \cdot \nabla)\vec{B}_d = \frac{V_b\ \chi_{eff}}{\mu_0}\ (\vec{B}_d \cdot \nabla)\vec{B}_d = \frac{V_b\ \chi_{eff}}{\mu_0}\ \left(\frac{\mu_0\ m_d}{4\ \pi}\right)^2\ \frac{1}{r^3}\ \frac{\partial \frac{1}{r^3}}{\partial r} \\ &= \frac{V_b\ \chi_{eff}\ \mu_0\ m_d^2}{16\ \pi^2}\ \frac{-3}{r^7} = \frac{\mu_0}{16\ \pi^2}\ (V_b\ V_d^2)\ (\chi_{eff}\ M_{sd}^2)\ \frac{-3}{r^7} \end{aligned} \tag{2.18}$$

Despite of all the assumptions this is a quite large equation. The most interesting for our application is the scaling of the force on the bead as a function of geometry, magnetic properties and distance. The force is proportional with the volume of the bead V_b and to the square of the volume of the disk V_d. The force on the bead has a squared dependence on the magnetization of the disk M_d, but a linear dependence on the susceptibility of the bead χ_{eff}. The force drops very rapidly an increasing distance r, with one over the distance to the power seven. The force is directed towards the disk. Hence the far-field bead force dependents quadratically on the magnetic moment and volume of the disk and decreases inversely to the power seven with the distance.

The near-field force

Because the magnetic charge of the disk is positioned at the border of the disk, the largest force is exerted on the magnetic bead near this border. Therefore the force on the bead is calculated near this border, since the bead is positioned here. The magnetized disk has a magnetic surface charge on the border as shown in Figure A.7. The magnetic bead which is near this border will try to mirror this magnetic charge, and as a consequence the two are attracted to each other. To make a rough estimation for this force between this disk and sphere, some assumptions are made. Assumed is that the disk is in saturation, because of the large external magnetic field. Due to this uniform magnetization, there is a charge density on the side of the disk which is uniform over the height of the disk. When a cross section is taken, there is a line of magnetic charge, see the blue line in Figure 2.12. Hence the attraction force between two equally charged sheets is calculated in this model.

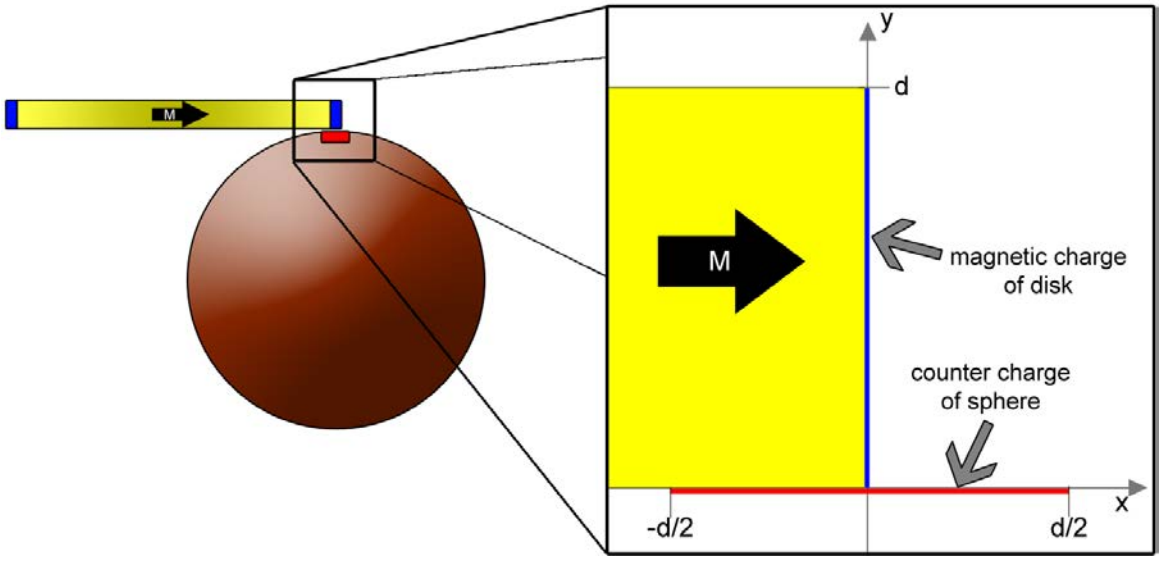

Figure 2.12: Close-up of the edge of the magnetized disk, in blue the magnetic charge of the disk and in red the magnetic counter charge on the sphere.

The surface charge ρ_s of the disk is uniform and equal to the saturation magnetization M_s with a minus sign. The magnetic counter charge of the sphere will be equal to this charge,

assuming that the relative permeability μ_r of the sphere is high. To simplify the calculations the assumption is made that the distance over which this counter charge is spead is equal to the height of the disk h (see Figure 2.12). The problem will be analyzed in two-dimensions, in order to obtain a practical expression for the force between the disk and the sphere.

The approach of this problem is to first calculate the magnetic field $\vec{H}$ of the magnetic charge of the disk, by integrating over the surface charge ρ_s. The second step is to integrate this magnetic field $\vec{H}$ over the magnetic counter charge, this results in the attractive force between the disk and the sphere. The derivation of these integrations can be found in Appendix A.5. The resulting equation for the attraction force is the quite simple expression

$$F_b = \frac{\mu_0}{2\ \pi}\ \ M_{sd}^2\ \ (h_d\ l_d\ 1.73) \tag{2.19}$$

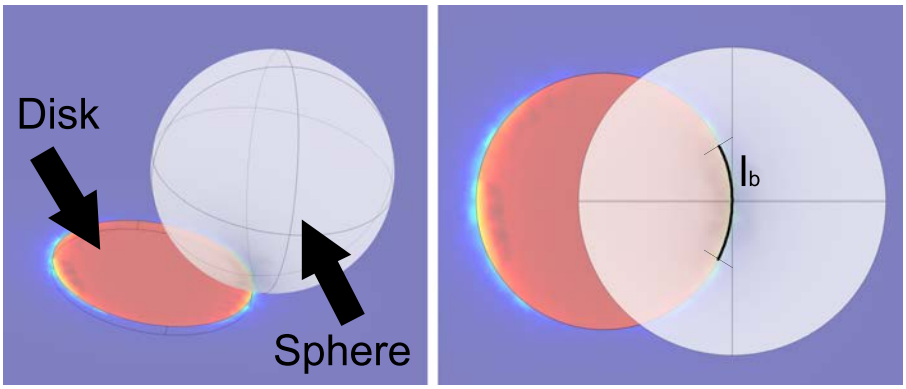

Figure 2.13: Magnetized disk with sphere, on the right the interaction distance l_b.

The saturation magnetization M_{sd} is a property of the disk material, for permalloy $8\ 10^5\ A/m$ [22]. The disk height h_d is a geometric property, set during the manufacturing. The distance l_b is the interaction distance between the bead and the disk, as shown in Figure 2.13. This distance can be set to one sixth of the disk radius $\frac{R_d}{6}$.

The equation can be split into different parts: the $(h\ l_d\ 1.73)$ part is a geometry factor, a larger interaction distance and a thicker disk will increase the magnetic force. The saturation magnetization M_s is a material factor. The magnetization of the disk and bead must be as high as possible to maximize the force, since the disk magnetic charge is mirrored by the sphere. When the magnetization in the disk is rotating, the distance is approximately the same. So when the bead is following the magnetization, the force will be in the same order of magnitude.

Possible model improvements

It is possible to improve the near-field model for the magnetic force on the bead. The bead is filled with small (approximately 50 nm) superparamagnetic magnetite particles. These all get separately magnetized, and the magnetic field H exerts a force on each magnetic particle in the bead. The percentage of magnetite Fe_3O_4 in the polystyrene bead is about 3% [21]. The force on the bead could be calculated by integrating the field, generated by the magnetized disk, squared over the diameter of the bead

$$\begin{aligned} F_y = \frac{\partial U_{mag}}{\partial y} = \frac{\partial \int_V \frac{1}{2}\ \vec{H}_y \cdot \vec{B} \mathrm{d}V}{\partial y} = \frac{\partial \int_{h_1}^{h_2} \frac{1}{2}\ \mu\ H_y^2\ A(y) \mathrm{d}y}{\partial y} \\ = \frac{1}{2}\ \mu \int_{h_1}^{h_2} \frac{\partial H_y^2\ A(y)}{\partial y} \mathrm{d}y \\ = \frac{1}{4} \frac{\rho_s\ \mu}{2\ \pi} \int_{-s-2\ R}^{-s} \frac{\partial \left(\left(\ln\left(y_1^2\right) - \ln\left((h-y_1)^2\right) \right) \right)^2\ \left(\pi\ \left(R_b^2 - (y+s+R_b)^2\right)\right)}{\partial y} \mathrm{d}y \end{aligned} \tag{2.20}$$

which is hard to solve. It can be done numerically in order to get a better estimation of the force on the bead. The disadvantage of this method is that it gives less insight into the working mechanism and scaling, and all the geometric variables must be known to get a solution. Hence this integral is not solved in this thesis.

2.3.4 Near-field simulations

To check whether the previous calculations are correct, a simulation is done in COMSOL[1]. First of all the dipole approximation is checked by comparing the simulated near field of the disk by the dipole approximation. Next the calculations on the two charged sheet model for the near-field force are verified by simulating two charged sheets and evaluating the forces.

Two charge model

As can be seen in Figure 2.14, close to the disk the magnetic field of the analytical point charge approximation is off with the simulated field. For larger distances the two charge model is a good approximation compared to the simulated field.

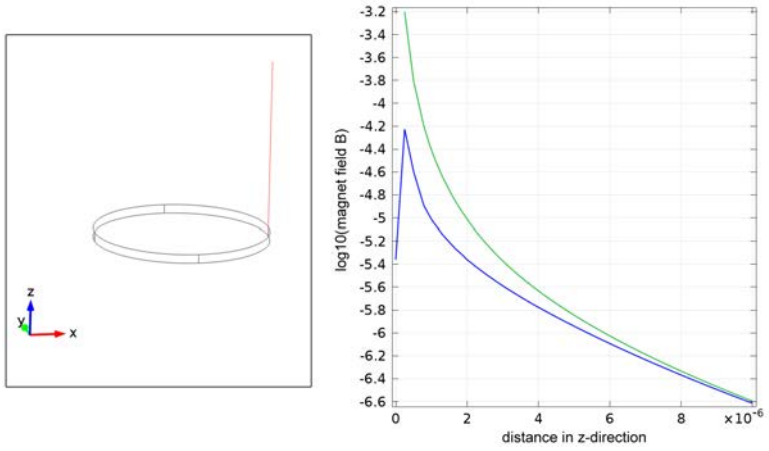

Figure 2.14: In green the point charge approximation and in blue the COMSOL simulation result, the height of the disk is 500 nm.

Near-field force

Previously the field of a charged sheet was calculated in order to calculate the near-field force. To verify this field, also simulation is performed. In Figure 2.15 the resulting field is shown, which has the same shape as the field earlier calculated. In simulation the force can easily be evaluated by integrating the field over the line charge and multiplying it by the charge density. The result of the analytic equation can then be evaluated by substituting the variables, which are chosen in the simulation, in Eq. 2.19.

	Calculation	Simulation
h=0.5	$3.89 \cdot 10^{11}$	$3.89 \cdot 10^{11}$
h=1	$7.78 \cdot 10^{11}$	$7.77 \cdot 10^{11}$

Table 2.1: Results for the near field force evaluated by means of calculation and simulation.

[1]COMSOL Multiphysics 4.2a using the Magnetic Fields (mf) physics module, unless otherwise noted the MUMPS solver is used.

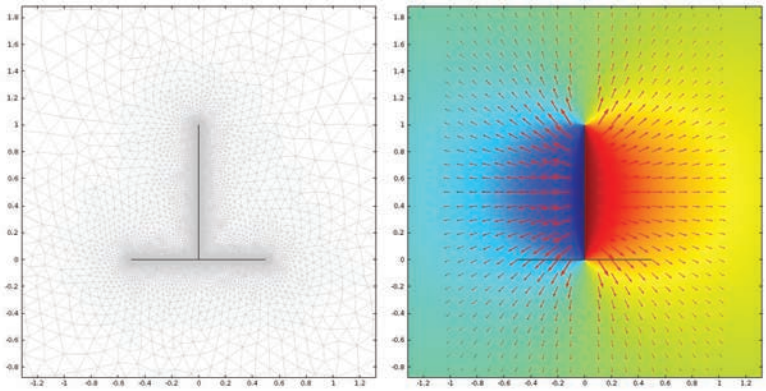

Figure 2.15: On the left the mesh is shown (boundary box is 50*h), and on the right the field of one charged sheet is plotted.

The calculation and simulation are compared for two different values of height h, the result can be seen in Table 2.1. It can be seen that both methods give the same results, the derivation of the field (Eq. A.17) and integration done of this field (Eq. A.19) are correct.

Interesting is the decrease of the force as a function of the bead separation distance, which could easily be evaluated using simulation. The horizontal charged sheet is moved down with a certain distance, which is expressed normalized by the disk height h_d.

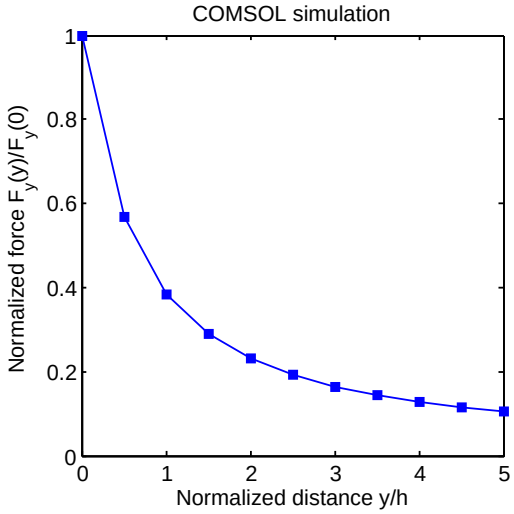

Figure 2.16: The normalized attraction force as a function of the distance.

The drop of the magnetic force as function of the distance can be seen in Figure 2.16. At a distance of five times the disk height (5 h) the force is still about one tenth of the maximum force close to the vertical sheet. The consequence for the experiment is that a large interaction force can only be achieved when the distance very small.

2.3.5 Remarks on the bead force

Important material parameters which influence the force exerted on the bead are the disk saturation magnetization squared M_d^2 and the susceptibility of the bead χ_b. These must be as high as possible for a large force on the bead. When the disk is in saturation, the magnetization will not increase with a larger magnetic field strength. The used beads are hard to saturate, hence a larger magnetic field strength will increase the bead magnetization and therefore the force on the bead.

The magnetic force is a volume force, a larger geometry gives a larger force. Therefore the volume of the disk has a large influence on the force, however the radius of the disk is fixed

by the chosen channel width. Hence the geometric parameter that could be maximized is the thickness of the disk h_d. The disk must be as high as possible to optimize the magnetic force. Another parameter influencing the force is the distance between the disk and the bead, the larger distance between the bead and the disk, the less force is exerted on the bead. When the disk is not clean, the bead-disk distance is larger. Hence the disk must be clean, and a possible coating layer of the disk or the bead must be as thin as possible.

In the previous analysis a high susceptibility of the beads ($\mu_r > 30$) is assumed, causing the magnetic charge of the disk to be mirrored by the bead. If the susceptibility is lower, the analysis is more complex. The problem is not analytically solvable, because the bead creates an internal field, making it difficult to determine where the magnetic charges are located. To analyze this, a finite element method is required.

An option to increase the force is to apply the external magnetic field under a certain angle, such that the magnetic charges of the bead generated by the external field are located closer to the disk. Another possibility is to change the geometry such that more force is exerted on the beads compared to the torque on the beads, with for example an array of pillars instead of disks.

2.4 Magnetic field control

In previous section the force on the bead is modeled when a certain external magnetic field is applied. This magnetic field is the driving source of the system. Two main options exist to locally generate a rotating in-plane magnetic field: with physically rotating permanent magnets or with a set of solenoids. The latter, magnetic quadrupole setup, is chosen for the control of the magnetic field. The advantages of such a setup are that the field is precisely controlled and can simply be varied in strength and frequency by changing the current signals. The disadvantage is the relatively low magnetic field strength and low achievable frequencies compared to rotating magnets. Also the quadrupole setup requires a control circuit. In this section the magnetic field generated by the quadrupole is studied. The basis for this analysis is the derivation of the magnetic field of a wire and long solenoid, which can be found Appendix A.6.

2.4.1 Magnetic quadrupole

A quadrupole construction is used consisting of four solenoids in combination with a round iron construction with four pole shoes to the middle, as shown in Figure 2.17. Such a setup is relatively compact and can generate a rotating magnetic field between the poles by applying current signals to the solenoid pairs which have 90° phase difference.

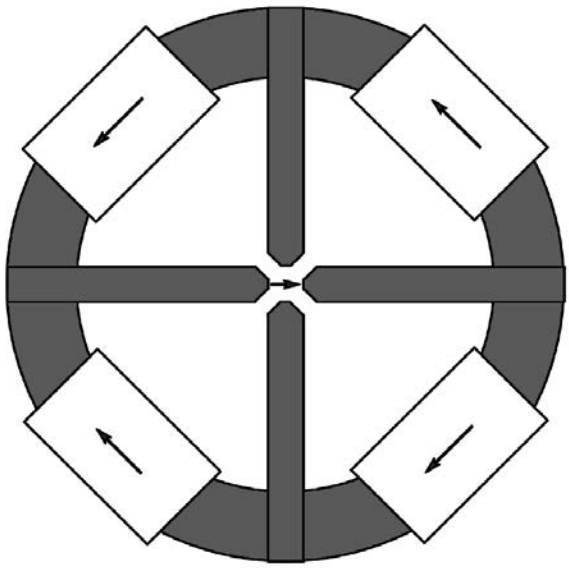

Figure 2.17: Top-view quadrupole setup with four solenoids shown for a possible field angle. [12]

The idea of the quadrupole setup is to generate a controllable rotating magnetic field. It is assumed that the direction of the magnetic field in the center is known by the current direction of the solenoids. The magnitude of the generated field can be analyzed with an equivalent electronic circuit, this analysis can be found in Appendix A.7. For the magnetic field in the air gap of the quadrupole holds

$$B_g = \frac{4 \cdot N \cdot I \cdot \mu_0}{l_g} \tag{2.21}$$

The magnetic field in the air gap depends on the number of turns N, the current through the solenoid I and the gap size l_g (see also Eq. A.33). In practice the magnetic field between the poles is smaller than shown in Eq. 2.21, because a part of the field goes through the iron next to the air gap instead of through the air gap. In the derivation the assumptions were made that the permeability of the iron is very high ($\mu_r >> 1$), soft magnetic, and not in the saturation region. Under the pole surfaces the field will drop approximately inversely with the distance squared $\left(\frac{1}{r^2}\right)$, similar to the field of a point charge.

2.4.2 Available quadrupole

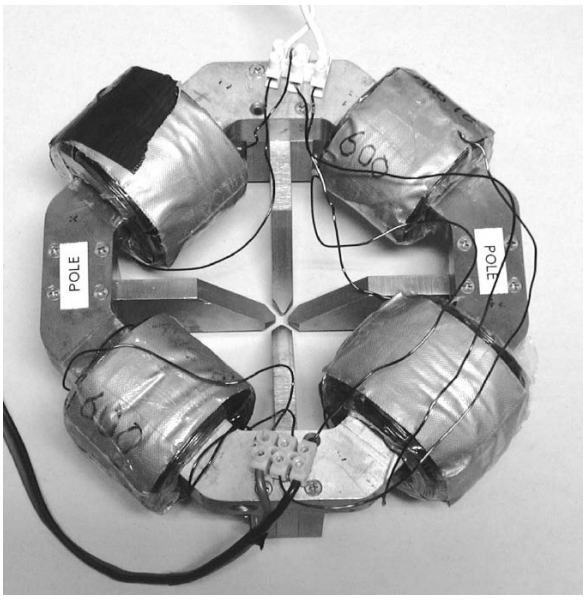

Figure 2.18: A picture of the used quadrupole with the four pole shoes. [12]

From the TST-group a quadrupole was available, a picture is shown in Figure 2.18. The properties of the quadrupole can be filled in Eq. 2.21 to make an estimation for the magnetic field between the poles. The coils each have 600 turns (N), the current through the solenoids (I) can be varied, which is set for the calculations and simulations on 1 ampere. The magnetic field follows this current proportionally, until the magnetization of the iron saturates, which is normally at very high fields. The gap between the poles (l_g) is approximately 1 cm. This gives a magnetic field in the gap of 0.3 tesla.

2.4.3 Simulation of the generated field

To simulate the quadrupole, it is drawn in COMSOL[2], see Figure 2.19. The model of the iron is simply a material with a large μ_r. Magnetic losses and other hysteresis effects are not included in the model. It is possible to simulate such effects, but this will complicate the model and simulating these second order effects is not the aim here. The solenoids are modeled as a remanent flux density B_r on the areas where the solenoids on the iron are located. The expression for this B_r is the expression for the magnetic field H of a solenoid (see Eq. A.33) multiplied by the large permeability μ. The equation used in COMSOL is

$$B_r = \frac{N\ I}{L}\ \mu_r\ \mu_0 \tag{2.22}$$

Parameter	**Value**
Current through the solenoid I	$1\ A$
Solenoid turns N	600
Solenoid length L	$3 \cdot 10^{-2} m$
Relative permeability μ_r	10000

Table 2.2: The parameters used for the simulation of the quadrupole.

[2]COMSOL Multiphysics 4.2a using the Magnetic Fields (mf) physics module

The parameters which have been used for simulation are shown in Table 2.2. The result of this simulation is shown in Figure 2.19. The maximum value of the magnetic field in the center of the poles is about 225 mT. Only a x-component is present in the middle of the poles. The maximum value of the simulation is about 225 mT, which is lower than the 300 mT earlier calculated. This difference is mainly caused by the field lines going through the side poles, shown in Figure 2.20.

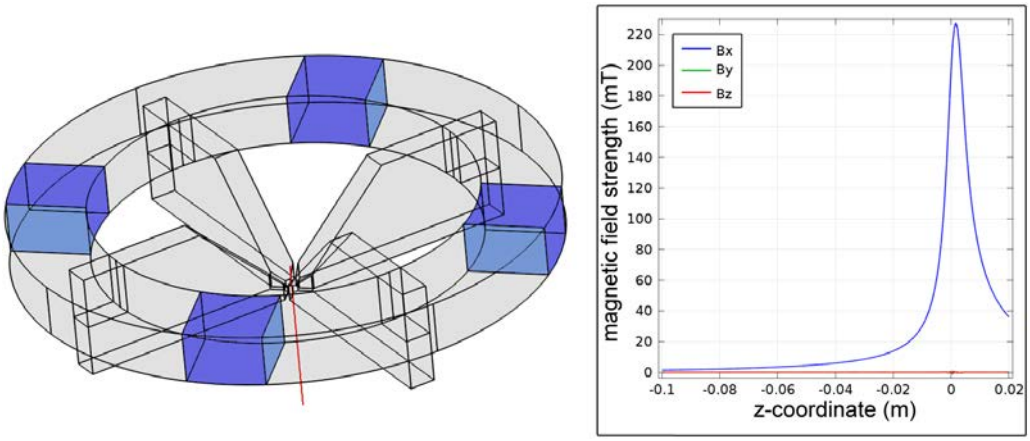

Figure 2.19: The magnetic field in the middle of the quadrupole is plotted, see the red line on the left. The figure is generated using COMSOL simulation.

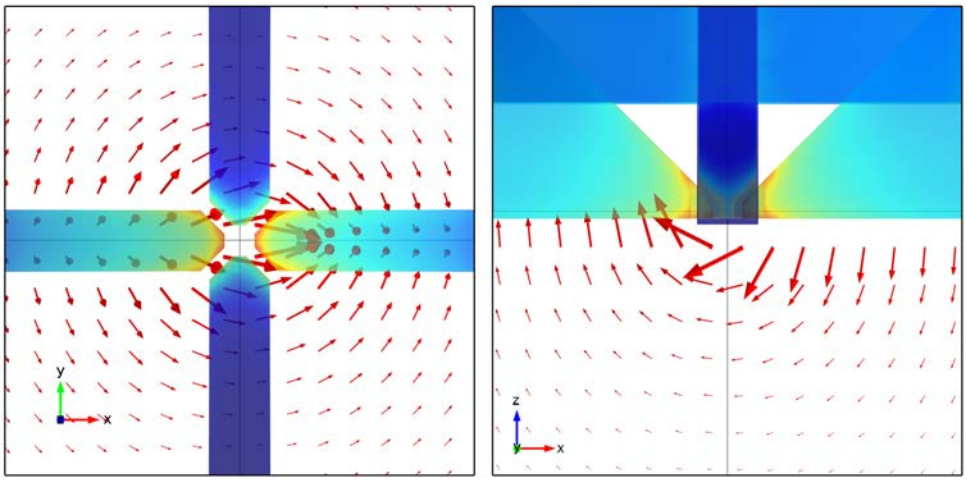

Figure 2.20: The magnetic field for a 0° driving signal, generated using COMSOL. On the left the direction of the magnetic field at a distance of $z = 0.5$ cm below poles, and on the right at $y = 0$ cm is shown.

The shape of the magnetic field has also been investigated. The direction of the generated magnetic field at 0.5 cm below the poles is simulated, since the chip is located at this distance. This field should be in-plane, else it could influence the behavior of the magnetic elements in the chip. The field angles of 0° and 45° to the x-axis are investigated, the other angles are a combinations of these two field angles. The result of the simulation of these field angles is shown in Figure 2.20 and Figure 2.21.

In the center of the quadrupole the generated field only has an in-plane component. When the distance from the center is larger, the field has also an out-of-plane angle and the magnitude of the field decreases. The effective in plane component will decrease rapidly. This process

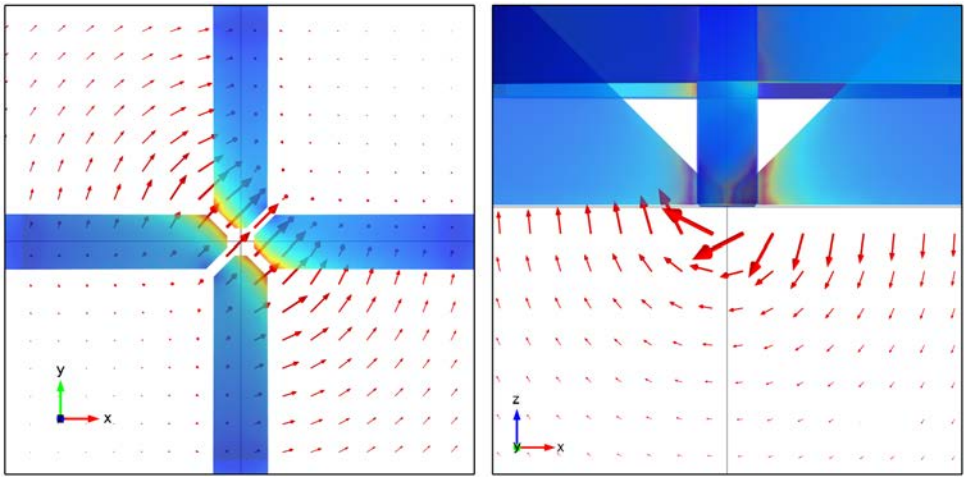

Figure 2.21: The magnetic field for a 45° driving signal, generated using COMSOL. On the left the direction of the magnetic field at a distance of $z = 0.5\ cm$ below poles, and on the right at $y = 0\ cm$ is shown.

occurs about the same for the two different angles. A small advantage of the simulation results is that when the distance z is larger, the field will be more in plane. Therefore the shape of the magnetic field is better when the chip is removed further from the poles, but the magnitude is much smaller. The disadvantage is that only the stray field of the quadrupole is used for the experiment, the strongest part of the generated magnetic field could not be reached, since the gap is too small.

2.4.4 Conclusion on quadrupole

Based on theory and simulation it is important that the channels with the magnetic material are located close to the center of the quadrupole. The magnetic field will drop quite rapidly with the distance below the poles, therefore this distance must be as small as possible for a large magnetic field. The shape of the magnetic field near the center of the poles is good, but when this distance becomes too large, the in plane component will drop. Near the center of the poles a large uniform field is present for all angles.

Chapter 3

Fluidics

In the previous chapter the magnetic theory was discussed in order to estimate the motion of the magnetic beads and the forces on these beads. How the fluid reacts to these moving beads, is investigated in this chapter. The purpose of the moving beads is to directionally displace liquid, creating a net pumping motion.

3.1 Fluid flow

The first step of the analysis of the beads moving in fluid is to investigate which fluidic effects are dominant. The flow regime is derived on basis of the Reynolds number. Based on this the flow can be determined.

3.1.1 Reynolds number

The fluid flow can be described using the Navier-Stokes equations. Different regimes can be characterized using the Reynolds number, whereby for high Reynolds numbers (much larger than 1) inertial forces are dominant. This flow is non-linear and may be turbulent, and complex models are required to simulate this flow. On the other end of this scale is the flow for low Reynolds numbers, in this regime the viscous forces dominate. This flow is laminar and time-reversible. In Figure 3.1 some flow profiles are shown of a flow past a cylinder for low and higher Reynolds numbers.

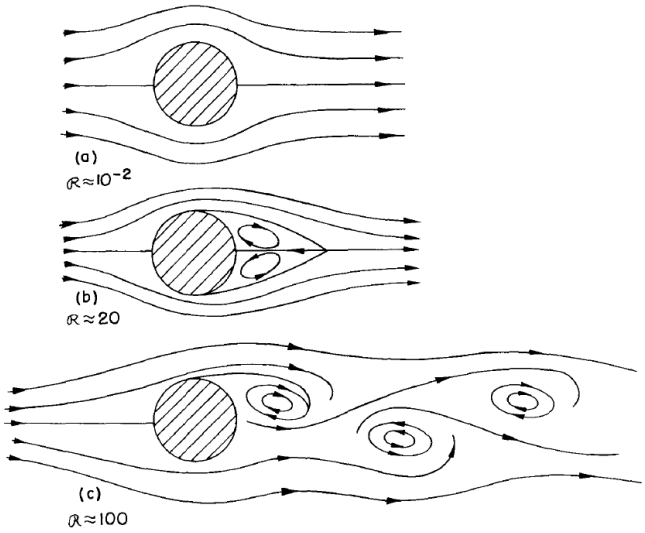

Figure 3.1: Flow past a cylinder for various Reynolds numbers [15]

The Navier-Stokes equation can be decomposed into different parts which contribute to different elements of the fluid flow. From this scaling it follows that the ratio of inertia terms to the viscous terms scales as the Reynolds number

$$Re = \frac{\text{inertial forces}}{\text{viscous forces}} = \frac{\rho_f \ u \ L}{\eta} \tag{3.1}$$

Here is ρ_f the density of the fluid, u is the speed of the fluid. L is the characteristic length scale, which in case of a sphere is about its diameter and η is the dynamic viscosity. The Reynolds number of our experiment can be estimated using this equation

$$Re = \frac{\rho_f \ u \ L}{\eta_w} = \frac{10^3 \ \frac{kg}{m^3} \ 10^{-3} \ \frac{m}{s} \ 10^{-5} \ m}{10^{-3} \ \frac{kg}{m \ s}} = 10^{-2} \tag{3.2}$$

The resulting Reynolds number is very low, so that the inertia terms of the Navier-Stokes equation may be neglected. The resulting flow is called Stokes flow or creeping flow, where the viscous forces dominate over the inertial forces. In case of an incompressible Newtonian fluid, the Stokes equations can be written as

$$- \bigtriangledown p + \eta \bigtriangledown^2 \vec{u} = 0 \tag{3.3}$$

$$\bigtriangledown \cdot \vec{u} = 0 \tag{3.4}$$

The Stokes flow equations are a great simplification compared to the complete Navier-Stokes equations, and the only variables are the pressure $\vec{p}$, the viscosity η and the velocity $\vec{u}$ [5, 39]. The properties of Stokes flow are discussed in the next section.

3.1.2 Stokes flow

For low Reynolds numbers the fluid flow can be calculated using the Stokes equation, in which viscous forces are dominant. This viscous or Stokes flow has the following properties:

- Instantaneous. The flow has no dependence on time. Given the boundary conditions the flow can be found without knowledge of the flow at any other time.
- Linear. The equation is linear, so that the response of the flow will be proportional to the applied forces. Linearity also means that the superposition principle can be applied, individual solutions may be added to calculate their combined effect.
- Time-reversible. A time-reversed Stokes flow solves the same equations as the original Stokes flow. If the same movement is performed in reversed direction, the original fluid situation is achieved [5]. An example of this is shown in Figure 3.2

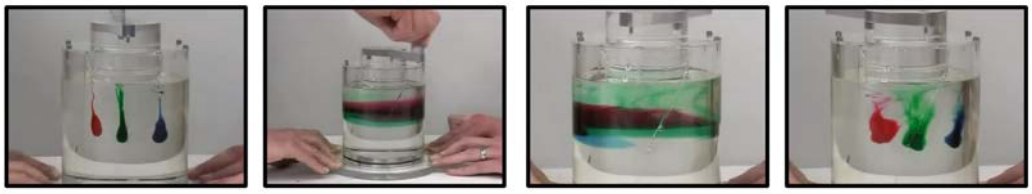

Figure 3.2: Stills of a video showing Stokes flow. Three different colors are inserted into a very viscous fluid. The inner cylinder is turned clockwise and then it is turned anti-clockwise for the same amount of turns. In the last still it is shown that the colors are separated as in the original situation. [3]

3.1.3 Drag of moving bead

The magnetic force causes the bead to circle around the disks. The bead is moving through a liquid (an aqueous solution), therefore it will feel some drag or resistive force. Ideally the bead follows the rotation frequency until the drag force is larger than the magnetic driving force. In this section an estimation is made of the drag force of a moving bead in water.

Free space

A minimum value for the drag force can be obtained by calculating the drag of a sphere in free liquid space. The drag force of Stokes flow along a sphere is algebraically solved, and the following equation holds for this force

$$\vec{F}_d = -6\ \pi\ \eta_w\ R_b\ \vec{u} \tag{3.5}$$

where η_w is the viscosity of water, R_b is the radius of the sphere and $\vec{u}$ is the velocity of the sphere. The drag force is always directed such that it opposes the movement. The linear property of Stokes flow is present, the drag force is linear with the velocity. [25, Page 289-291]

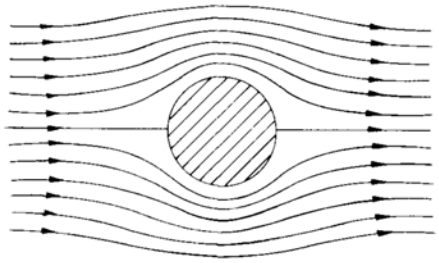

Figure 3.3: Stokes flow around sphere [15].

The flow lines of the Stokes flow around a sphere are shown in Figure 3.3. The drag force scales proportionally to the velocity u and to the sphere radius R_b.

Close to wall

In the previous section the drag force of a sphere in free space is shown. Movement near a wall increases the drag force, leading to a correction factor λ, which takes this extra wall drag into account. This factor is a function of the distance to the wall δ, see Figure 3.4. The expression for the drag force becomes

$$\vec{F}_{d,wall} = -6\ \pi\ \eta\ R\ \vec{u}\ \lambda(\delta) \tag{3.6}$$

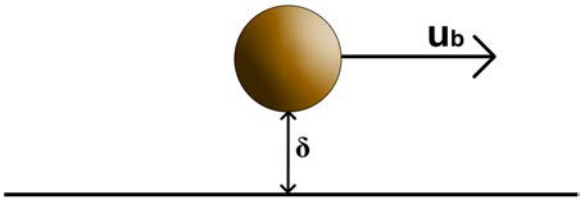

Figure 3.4: Sketch of sphere with velocity $\vec{u}_b$ at a wall distance δ.

There exist different models for this extra drag factor near a wall. The theory of Faxén is chosen, since this theory models the drag force in the form of a rather simple polynomial function [18]. The correction factor can be expanded to a fifth order polynomial function, but here only the first order approximation will be used

$$\lambda(\delta) = \left[1 - \frac{9}{16}\left(\frac{1}{1+\frac{\delta}{R_b}}\right)\right]^{-1} \tag{3.7}$$

where δ is the gap-width between the bead and the wall. The smaller the wall gap becomes, the larger the drag force. The correction factor doubles the drag force when the gap-width δ is

equal to $\frac{1}{8}R_b$. With a constant rotation frequency the velocity is constant, therefore the drag force on the bead has the largest value near the side wall.

3.2 Fluid displacement

To make an estimation of the net fluid velocity in the channel, different models can be used. In this section different models are presented and discussed, including their pumping speed and scaling properties. Also some simulations have been performed to make a better prediction of the flow profile in the channel.

3.2.1 Pressure approximation

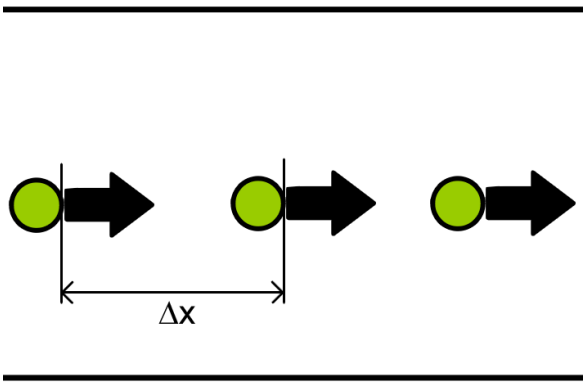

Figure 3.5: A series of spheres moving with separation distance Δx.

First the average channel velocity is calculated by assuming a flat channel where the moving spheres create a pressure difference along the channel. Consider a sphere moving in a microchannel with a velocity $\vec{u}_b$ parallel to the wall, see Figure 3.4. The magnitude of the drag force on the sphere is equal to the force exerted on the fluid. If the friction with the walls is neglected, the drag force is equal to a moving sphere in free space as shown in Eq. 3.5. The average pressure difference Δp in the channel is the force F_d divided by the cross-sectional area of the channel A_c.

$$\Delta p = \frac{F_d}{A_c} = \frac{F_d}{h\ w} \tag{3.8}$$

where the height of the channel is h and the width of the channel is w. Suppose a series of beads separated by a distance Δx generate a flow in the channel, see Figure 3.5. In flat microchannels the average fluid flow $\overline{u_c}$ is dependent on the pressure gradient, the viscosity η and the channel height h [13]

$$\overline{u_c} = \frac{h^2}{12\ \eta}\frac{\Delta p}{\Delta x} \tag{3.9}$$

With Eq. 3.5, Eq. 3.8, and Eq. 3.9 the ratio between the average channel liquid speed $\overline{u_c}$ and the speed of the bead u_b can be calculated.

$$\frac{\overline{u_c}}{u_b} = \frac{h^2}{12\ \eta}\frac{6\ \pi\ \eta\ R_b}{\Delta x\ h\ w} = \frac{6\ \pi}{12}\ \frac{h}{w}\ \frac{R_b}{\Delta x} \tag{3.10}$$

This rough approximation gives some insight in the magnitude and scaling of the pumping motion. The channel velocity is not dependent on the viscosity. A wider channel will decrease the flow rate, since there is more volume to displace. A higher channel will increase the flow rate (less resistance), however under the condition that the flat channel approximation still is valid. Larger beads will displace more fluid, especially when they are placed close to each other (small Δx).

3.2.2 Asymmetry

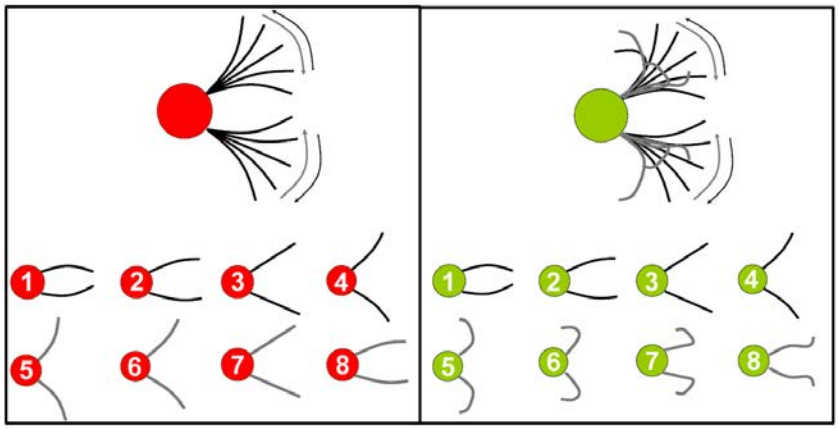

Figure 3.6: A symmetric bacterium will not swim (red), since the forward stoke (black) is equal to the backward stoke (gray). However an asymmetric bacterium will swim (green), because the backward stroke is different from the forward stoke. [5]

To create a net fluid displacement by a pumping or swimming motion, some asymmetry must be present in the performed motion. An example is the bacteria shown in Figure 3.6. The red bacterium has the same forward as backward stroke, it does not generate a net fluid displacement. The green bacterium has a different backward stroke, so it will create a net fluid displacement in one direction, the bacterium is swimming.

The same principle holds for the pumping motion of a rotating sphere in a microchannel, asymmetry is required to pump fluid into one direction. In other words, the volume displacement during the forward stroke, must be different from the volume displacement during the backward stroke.

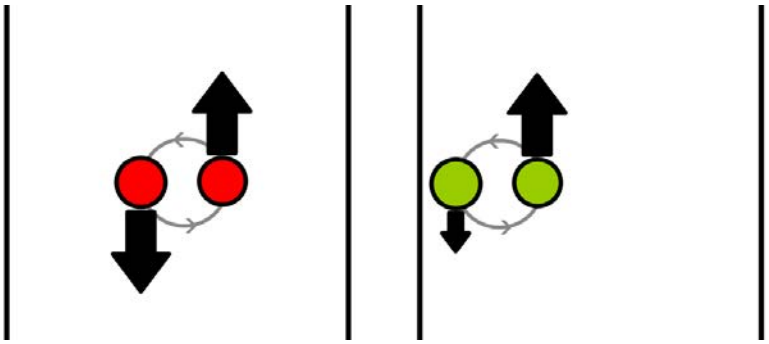

Figure 3.7: A symmetric bead setup will not have a net fluid displacement (red), but an asymmetric bead setup will displace fluid (green).

A solution not affecting the pumping motion, is to place the moving sphere near the side wall of the channel. A schematic picture of pumping is shown in Figure 3.7, and the idea is analog to the swimming of the bacterium. The red bead does not produce a net volume displacement, since the forward stoke produces the same displacement as the backward stroke. The green bead does however produce a net volume displacement, since the forward stoke is approximately the same as the red bead, but the volume displacement of the backward stroke is much smaller. The ratio between these two volume displacements mainly depends on the distance to the wall, therefore this factor mainly influences the pumping efficiency. The magnitude of the volume displacement depends on the size and the path of the bead. The position and the path are

determined by the place and the size of the magnetic disks in the channel. The pumping speed is the volume displacement multiplied by the rotating frequency of the bead. To investigate the pumping efficiency, a pumping efficiency η_p is defined

$$\eta_p = \frac{V_f - V_b}{V_f} \tag{3.11}$$

Here V_f is the volume displacement during the forward stroke and V_b is the volume displacement during the backward stoke. To optimize the efficiency, the volume displacement during the backward stroke V_b has to be minimized. If the two strokes take the same amount of time and have the same pumping curve, the efficiency can be written as a fraction of fluid velocities

$$\eta_p = \frac{|u_f| - |u_b|}{|u_f|} \tag{3.12}$$

Here $|u_f|$ is the fluid pumping velocity during the forward stroke and $|u_b|$ is the fluid pumping velocity during the backward stroke. From this it follows that the fluid velocity caused by the backward stroke must be as small as possible compared to the forward stroke.

3.2.3 Flow profile integration

An approximation of the relative difference between the forward and backward stoke can be obtained by integrating the velocity profile of a moving sphere in liquid, over two different surfaces. As integration boundaries for these surfaces the edges of the channel are chosen, whereby in one situation the bead is located in the middle of the channel and in the other situation the bead is located near the edge of the channel. The no-slip condition of the wall is completely neglected, nevertheless it will give an estimation for the asymmetry between the two situations as shown in Figure 3.7. The result will give an indication for the pumping efficiency of the system. The Stokes flow for a moving sphere in the Cartesian coordinate system is derived in Appendix A.8. For the velocity component in the direction of the moving bead holds

$$u_x = u_b - u_b\, cos^2(\theta)\left(1 - \frac{3R}{2r} + \frac{R^3}{2r^3}\right) + u_b\, sin^2(\theta)\left(1 - \frac{3R}{4r} - \frac{R^3}{4r^3}\right) \tag{3.13}$$

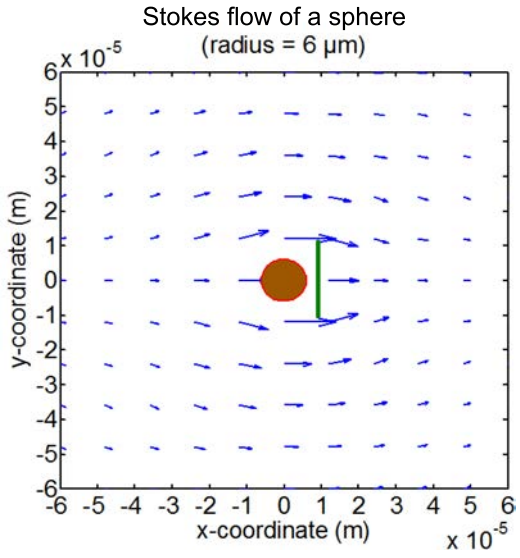

Figure 3.8: A schematic of the flow profile around a sphere calculated using Eq. A.44 and Eq. A.45, the integration boundary of Eq. 3.14 is displayed as a green line.

The ratio between the average channel velocity and the bead velocity can be calculated by integrating the flow profile u_x (Eq. 3.13) over the channel boundaries, and dividing by the channel surface. A schematic of this integration can be seen in Figure 3.8.

$$\frac{\overline{u_c}}{u_b} = \frac{\iint u_x(x,y,z)\mathrm{d}A}{A_c\ u_b} = \frac{1}{h\ w\ u_b} \int_{h/2}^{-h/2} \int_{z-w}^{z} u_x(x,y,z)\ \mathrm{d}z\ \mathrm{d}y \Bigg]_{x=x_0} \tag{3.14}$$

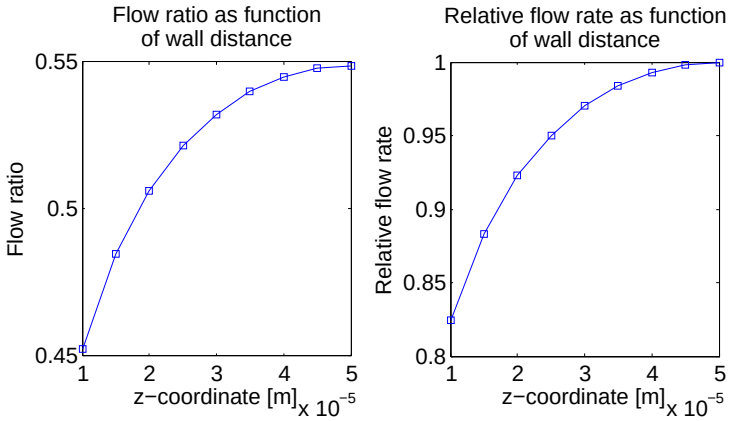

Figure 3.9: The flow velocity ratio of Eq. 3.14 as a function of the distance from the wall (left-hand side), and the relative decrease of flow near the wall compared to the middle of the channel (right-hand side).

This integral was evaluated numerically[1], since it was not possible to find an algebraic solution. The result of the numerical evaluation is shown on the left in Figure 3.9. The z-coordinate is the position of the center of the microsphere. A channel width w of 100 μm was chosen, so $z = 50$ μm is in the middle of the channel and $z = 0$ μm is on the edge of the channel. The other parameters used are: channel height h of 15 μm, bead radius R_b of 6 μm, the integration distance x_0 is chosen as $1\frac{1}{2}R_b = 9$ μm.

The average channel flow rate in the middle of the channel is 0.55 times the bead velocity u_b, this is a large flow rate, caused by neglecting the slip of the walls. The pressure approximation of the previous section gave an average channel flow rate of 0.01 u_b with the same parameters and a sphere spacing Δx of 100 μm. Calculating the exact flow profile with the wall slip condition taken into account is beyond the scope of this assignment. In simulations the flow profiles for the different situations are further evaluated, see next section.

The asymmetry in the average channel velocity was obtained by the integration of the flow profile and is shown in Figure 3.9 on the right. The relative decrease in flow velocity of a sphere near the wall is 82% compared to the flow velocity in the middle of the channel. This means that the pumping efficiency, as defined in Eq. 3.12 is 18%. This efficiency can be optimized by performing the forward stoke in the middle of the channel and the backward stoke as close to the wall as possible. The risk is that the drag force near the wall can become too large, disturbing the rotational motion of the bead around the disk (see Section 3.1.3). The flow ratios for other channel heights were also evaluated, but virtually no dependence on the channel height was found.

3.2.4 Simulation of flow profile

In order to investigate the flow profile, simulations of moving beads were done. First straight moving spheres were simulated in 3D, to obtain the flow profile of the sphere moving in the

[1]Matlab R2011b was used to evaluate the integral with a number of parameters, it was performed in a parallel for-loop (parfor) to profit from the multicore processor computing power minimizing the computing time.

channel. Next a simulation in 2D is performed to get an estimation of the time dependent flow profile of a rotating bead.

Sphere moving straight in channel

A stationary simulation of a sphere with a velocity parallel to the channel wall is performed in COMSOL[2]. For this three dimensional simulation a channel with a length of 200 μm and a sphere radius of 6 μm are chosen. The boundary condition for the outlets is 1 bar (10^5 Pa). The resistance of the channel is influenced by the channel length and therefore also the flow rate magnitude at the end of the channel. The simulation results of a sphere moving in the middle and near the wall of the channel are shown in Figure 3.10 and Figure 3.11.

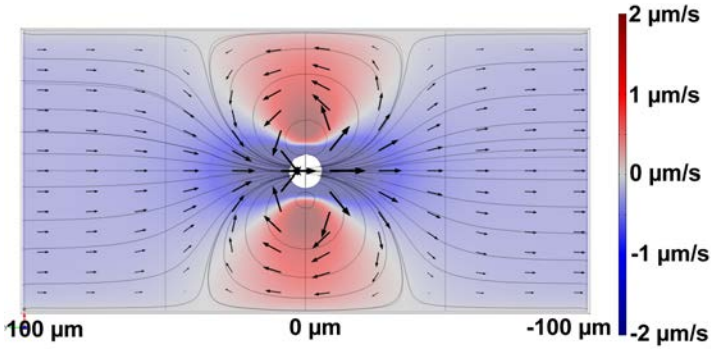

Figure 3.10: Stokes flow of a sphere moving parallel to the wall in the middle of the microchannel (top view). The color indicates the magnitude of the flow in the horizontal direction, the arrows indicate the direction of the flow.

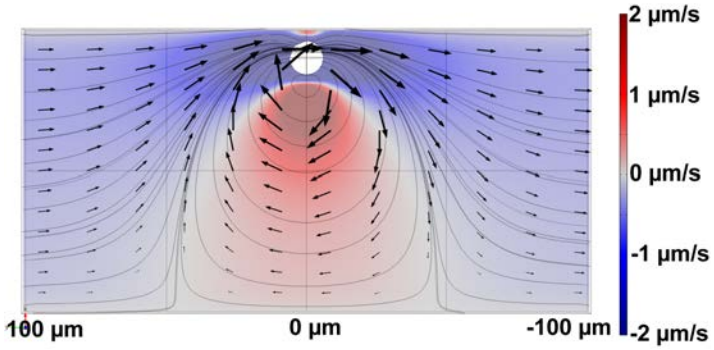

Figure 3.11: Stokes flow of a sphere moving parallel to the wall close to the side wall of the microchannel (top view). The color indicates the magnitude of the flow in the horizontal direction, the arrows indicate the direction of the flow.

A net fluid flow in the direction of the sphere of 0.02 times the bead velocity u_b was generated. For the flow profile of the sphere moving in the middle of the channel two vortices are formed. These vortices decrease the net flow, since they have a negative contribution to the flow. The flow profile of the sphere moving close to the wall has one vortice. The sphere moving closer to the wall, feels a larger drag force, tut this force acts on less volume, so in total less volume is displaced. The flow profile of two moving spheres in opposite direction is also simulated, see Figure 3.12. The largest part of the flow at the end of the channel is canceled out. The time-dependent pumping motion is investigated in the next section.

[2]COMSOL Multiphysics 4.2a using the Creeping flow (spf) physics module, incompressible flow and neglecting inertial terms.

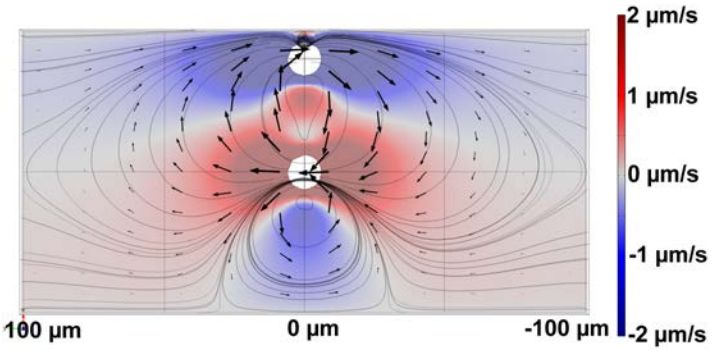

Figure 3.12: Stokes flow of two spheres moving in opposite direction (top view). The color indicates the magnitude of the flow in the horizontal direction, the arrows indicate the direction of the flow.

Rotating sphere

A time-dependent simulation of the pumping motion of a rotating sphere was done in COMSOL[3]. To simulate the bead fluid interaction the fluid-solid module was used, and a force was applied to the bead causing the fluid to move. The simulation was performed in two dimensions, since the situation is symmetric in the z-direction (depth). The moving sphere makes the simulation quite challenging, nevertheless the 2D simulation was successful. A 3D simulation however was too complex, mainly because of meshing issues. A channel length of 250 μm and a width of 100 μm were chosen, and the outlet pressures were 1 bar (10^5 Pa). The sphere was modeled as a solid material, on which a very strong force in a circular motion was exerted. Since the sphere is moving, autoremeshing was required during solving. The simulation result of the flow on 8 moments of one period is shown in Figure 3.13.

During the forward stroke a fluid flow with some small vortices is generated. During the backward stroke a smaller fluid flow in the other direction is generated. When the bead is moving perpendicular, there is no flow at the end of the channel. To investigate the net pumping motion, the velocity in the horizontal direction is averaged over the end of the channel. The result of this averaged flow as a function of time can be seen in Figure 3.14.

There is a clear asymmetry in the fluid displacement of the forward and backward stoke. The flow rate during the forward stoke is -16.9 $\mu m/s$, and the flow rate during the backward stoke is 11.3 $\mu m/s$. This gives an average simulated pumping efficiency of 33%.

[3]COMSOL Multiphysics 4.2a using the Fluid-Structure Interaction (fsi) physics module, incompressible flow and neglecting inertial terms. Solver settings: Fully coupled, direct MUMPS solver and automatic remeshing with a minimal mesh quality condition.

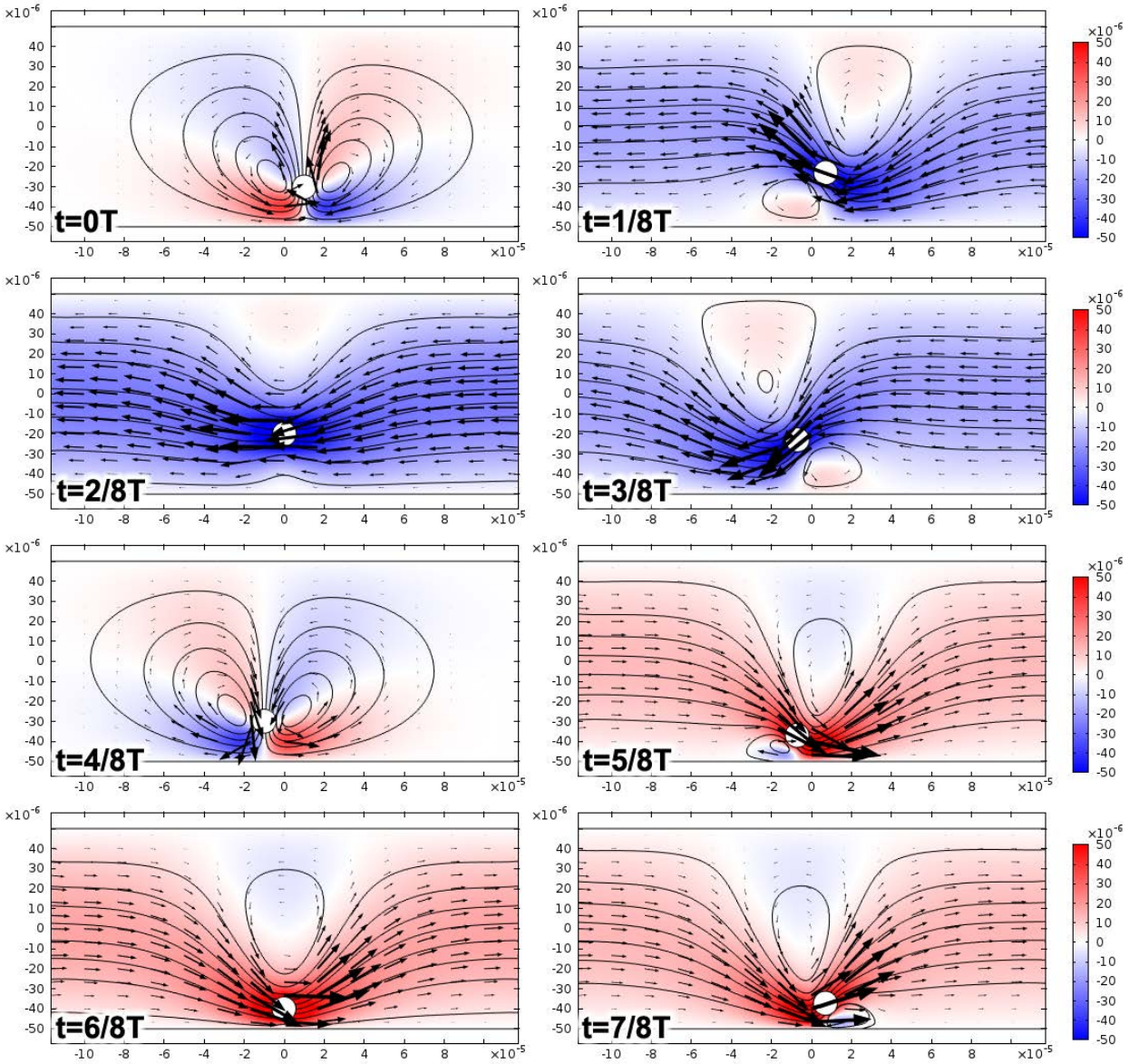

Figure 3.13: Stokes flow of a circle making a circular motion in the microchannel (2d simulation). The color indicates the magnitude of the flow in the horizontal direction, the arrows indicate the direction of the flow.

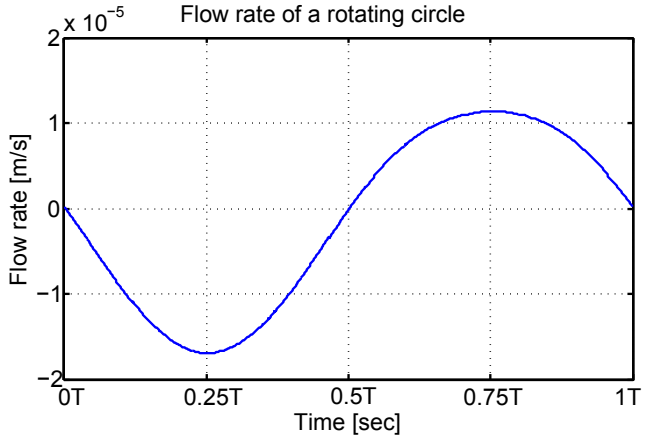

Figure 3.14: The average output flow of the moving circle (2D simulation) at the end of the channel as a function of time, the average flow is $-5.6\ \mu m/s$.

3.2.5 Summary on fluid displacement

The parameters determining the pumping speed have been derived by analyzing the flow in the channel. A very low Reynolds number was calculated, so the flow regime is laminar or Stokes flow: viscosity dominates inertia effects. In Stokes flow it is important to have an asymmetry in the moved volume to generate a net pumping effect, since no asymmetry is present due to turbulence effects. In the chosen pumping system the pumping speed is depending on the distance from the wall, the size of the bead and the rotation frequency.

To maximize the net pumping flow it is essential to optimize the pumping efficiency. The efficiency per stroke is dependent on the distance between the sphere and the side wall. The forward stoke of the sphere should occur in the middle of the channel and the backward stoke as close to the wall as possible. When the bead is closer to the wall more force is required to move it with the same velocity, which may disturb the circular motion. A theoretical pumping efficiency of about 18 % was calculated, whereas the simulated pumping efficiency was 33%. A cause for this difference in efficiency is the neglect of the slip of the wall in the calculation, they are however in the same order of magnitude.

3.3 Maximum rotation frequency

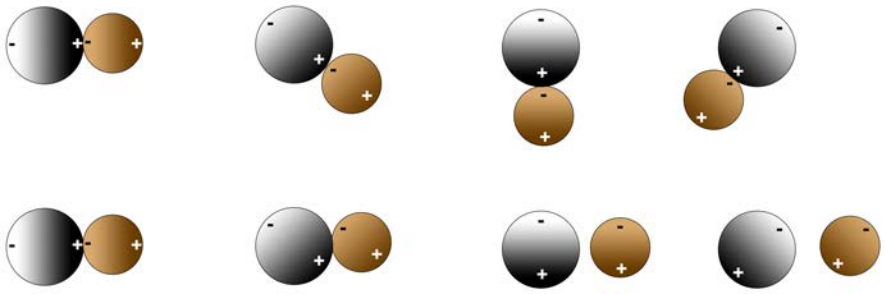

Figure 3.15: In the top the situation a paramagnetic isotropic bead and below the situation of a ferromagnetic or anisotropic bead is behaving as a permanent magnet.

As described earlier, the magnetic microspheres follow the rotating magnetization of the permalloy disk. When the magnetic field is very strong, the beads can follow the magnetization. However starting from a certain frequency the circular motion of the bead is disturbed. This is mainly caused by three components:

- With an anisotropy in the magnetic microsphere (an easy axis) or a remanent magnetization, a torque on the sphere arises [24]. When this torque starts to dominate the magnetic force exerted by the poles of the magnetized disk, it disturbs the motion, as shown in Figure 3.15. The result is that the microspheres circle around the disk and spin around their axis, leading to a hypotrochoidial path[4] as shown in Figure 3.16.
- When the magnetic material of the disk is of bad quality, it is possibly that the disk can not follow the rotation of a magnetic field for higher actuation frequencies. The magnetic domains or their magnetization can be disturbed such that near the edge no strong poles are present. The result is a lower magnetic force on the sphere. A lower force can also be caused by bad magnetic properties of the magnetic microsphere.
- When the sphere is moving close to the wall, the drag force of the liquid is larger for a constant frequency. Therefore more likely is that the movement of the sphere will be disturbed near the wall.

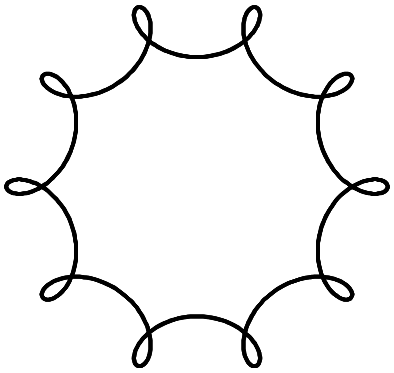

Figure 3.16: A drawing of a hypotrochoid (a=3 b=0.3 h=0.5).[43]

It is difficult to find an exact expression for the maximum rotation frequency, since it will depend on very specific material parameters. And even if all these parameters would be known, this should be simulated with a finite element method because of the complexity, which is beyond the scope of this assignment. Nevertheless with the given relations it is possible to optimize the maximum rotation frequency. In practice also the cleanness of the permalloy disks is important, since a larger distance between disk and sphere causes a smaller force on the sphere and roughness causes extra friction for the rotation motion. In theory it is possible that a small phase delay is present between the external magnetic field and the movement of the sphere, but in practice this is difficult to measure and a too large phase delay disturbs the circular motion.

[4]A hypotrochoid is a roulette traced by a point attached to a circle of radius b rolling around the inside of a fixed circle of radius a, where the point is at a distance h from the center of the interior circle. The parametric equations are: $x(t) = (a-b)\cos(t) + h\,\cos(\frac{a-b}{b}t)$ and $y(t) = (a-b)\sin(t) - h\,\sin(\frac{a-b}{b}t)$.[43]

Chapter 4

Chip design and fabrication

In order to do experiments a microfluidic chip is designed and fabricated. The theory of Chapter 2 and Chapter 3 has been the basis for the design of the chip. Based on a set of requirements the design choices are explained. Next the fabrication methods are explained, including the problems encountered with manufacturing with the permalloy.

4.1 Design choices

The channel and disk geometry must be tuned to the bead size. The chip can be designed freely, whereas the choice in the sizes and properties of magnetic beads is limited. Many of the available magnetic microbeads have a diameter below 5 μm, for example the Dynabeads are only available in 4, 2 and 1 μm. For this reason the beads are chosen first and based on their size the chip is designed [21].

4.1.1 Chosen magnetic microspheres

The magnetic beads have to be large, since the magnetic force scales with their volume. Another requirement is that the remanent magnetization must be as small as possible, to achieve a high maximum rotation frequency of the circular motion (see Section 3.3), and therefore the beads must be superparamagnetic. A beneficial property would be if the beads are isotropic, since this improves the ability to follow the disk magnetization. The beads can then roll over the surface instead of being dragged over the disk surface. Another advantage would be if the beads are biocompatible, since a possible use of the system is the pumping of biological fluids.

Already available magnetic microspheres were the 12 μm Micromer beads[1], spherical magnetic polystyrene matrix particles. According to their datasheet they have a mass magnetization of 0.5 $\frac{Am^2}{kg}$ in a magnetic field H of 80 $\frac{kA}{m}$. They are coated with carboxylic acid (-COOH), the number of particles per ml is $5.1 \cdot 10^7$. The density of the beads is 1.1 g/cm^3 [34].

Later in the project 30 μm magnetic microspheres[2] were used for experiments. According to their datasheet they have different properties, a higher mass magnetization M of 4.3 $\frac{Am^2}{kg}$ in a magnetic field H of 80 $\frac{kA}{m}$. They are consisting of magnetic polylactic acid particles, which dissolves in water at higher temperatures. Their coating is also carboxylic acid (-COOH), the number of particles per ml is $5.5 \cdot 10^5$ and their density is 1.3 g/cm^3. Based on these specifications, it seemed that these beads have a higher density magnetic material in their matrix. These beads were chosen, since they possessed a good magnetization and a large diameter. The disadvantage of the large beads is that they are not very monodisperse, some beads were small (about 15 μm), and some beads were aggregated (sticking together) permanently. Also in the magnetic bead solution some debris was present. Another problem of these beads is that the matrix consists of polylactic acid, which dissolves in water at higher temperatures. They must therefore be stored at 8 °C to prevent dissolving the beads [33].

[1] Micromer-M particles (product-no: 08-02-124) produced by the German company Micromod Partikeltechnologie GmbH, http://www.micromod.de

[2] PLA-Particles -M particles (product-no: 12-02-304) produced by the German company Micromod Partikeltechnologie GmbH, http://www.micromod.de

4.1.2 Requirements for chip

The most critical part to get a functional pumping system is the array consisting of permalloy disks. The permalloy disks have to be thick enough to generate sufficient deformation of the magnetic field, creating a strong enough attracting force on the beads. For this reason the quality of the permalloy has to be good. A large saturation magnetization (strong magnetic poles) exerts more force on the beads. A large force on the beads has the effect that the beads can follow the rotation magnetic field up to a higher frequency, a higher bead velocity gives proportionally a larger pumping velocity. The permalloy disks must be as thick as possible, however there is a practical limit due to stress in the layer and other deposition limitations. Stress in the permalloy will deteriorate the magnetic properties, but may also cause delamination.

Beads are placed close to each other to optimize the pumping action. However if the beads are placed too close, the magnetic field of the neighboring beads is disturbing the circulating motion around the permalloy disk.

4.1.3 Chosen design

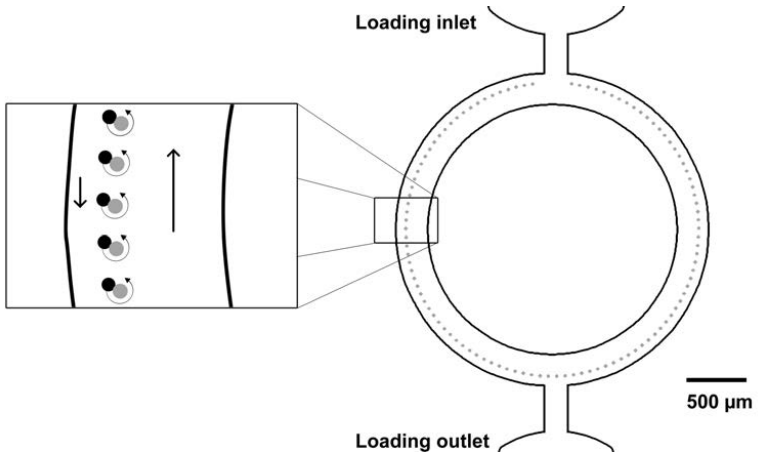

Figure 4.1: The closed pumping channel with permalloy disks (gray) and magnetic microspheres (black). The arrows indicate the direction of expected flow.

The design consists of three masks for lithography:

- Channel mask: on this mask the channel design is drawn. In case of anisotropic etching (DRIE) the drawn channel width on this mask is equal to the etched channel width. In case of isotropic etching the etched channel width is the drawn channel including round underetched sidewalls. If there are no significant surface etching effects, the width of the etched round sidewall is equal to the channel depth.
- Permalloy mask: this mask determines the position and the shape of the permalloy patterns. When lift-off is used, the patterns are equal to the drawn patterns. In case of wet etching, there is some underetching of the patterns. This causes the patterns to be smaller than drawn, on the edges of the patterns round isotropic underetching occurs. When the same mask is used for wet etching, the disk radius is reduced by the thickness of the permalloy layer.
- Powderblasting mask: on this mask the loading in- and outlets are drawn. It is determining the positions of the holes, to fill the chip with liquid and beads.

The first design was based on the 12 μm microspheres, and drawn in CleWin[3]. The complete mask design can be found in Appendix B, a schematic of the design can be seen in Figure 4.1.

[3]CleWin 4.3, layout editor for mask designs

No.	Set	Wafer type	Channel depth	Permalloy thickness	Permalloy side
1	-	glass	-	500nm	-
2	-	glass	-	132nm	-
3	1	glass	15 μm	100nm	bottom
4	1	glass - silicon	15 μm	120nm	bottom
5	1	glass - silicon	15 μm	90nm	bottom
6	2	glass - silicon	40 μm	480nm	top
7	2	glass - silicon	40 μm	460nm	top
8	2	glass - silicon	40 μm	295nm	top

Table 4.1: Summary of wafer manufacturing information.

The depth of the channels of the first design was 15 μm and the width was 100 μm, etched anisotropically with straight walls. The distance between two disks was set to 45 μm, the distance between the disk and the side wall of the channel was 15 μm. The outside diameter of the circular channel was 2.5 mm. The drawn disk diameters were 25 μm, 15 μm and 5 μm, placed in separate channels near the in- or outside side wall of the channel. On a second chip other permalloy patterns were placed, rings with a diameter of 30 μm and a hole of 10 μm spaced 60 μm from each other. Furthermore, strips were drawn with a width of 8 μm spaced 10 μm.

Based on the 30 μm beads a new design was made. For this second set only a new channel mask was made. The channel depth was increased to 40 μm. The drawn wall-disk distance was increased to 20 μm. The space to move for the magnetic bead is this drawn distance added by the round sidewall.

4.2 Fabrication

Wafers have been processed using the mask design in Appendix B. Two sets of wafers were made, because the maximum rotation frequency achieved with the first design achieved had to be increased in a second. The first set was produced in October and November 2011, the second set was produced in January and February 2012. The produced wafers and their manufacturing process are shortly discussed. Drawings of the used fabrication process can be found in Appendix C. An overview of the fabricated wafers with their different fabrication parameters is given in Table C.1. A summary of the wafer information can be found in Table 4.1.

Improvements made in the design and process of the second set with respect to the first set are:

- The thicker permalloy film, leading to much more force on the bead and therefore a higher pumping rate.
- A new channel design to accommodate larger magnetic beads resulting in a larger magnetic force.
- The permalloy was placed on the top wafer, this way the magnetic force due to the quadrupole is in the same direction as the magnetic force due to the permalloy disk. For an image with the two force vectors, see Figure 4.2 and Figure 4.3.

4.2.1 Fabrication processes

To fabricate the chips several steps were performed: the channels were etched, inlets were created and permalloy patterns were placed. To make a closed reliable system, the system then was bonded. Next the wafers were diced into separate chips.

To produce the channels and holes in the glass or silicon wafer three options were used:

- The channels of the first set of wafers were created by an anisotropic etching method. Deep Reactive-Ion Etching was used to create channels with a high aspect ratio, see Figure 4.2. The disadvantage of this method was that the channel depth is limited to approximately 20 μm and the bottom of the created channels was not very smooth.

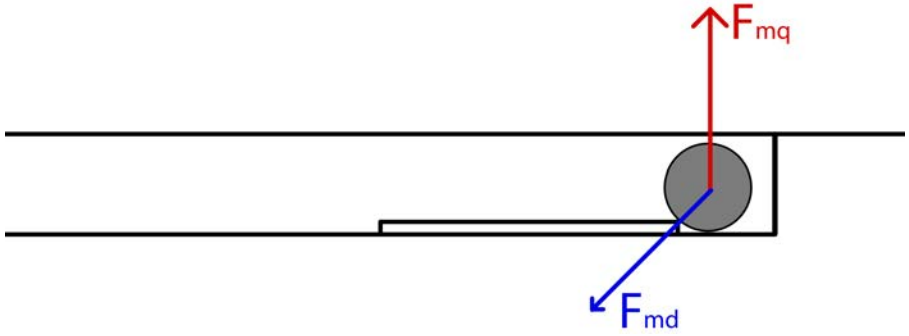

Figure 4.2: The cross-section of the channel of the first set design.

- The channels of the second set of wafers were created by wet etching, this is an isotropic etching method. The etchant removed the substrate in all the directions with the same speed, creating round sidewalls. The advantages are that the channels are smooth and it is a well controllable process. The disadvantage is the low aspect ratio, steep walls can not be produced using this method. An attempt was made to design the chip such that the beads placed as close to the wall as possible, with a safety margin. The problem of the isotropic etched wall is that there is some leakage of liquid through the upper corner of the round side wall, reducing the pumping efficiency.

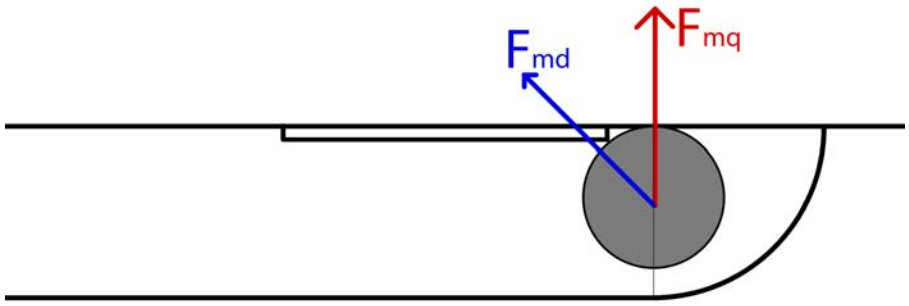

Figure 4.3: The cross-section of the channel of the second set design.

- The holes for the in- and outlets were created using powder blasting. With this method the surface is bombarded with aluminum oxide particles, creating a hole in the wafer. The advantage of this is the potentially large depth and high aspect ratio. The disadvantage is the roughness of the surface near the hole, which is a possible cause for the stiction of beads.

The permalloy patterns were created by modifying the applied permalloy film with two methods:

- Lift-off was used for the patterning of the permalloy film of the first set of wafers. With this method first a layer of photoresist is spun on the wafer, the mask design is transferred by exposing the photoresist. A permalloy film is sputtered on the wafer, partly on the open areas the and partly on the photoresist. The exposed resist is then removed leaving the patterns of the design open. The drawback of this method is the limitation that it only works well using thin films.

- For thicker films of the second set a standard wet etching process and lithography was used. First an adhesive layer and then a film of permalloy are sputtered on the wafer, then the photoresist is spinned. The patterns are transferred to the resist using the same mask as used for the lift-off patterning, and the patterns are etched into the film. The disadvantage is that due to the underetching of the patterns, the resulting patterns are smaller than the drawn patterns.

After the channels were created and the permalloy patterns were placed, the top and bottom wafer were bonded to create a closed system with a non-oxidated permalloy layer. For this three different methods were investigated:

- For Wafer 3 the two glass wafers were attached to each other using *fusion bonding*. For this bonding method, the surfaces have to be very smooth for good bonding. A large force was exerted to force the wafers close to each other, and create a prebond by van der Waals forces. They were heated to high temperature (around 600 °C) to form a solid bond between the two interfacing surfaces. The high annealing temperature caused the hydrogen on the interfaces to diffuse away. Another effect of this high temperature is the softening of the glass, creating a better seal. The advantage of this method is a strong bond, the disadvantage is a marked quality deterioration of the permalloy due to this annealing step.
- For Wafer 4 up to 6, a glass wafer and a silicon wafer were bonded using *anodic bonding*. A picture of a bonded chip of Wafer 5 can be seen in Figure 4.4. For this method the two wafers are clamped together with electrodes and heated to about 400 °C. Next a high DC voltage ($> 1kV$) is applied between the electrodes, creating a high electric field in the wafers. The sodium ions in the glass wafer are displaced from the bonding surface by the electric field and high temperature. The depletion of ions near the surface of the glass makes the surface highly reactive with the silicon surface forming a solid chemical covalent bond. The two surfaces have to be smooth ($Ra < 0.7\ nm$) to create a good bond [31]. Fusion and anodic bonding result in a nearly equivalent bonding strength. The quality of the permalloy is less affected by this lower annealing temperature.
- Wafer 7 and 8 were bonded using *glue*, for which a thin film of glue (photocurable NOA) was applied and then the wafers were aligned. This method was performed at room temperature, which was beneficial for the quality of the permalloy. The drawback was the difficulty of alignment and the (partly) filling the channels with glue. Another drawback is that a glued bond is less robust than a bond using the previous bonding methods. Pictures for this chip assembly can be found in Appendix C.4.

4.2.2 Permalloy

During the fabrication of the permalloy patterns, some problems were experienced. The magnetic material was sensitive to annealing steps and the adhesion of the film was bad. Permalloy was chosen because of the large magnetization, however most magnetic materials are difficult to handle. Heating steps increases the magnetic coercivity (see Section 2.2.3). Internal stress can have a large influence on the magnetic properties. Also irregularities in the permalloy layer can lead to anisotropy in the material.

Wafer 1 was a test wafer to investigate the adhesion of the permalloy film to the glass substrate. A layer of approximately 500 nm was deposited, the result can be seen in Figure 4.5. The permalloy was released from the glass due to stress. Another problem was that the thick permalloy layer caused rapid contamination of the manufacturing systems.

To reduce the stress, a permalloy layer of only 132 nm was sputtered on a glass wafer (Wafer 2). During the sputtering was the wafer rotated, which should lead to a isotropic

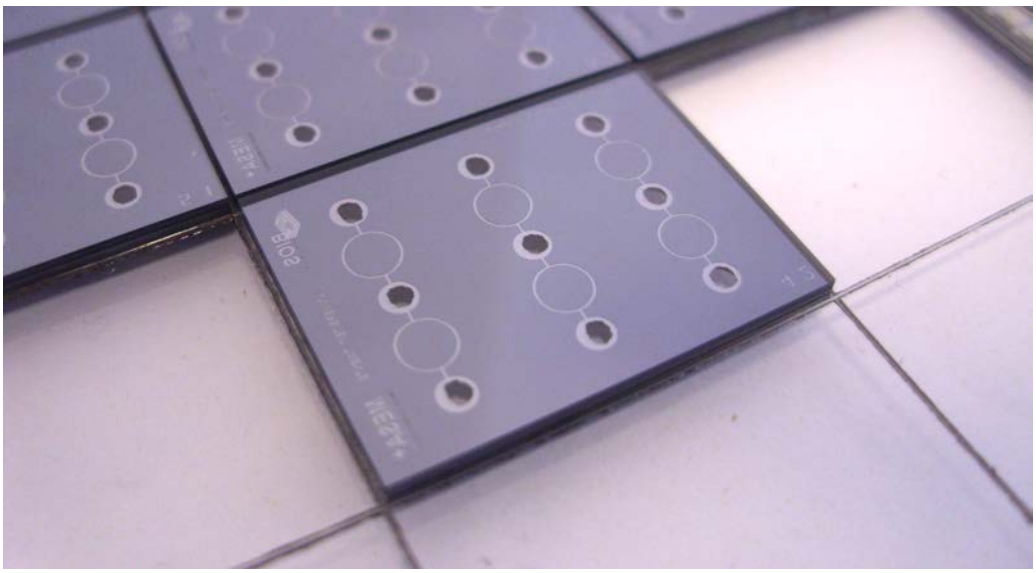

Figure 4.4: The bonded chip (Wafer 5).

Figure 4.5: Release of permalloy film due to stress.

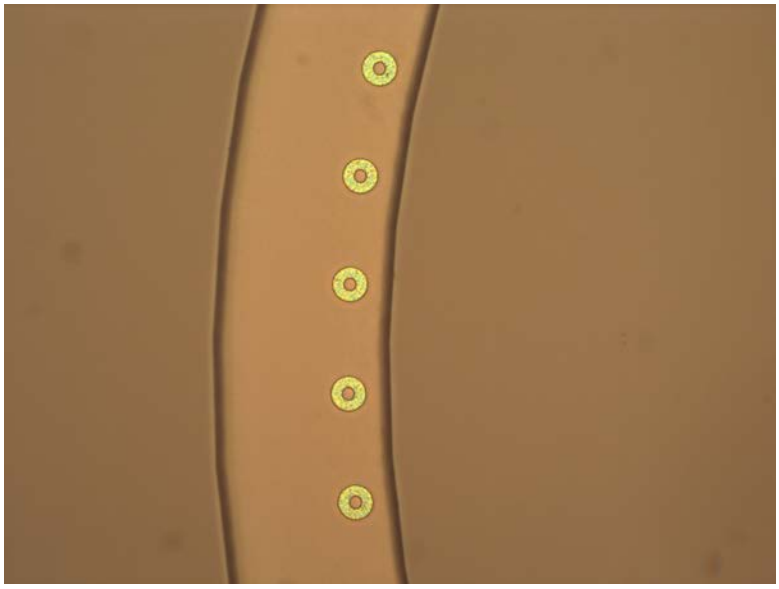

Figure 4.6: Strong oxidation of the permalloy patterns after bonding Wafer 3, the yellow color indicates oxidized metal.

uniform film of permalloy. The result was an isotropic layer of permalloy of good quality. Based on this result Wafer 3 was produced, whereby the patterns were created using lift-off. This was possible, since the permalloy layer was thin. For the pumping principle it is the most profitable to have steep walls, and anisotropic etching was therefore used to create steep channels with a depth of 15 μm. The two glass wafers were bonded together at 625 ^oC in an air atmosphere. This step caused the permalloy layer to oxidize (almost) entirely, and almost no magnetic effect was measured, see Figure 4.6.

To prevent the permalloy from oxidizing completely, subsequently the channels were etched in a silicon wafer. The advantage of the silicon to glass bonding is the lower process temperature of 425 ^oC. This bonding was performed in a vacuum, to reduce oxidation by reducing the influence of oxygen in air. The oxygen in the glass can still oxidize a certain depth of the permalloy layer, but the expectation is that this is only an surface effect with a depth of at maximum tens of nanometers. The resulting permalloy layer of Wafer 4 was of good quality.

Another option to prevent the permalloy from oxidating is adding a platinum covering layer on top, which was performed on Wafer 5. This procedure allowed the preservation of the magnetic quality of the permalloy. Beneficial is furthermore that the chip becomes biocompatible, since the biologically toxic nickel-iron alloy is shielded. The covering process was successful, but the permalloy layer was thin, so that the force on the magnetic beads was small.

Experiments showed that the maximum rotation frequency of the first set of wafers was too low. To improve this, the permalloy layer had to be thicker (see Section 3.3). A permalloy thickness of 480 nm was sputtered. The disadvantage of this thicker layer is that lift-off cannot be used, hence the patterns were created by wet etching. The disadvantage of wet etching is that the magnetic structure on the edges of the patterns can deteriorate, since the existing crystal is modified. Since the external magnetic field was applied from the top, the permalloy patterns were also placed on the top side of the channel to increase the magnetic force. Between the silicon wafer and the permalloy an adhesive layer was added. The goal of this layer was to improve the adhesion of the permalloy and to reduce the stress. The adhesion layer of chromium was etched using a standard etching step. However tantalum was difficult to remove, and an ion bundle bombardment etching method was required, which could possibly damage the permalloy layer. An adhesion layer of 10 nm should be sufficient[4]. In practice large surfaces of permalloy were released, see Figure 4.7. However the permalloy disks showed a good magnetic performance, see Chapter 6.

Figure 4.7: Sample partly covered by permalloy film (Wafer 6).

The permalloy film delaminated mainly during the cleaning process required for fusion or anodic bonding of the wafers. To circumvent this problem an attempt to bond the wafers with NOA-glue was carried out. Wafer 7 and Wafer 8 were thus not bonded at a high temperature, but glued[5] with NOA 81. This glue cures by exposing to strong UV-light. To get an uniform

[4]advice of Johnny Sanderink of the NE-group, who has experience with handling permalloy

[5]Verena Stimberg introduced me to the method of gluing chips with NOA.

layer, the NOA was spinned on an objective glass with spin coater: first 30 sec on 500rpm, then 30sec on 5000rpm. It was precured for 10 seconds with low UV intensity. After alignment the NOA was fully cured using high UV intensity [4]. The NOA had a too low viscosity, so that after placing the two parts on each other, the channels were almost completely filled with the glue. This was caused by the vacuum chuck in combination with the silicon chip with the powder-blasted holes, creating a low pressure in the channels. Because of this low pressure in the channels, the glue filled the channels. No convenient method was found to circumvent this problem.

Another attempt on Wafer 7 and Wafer 8 was carried out with a more viscous glue, Loctite 415. The silicon chip was placed on the vacuum chuck of the chip aligner shown in Appendix C.4. Under the chip plastic foil was placed, to avoid glue contaminating the chuck. After this the chips were aligned, placed onto each other, and a small drop of glue was placed along the edge of the chip. During the chip design it was not taken into account that individual chips had to be aligned, no alignment marks were drawn on the design of the chips. Therefore it was difficult and time consuming to align the chips correctly, whereby it was critical to place the magnetic patterns exactly in the right position in the channel. Also the problem of glue in the channels was still present, however less problems were experienced with the Loctite glue. An overview of the fabricated wafers with their different fabrication parameters is shown in Table C.1.

Chapter 5

Experimental

In this chapter the setup for the experiments is discussed. With the chosen quadrupole and amplifier a rotating magnetic field is generated, causing the magnetization in the permalloy disks to rotate. When magnetic beads were loaded into the chip, they could therefore be moved by placing the quadrupole on the microscope stage. The movement of the beads then displaces the fluid with indicator beads. With a camera images of the moving indicator particles were recorded. Samples were furthermore made to study the magnetization properties of the permalloy films and the magnetic beads.

5.1 Magnetization measurements

Figure 5.1: The VSM analyzing the magnetization of sample.

The magnetization of the materials was investigated using a Vibrating Sample Magnetometer or VSM[1], see Figure 5.1. This is a computer-controlled measurement system which is capable of characterizing the widest variety in magnetic samples [35]. The sample is vibrating in a strong electromagnet, and around the sample four pick-up coils are located. The signals of these coils are amplified using a lock-in amplifier. For more pictures of the VSM see Appendix D.

To measure the magnetic properties ofthe magnetic films in the VSM, samples of 5x5 mm were made. Some test structures were present on the side of the wafer. Of the first generation of wafers VSM samples were fabricated by cutting the samples into pieces with a carbon fiber cutting pen[2]. Samples of the second generation were made by mechanically dicing the test structures. The test structures on the wafer were used for this measurement to ensure the same

[1]Vector Magnetometer Model 10 VSM, introduction by Thijs Bolhuis, TST-group
[2]PROSKIT INDUSTRIES - DK-2026N - SCRIBE, CARBIDE FIBRE

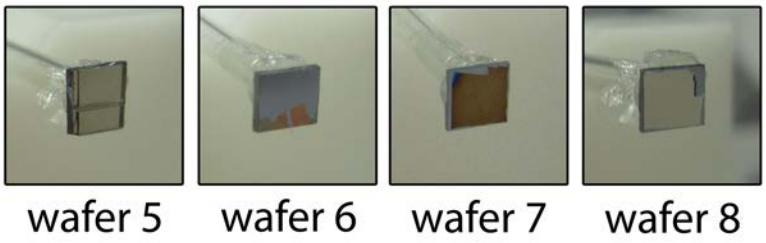

Figure 5.2: Pictures of the permalloy film samples for VSM measurement.

treatment for the permalloy film of the samples as the permalloy in the channels. Pictures of permalloy samples can be seen in Figure 5.2. In some cases a problem was the bad adhesion of the permalloy to the substrate, so that only partly coverage was achieved. This made it hard to determine the exact volume of the film, and as a result the saturation magnetization could not be determined precisely.

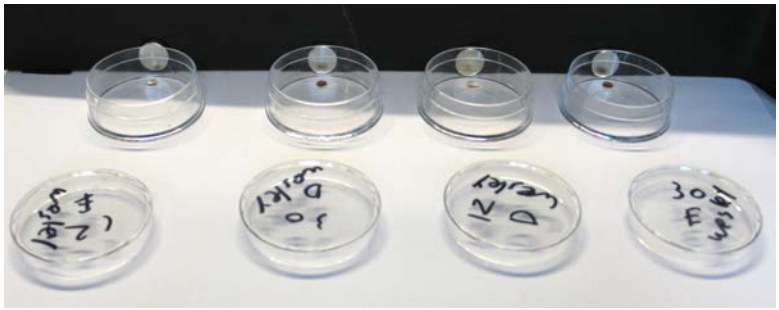

Figure 5.3: Beads drying on a glass sample.

For the preparation of the samples with magnetic beads, a microscope cover slip[3] was cut into 5x5 mm pieces. On these pieces 12 μm and 30 μm magnetic beads were dried. One set was dried without an external magnetic field. A second set was dried with an external magnetic field as shown in Figure 5.3.

5.2 Magnetic field control

For controlling the applied magnetic field a quadrupole was chosen, which is a set of four solenoids on an iron core with four pole shoes. It has a well controllable magnetic field, for the analysis of the quadrupole one is referred to Section 2.4. The four solenoids are driven in pairs of two, so that two individual electrical power amplifiers are required. First a self-built construction was used to drive the solenoids, consisting of two H-bridges and a microcontroller. Later in the project two kepcos were used as current sources, mainly because the kepcos can deliver a higher controlled current up to a higher frequency.

5.2.1 Double H-bridge

To deliver a large current for the two pairs of solenoids, first a circuit was chosen with a microcontroller and two H-bridges. The microcontroller generated the control signals, amplified by the H-bridges. To obtain a simple circuit able to deliver a large current, a class D amplifier was chosen. This is a switching amplifier, amplifying an on/off-signal with a set of inverters. The double H-bridge is able to output two voltage signals in two directions over a certain electrical load, required for the positive and negative half. Each H-bridge drives a pair of solenoids, and in this way a sinusoidal signal and a phase shifted control signal can be generated for each pair.

[3]Menzel-Gl aser, 24x40 mm #1. Thickness: 0,13 - 0,16 mm

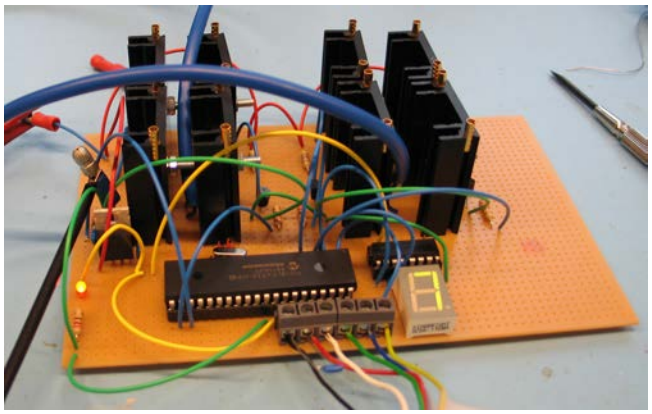

Figure 5.4: The double H-bridge circuit for driving the quadrupole current.

The circuit used for one H-bridge can be seen in Figure E.2, the two H-bridges are identical. A picture of the total circuit of the double H-bridge is shown in Figure 5.4. See for more information about the circuit and the amplification principle Appendix E.

The solenoids are modeled as an inductor with a resistor of a few ohms in series. For low frequencies the resistive part is dominant. For higher frequencies the inductive part is more dominant, and the impedance is large. With a constant sinusoidal voltage, the current will therefore drop rapidly with the frequency. The circuit is able to deliver this higher frequency signal, but not the required voltage for a solenoid current of a few ampere. As a result for higher frequencies the current drops and with this the magnetic field strength. The magnetic field dropped to half of its DC value for a frequency of about 3 Hz.

A possibility to generate a rotating magnetic field with a higher frequency, is by adding a capacitance in series. This way it can be driven with a high resonance frequency. The resonance frequency for a resistor R_L, inductor L and a capacitance C in series is

$$f_r = \frac{1}{2\,\pi}\,\frac{1}{\sqrt{L\,C}} \tag{5.1}$$

With a capacitor of 100 μF[4] a resonance frequency of 42 Hz was achieved. The disadvantage was that such a high frequency could not be set very precisely with the self-built circuit. Therefore the current was not optimal, only 0.4 A.

The H bridge could deliver a current of up to about 1.5 A per solenoid, but when a higher supply voltage was connected to the circuit, it suffered from the peak generated by the PWM signal of the solenoids. The low voltage part of the microcontroller was uncoupled electrically from the driving circuit using opto-couplers. However large peaks were generated in the output signals for supply voltages above about 13 V, disturbing the generation of the control signals.

5.2.2 Kepcos

A problem of the self-built solution was the low current, low controllability and low frequency range of the output signal. These problems were solved by using a control and amplification setup consisting of two function generators and two current amplification kepcos, a picture of which can be seen in Figure 5.5. A drawback of this solution is the large size, the produced noise and the weight, considering one kepco weighs about 30 kg.

The used kepcos were the BOP 50-8M[5] and BOP 75-6M[6]. The first has a voltage range of ± 50 V with a current of ± 8 A and the latter is able to output voltages up to ± 75 V and a current of ± 6 A. The function generators created sinusoidal signals of the same frequency, and

[4]MKP 500V capacitor VISHAY ROEDERSTEIN (MKP1848 710 454Y5)
[5]Borrowed from Thijs Bolhuis - TST group
[6]Borrowed from Marcel Schwirtz - CE group

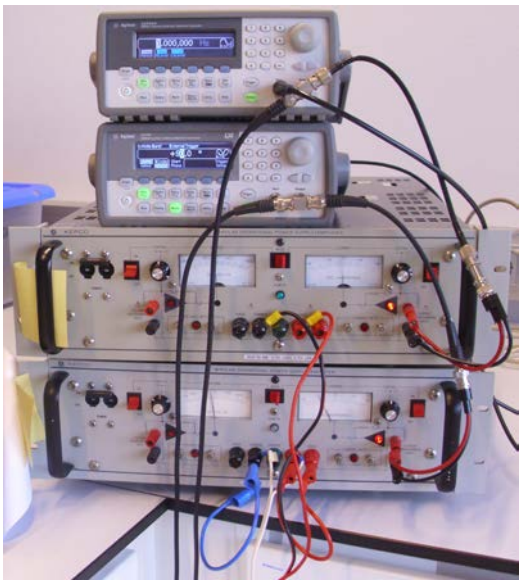

Figure 5.5: The pair function generators and kepcos for driving the quadrupole current.

the 90° phase shift was ensured by connecting the 'Sync output' of the top function generator to the 'External Trigger input' of the lower one. The function generators were connected to the current programming input of the kepcos. The two kepcos have a different current gain, so to generate the same current the control signals had different amplitudes. The output of the kepcos was connected to the two pairs of solenoids of the quadrupole. The result was a controllable solenoid current, giving a well-defined magnetic field.

The control signals for the quadrupole were verified using an oscilloscope, whereby a phase shift of 90° was required. Assumed was that the solenoids were identical, hence if the amplitude voltages of the signals were equal also the magnetic field components were equal in magnitude. The magnetic field was measured using two identical Hall-sensors[7] with the same supply voltage. With these sensors the magnetic field of the quadrupole was determined.

5.3 Setup

To study the movement of the magnetic beads and the indicator beads, the beads were loaded into the chip (see Section 5.3.2). This chip was then placed in a chip holder. The chip holder was placed on the microscope stage and the quadrupole was positioned above the holder. For a picture of the setup see Figure 5.6.

The quadrupole core consists of iron, which could potentially damage the microscope stage. Therefore the iron was covered by standard lab cleaning paper to prevent damaging the microscope stage, see Figure 5.7. The drawback was the extra distance between the pole shoes and the chip.

The quadrupole was placed on the microscope stage, above the chip and the chip holder, as shown in Figure 5.8. The distance between the pole shoes and the chip was about 0.5 cm, so that as a result the strong magnetic field between the poles is not used.

5.3.1 Indicator beads

To visualize the flow polystyrene beads were added, which were small compared to the magnetic beads. The polystyrene beads give a good indication of the flow speed and direction. Depending on their density compared to water, the indicator beads will be mostly on the top or the bottom

[7]Honeywell SS94A1 - General purpose linear magnetic hall effect Sensor

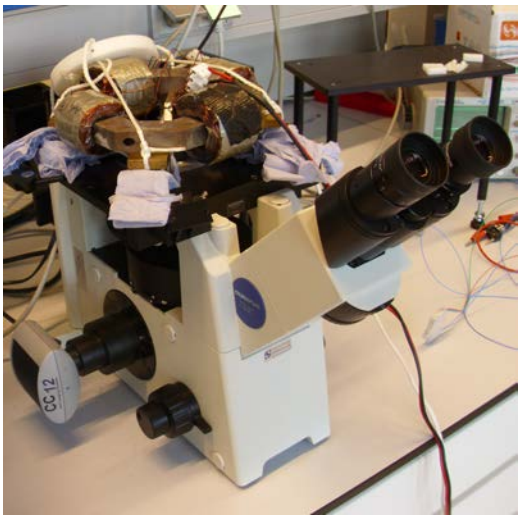

Figure 5.6: The microscope with quadrupole on top of the microscope stage.

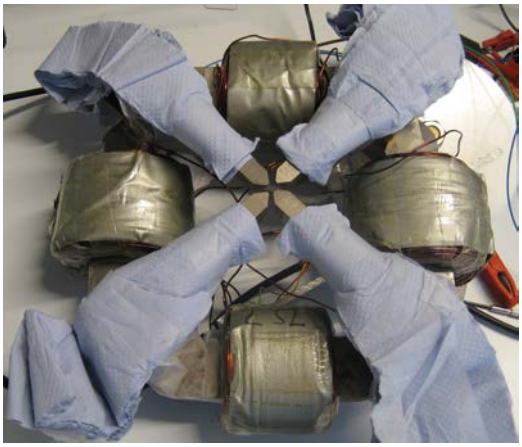

Figure 5.7: On the quadrupole cleaning paper is taped to avoid damaging the microscope stage.

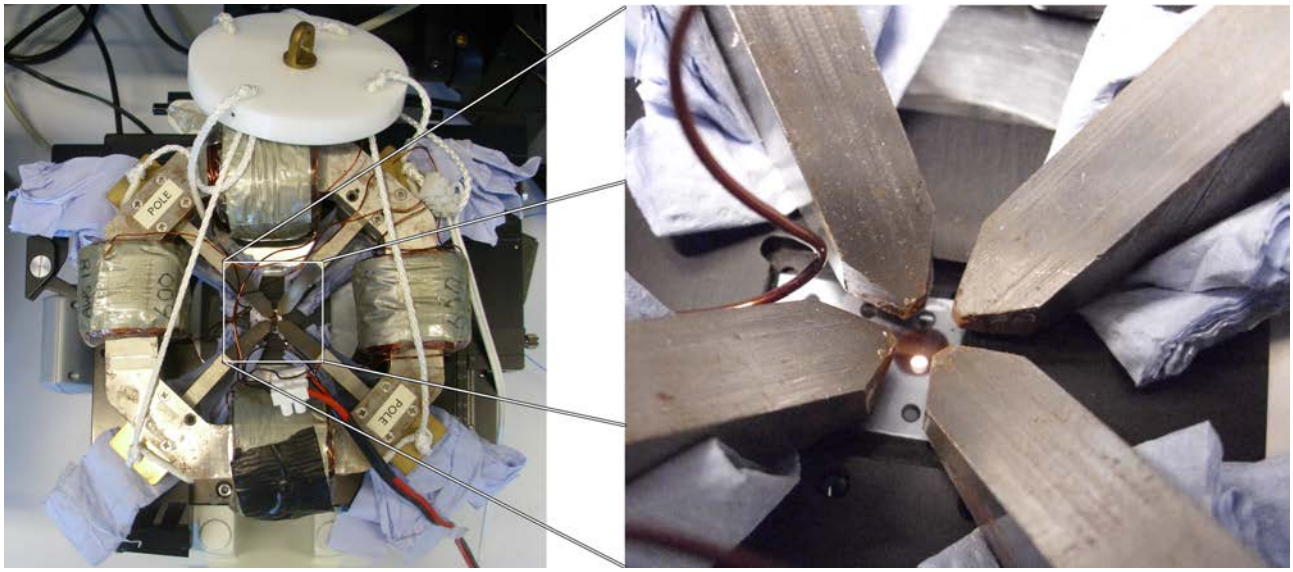

Figure 5.8: Top view of the microscope setup with quadrupole (left), and a close-up of the pole shoes of the quadrupole above the chip (right).

of the channel. The disadvantage of this is that near the top and bottom of the channel the fluid velocity is very small due to the flow boundary layer. To feel a significant force of the fluid flow, the indicator beads therefore must not be too small.

In the first set of wafers 1 μm microparticles[8] were added and in the second set red polystyrene microspheres of 3 μm[9] were added to visualize the flow.

5.3.2 Filling of the chip

The chip can be filled in two ways, by using an external pressure source or by capillary action. In the beginning of the experiment it was tried to fill the chip with a syringe pump. The syringe was connected to the chip holder by capillary connections. The idea was to stop the pump when the beads were in the right spot in the channel of the chip. This did not function well due to trapped air in the loading in- and outlets and dead volume in the system. It was difficult to apply no pressure difference over the channel. A small pressure difference can cause a flow, influencing the measuring result. Because of these problems, the filling was performed by capillary action.

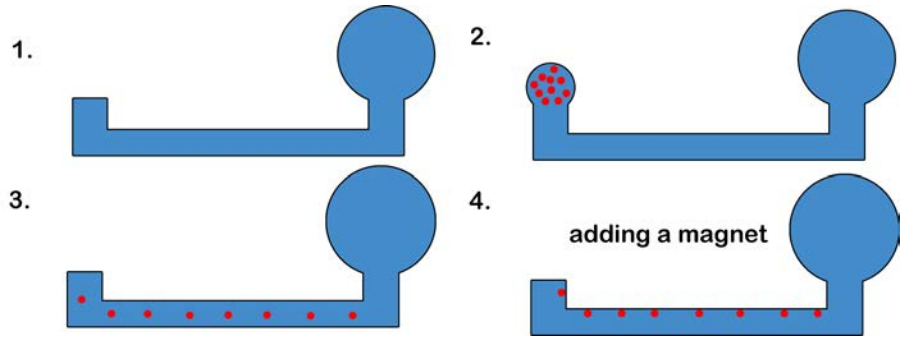

Figure 5.9: Placing the beads on the right locations.

Before using or diluting a solution with beads, the beads were shaken with the minishaker, to ensure a uniform distribution of the beads in the solution. This is required since the beads sink due to gravity. The loading of the beads in the chip was performed in a number of steps to ensure the correct positioning of beads. The protocol followed was:

- A droplet was applied to the loading inlet of the chip, and the channels fill by capillary action. This initial liquid was a channel cleaning liquid (IPA and KOH) or a solution with magnetic beads.
- The end of a syringe was inserted in the inlet, filled with a solution containing magnetic beads. The beads were mixed with Milli-Q water in a ratio of 1 : 10. By pumping or sucking with the syringe beads were placed near the permalloy disk, see step 3 in Figure 5.9. Most of the sticking beads could be released by applying a high flow with the syringe. The 30 μm magnetic beads were filtered using a 40 μm filter to remove large aggregates, see Figure 5.10 and Section 4.1.1.
- If a sufficient number of beads was placed correctly, one pair of solenoids was switched on to apply a constant magnetic field. The magnetic beads moved to a permalloy disk, see step 4 in Figure 5.9.
- The indicator beads were mixed with Milli-Q water in a ratio of 1 : 50. The concentration of both indicator beads was high. They were introduced into the chip with the syringe. The magnetic beads stayed in place due to the magnetic field, however they detached if

[8] 1 μm beads chemika 90518 microparticles with sd <= 0.1μm
[9] Polybead Polystyrene Red Dyed Microsphere 3.00μm [38]

Figure 5.10: The filter used for the filtering the 30 μm magnetic beads.

the applied flow rate was too high. The 3 μm indicator beads were mixed with a sodium chloride (NaCl) solution. The salt increased the density of the liquid, preventing the beads from sinking permanently to the bottom of the channel. For the sinking of beads as function of density see Figure 5.11. Beads which sunk to the bottom of the channel, stayed there due to the flow boundary layer.

Figure 5.11: Higher liquid density reduces the sinking of the indicator beads, the highest fluid density was in the right glass. Picture was made after 2 hours.

- To eliminate the pressure difference over the channel, a large droplet was placed over the channel in- and outlets as can be seen in Figure 5.12. The working mechanism is that the droplet has approximately the same pressure everywhere inside. This works fine until too much water is evaporated, when a pressure difference occurs again.

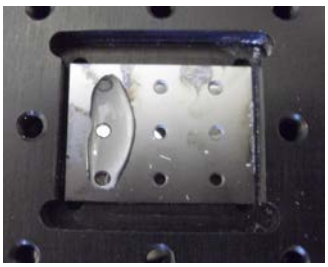

Figure 5.12: A droplet is placed over the holes to eliminate pressure differences.

- Applying a rotating magnetic field with a certain frequency, caused the magnetic beads to start rotating. Pictures and videos of the bead movement were made by using the camera[10] attached to the microscope, which can be seen in Figure 5.6.

Bead sticking problems

A problem was the sticking of the beads, with the 12 μm beads sticking in the loading in- and outlet. The explanation is the roughness near the hole due to powderblasting. Almost no

[10] CC-12, high-sensitive, soft imaging system - digital CCD color camera

sticking of the 12 μm beads occurred in the channels. Not much sticking problems with the 1 μm indicator beads were experienced.

In the second set of measurements many more problems with sticking beads were experienced, since the 30 μm magnetic beads stick to each other and to the channel walls. In some experiments the magnetic beads were rotating, but stopped suddenly and were sticking to the channel wall or to the permalloy. The 3 μm indicator beads stick to the glass and the permalloy. In a number of cases this disturbed the circular movement of the magnetic beads, however the indicator beads were required to visualize the flow. Using ink for the visualization was not practical, because of the mixing caused by the rotating beads and the low flow velocities.

An option to reduce the sticking of the beads is to apply a coating on the channel walls, for example BSA, to minimize sticking problems. Another option is to clean the chips with a mixture of KOH and IPA to ensure the wall surfaces are negative charged[11]. Experiments to investigate this were performed, however no noticeable improvement through the microscope was observed. Another option to reduce sticking problems is to make the channels smoother by apply a post-etchant in the bonded chip.

[11] Advice of Nicole Pamme, Department of Chemistry, The University of Hull.

Chapter 6

Results and discussion

With the manufactured chips experiments were performed, and the results are shown in this chapter. First the measured magnetic properties of the permalloy and the magnetic beads are discussed. Next the movement of the magnetic beads is analyzed. In the last section the resulting fluid displacement is shown, determined by using indicator beads.

6.1 Magnetic properties

In the VSM the magnetization of prepared samples was measured as shown in Section 5.1. First the results of the permalloy are shown and next the magnetization measurements on the magnetic beads.

In the manufacturing process problems were encountered with the adhesion of the permalloy film. In Figure 5.2 the partial coverage of permalloy on the samples is displayed. To make an estimation of the saturation magnetization (for permalloy 8 10^5 A/m [22]) a coverage factor is introduced. The measured dipole moment m_{vsm} is divided by the volume V_d and the coverage factor C_F to calculate the volume magnetization M.

$$M = \frac{m_{vsm}}{V_d \, C_F} \tag{6.1}$$

In this way the shape of the hysteresis curve is investigated. The coercivity H_c is not dependent on the volume, hence this is measured correctly for a partly covered sample.

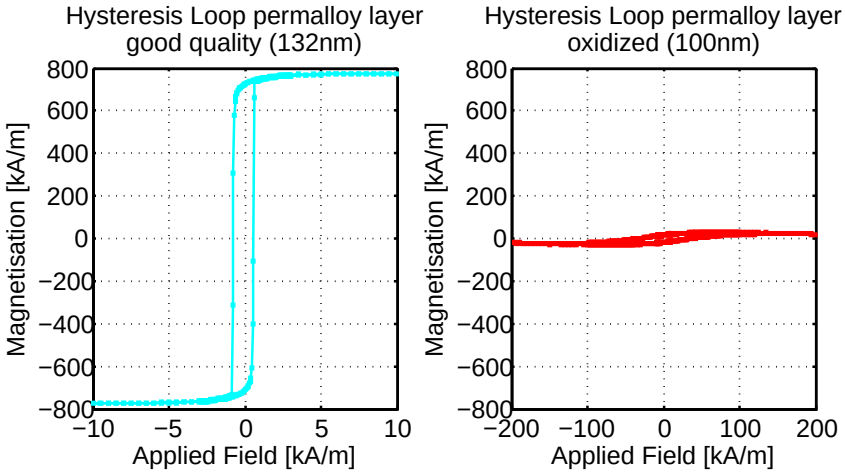

Figure 6.1: The magnetization of the good permalloy layer (Wafer 2, $C_F = 0.9$) and the fully oxidized permalloy layer (Wafer 3, $C_F = 0.9$).

In Figure 6.1 the hysteresis curves are shown of the good permalloy layer of Wafer 2 and the hysteresis curve of the oxidized permalloy layer of Wafer 3 (see for the overview of the wafer information Table C.1). The coercivity H_c of the unheated good permalloy layer is 0.7 $\frac{kA}{m}$ (Wafer 2). As an indication which field is required to almost fully saturate the material, the

applied field is determined where the magnetization was 90 % of the maximum magnetization. For the unheated permalloy layer this is 1.6 $\frac{kA}{m}$, which is very low. The oxidized layer had a very low magnetization, the with a magnetization of only 30 $\frac{kA}{m}$ instead of the 800 $\frac{kA}{m}$ of the good permalloy layer. This shows that the magnetic material can not withstand the anneal step of 600 °C required for fusion bonding.

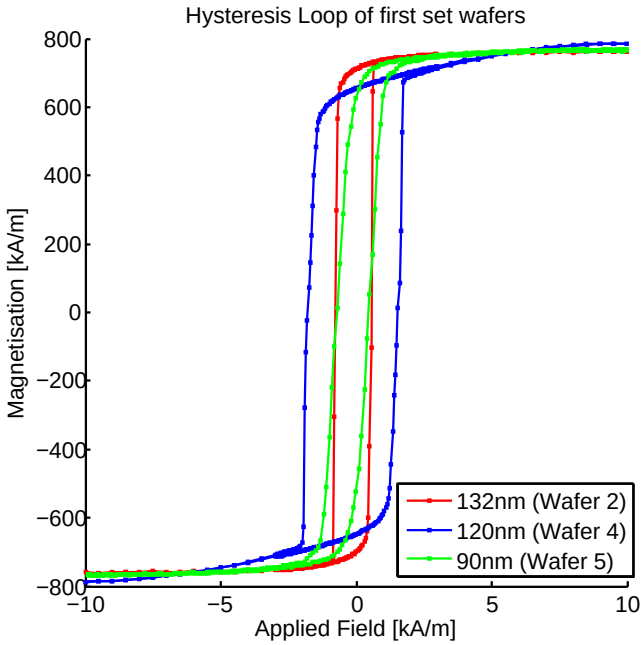

Figure 6.2: The magnetization of the permalloy of the untreated film and of the first set of wafers: Wafer 2 (132nm, $C_F = 0.9$), Wafer 4 (120nm, $C_F = 0.9$) and Wafer 5 (90nm, $C_F = 0.75$)

The magnetization of the first set of wafers was good, see Figure 6.2. The coercivity was small and the material was saturated by applying a small magnetic field.

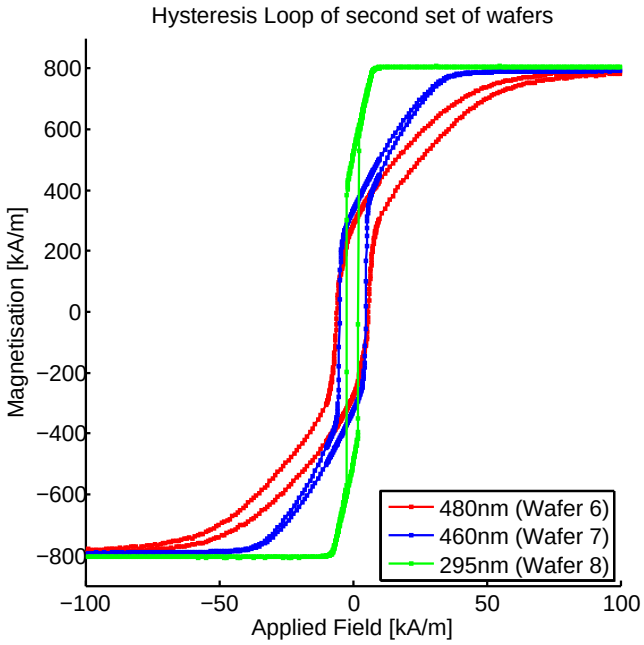

Figure 6.3: The magnetization of the permalloy of the second set: Wafer 6 (480nm, $C_F = 0.55$), Wafer 7 (460nm, $C_F = 0.13$), Wafer 8 (295nm, $C_F = 0.63$)

No.	Set	Hc	H(M=0.9Ms)	Permalloy thickness	Permalloy side
1	-	-	-	500nm	-
2	-	0.7	1.6	132nm	-
3	1	32.4	-	100nm	bottom
4	1	1.7	4.5	120nm	bottom
5	1	0.6	3.7	90nm	bottom
6	2	5.9	64	480nm	top
7	2	4.9	28	460nm	top
8	2	2.2	5.6	295nm	top

Table 6.1: Summary of the magnetic properties of the permalloy for each wafer.

The coercivity H_c of the second set of wafers was higher, but still low enough to reach a large magnetization by applying a small field. The magnetic properties were deteriorated, the hysteresis curves were not steep anymore. There was a relatively large field required to saturate the magnetic material of Wafer 6. A part of the slope in the curve is caused by the adhesion material, consisting of chromium or thallium. Chromium is an antiferromagnetic material, some magnetic interface effects could occur between the permalloy and the chromium. A summary of the coercivity and the 90 % saturation field can be found in Table 6.1.

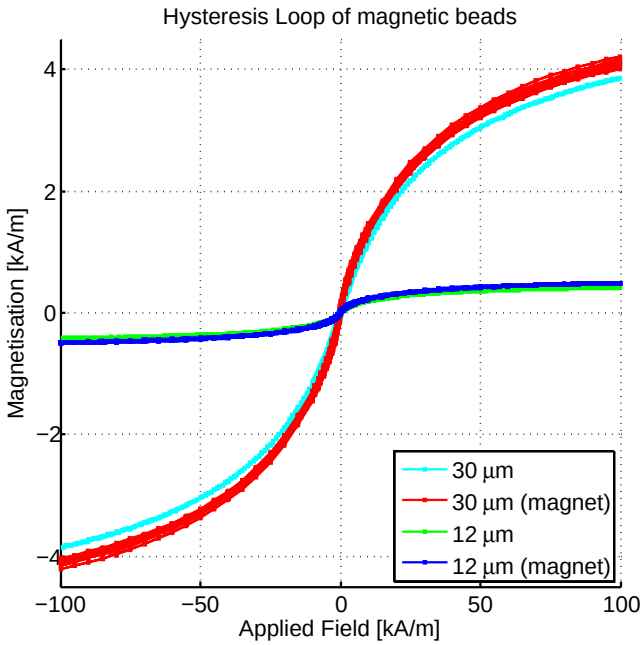

Figure 6.4: The magnetization of the magnetic beads for different angles. The beads dried with a magnet showed a higher magnetization.

Also the magnetization of magnetic beads was measured, and the hysteresis curve can be found in Figure 6.4. The magnetization of the magnetic beads was approximately as specified in the datasheet. The volume is determined by dividing the weight by the density. The magnetization of the magnetic beads dried with a magnet was a little higher, so there was little anisotropy present in the beads. This anisotropy can be a cause for the torque on the beads. The measured permanent magnetization of the beads was low, about 0.12 kA/m for the 30 μm beads and 0.03 kA/m for the 12 μm beads. The measured average susceptibility χ of the beads was low, in the order of 0.1. This is caused by the low percentage of the magnetic material in the beads.

Amplitude current	Measured magnetic field
4 A	95 $\frac{kA}{m}$
2 A	41 $\frac{kA}{m}$
1 A	20 $\frac{kA}{m}$
0.5 A	10 $\frac{kA}{m}$

Table 6.2: The measured magnetic field strength of the quadrupole magnet used for driving the beads for different currents.

The magnetic field of the quadrupole was also measured. The distance between the pole shoes and the chip was 0.5 cm. The magnetic field which was measured at this distance is shown in Table 6.2. An explanation for the non-linear relation is the coercivity of the iron. The measured magnetic field as a function of distance corresponded well with the simulated field.

6.2 Motion of beads

The beads were loaded into the channel and placed near the magnetic disks, as explained in Section 5.3.2. The small 12 μm magnetic beads were loaded and positioned without many sticking problems, hence a good array coverage was achieved. The larger 30 μm magnetic beads however experienced a lot of sticking problems, which made it hard to achieve a good array coverage. More information on the sticking problems of the magnetic beads can be found in Section 5.3.2.

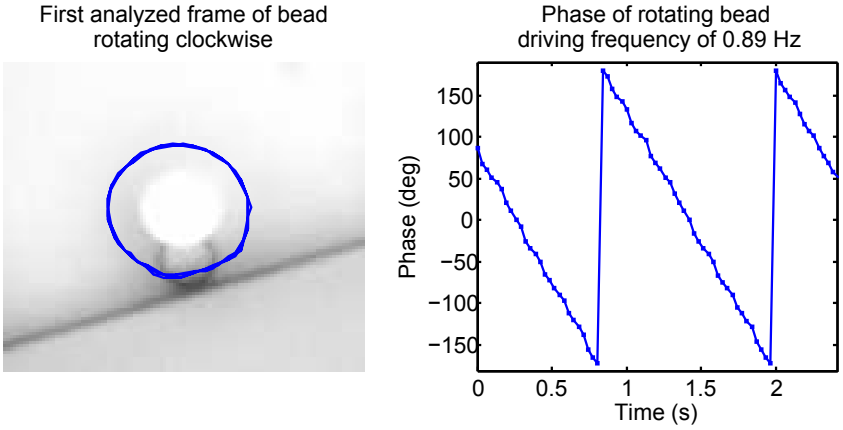

Figure 6.5: Rotating bead with a constant rotation speed (Wafer 4).

The motion of the small 12 μm beads was studied for a range of frequencies. This motion can be categorized into different regimes. The goal of the moving bead is creating a fluid flow in the channel. To achieve this a purely circulating bead movement is required, so the focus was on finding the highest actuation frequency where this is the case. A bead with a constant rotation speed is shown in Figure 6.5. There is no phase delay measured near the wall, where it could be expected, and the rotating speed is constant.

If the applied magnetic field frequency is increased, the torque on the bead becomes dominant compared to the magnetic force due to the disk. The result is that the bead makes a hypotrochoidial-like movement, as shown in Figure 6.6. The spinning part takes place at approximately the same locations. One theory to explain this is that at these spots the magnetic quality of the permalloy is less. The permalloy could be contaminated so the magnetic force is weaker. When the bead made the spinning part of the hypotrochoidial-like motion it must have been at some distance from the disk, since it was unsharp in the microscope image. This

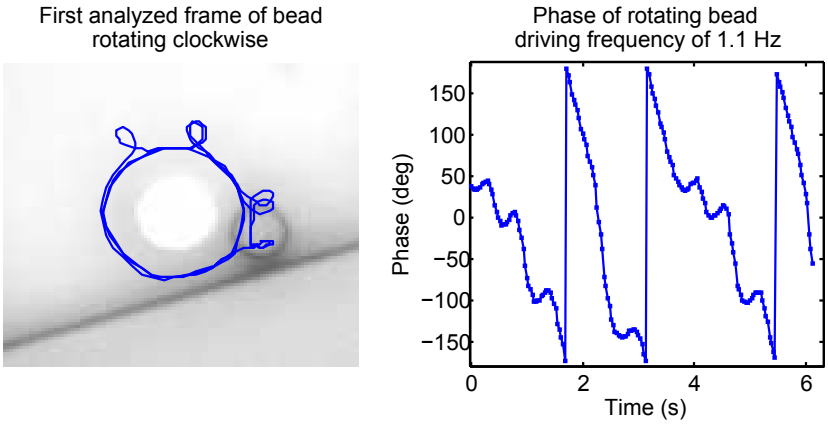

Figure 6.6: Rotating bead which makes a hypotrochoidal-like movement (Wafer 4).

behavior was an indication that the bead was on the top of the channel instead of the bottom, due to direct quadrupole force on the bead. This is not observed for the second set of wafers, since the permalloy is on the top of the channel (see Section 4.2).

When the frequency was increased further, the magnetic beads started spinning around their axis. This occurred near the permalloy disk, since there was still an attractive force between the bead and the disk. In channels with thin permalloy disks the force was so small that the beads were spinning freely through the channel. When the magnetic beads are close to each other they start forming clumps due to the mutual magnetic attraction force. To avoid the forming of a permanent magnetic superstructure the remanent magnetization of the beads must be small [16].

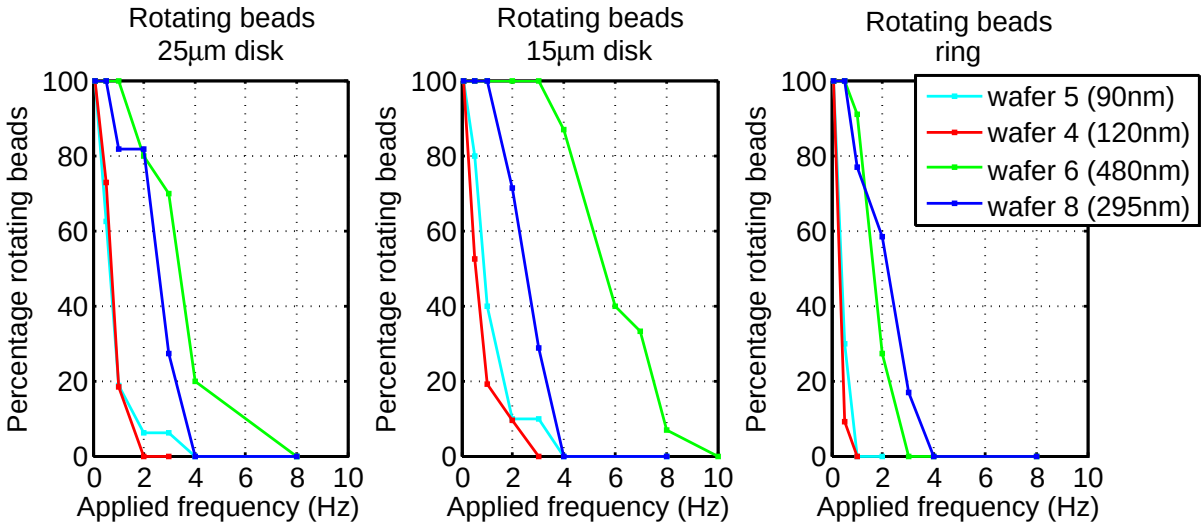

Figure 6.7: The percentage rotating magnetic beads with a quadrupole current of 4A ($N \geq 10$). The plotted percentage is the part of beads placed near a disk, which rotates at the frequency of 0.1 Hz, and still was rotating for increasing frequencies.

To measure when the beads stop with the purely circular motion, the number of circulating beads is counted visually by applying increasing actuation frequencies. The result is shown in Figure 6.7, the measurements were performed with the 12 μm magnetic beads. This counting estimates the maximum rotation frequency of the beads. The maximum rotation frequency for the first set of wafers was low, the most beads stopped spinning below 1 Hz. For the second set of wafers much higher rotating frequencies were achieved, caused by the larger disk volume.

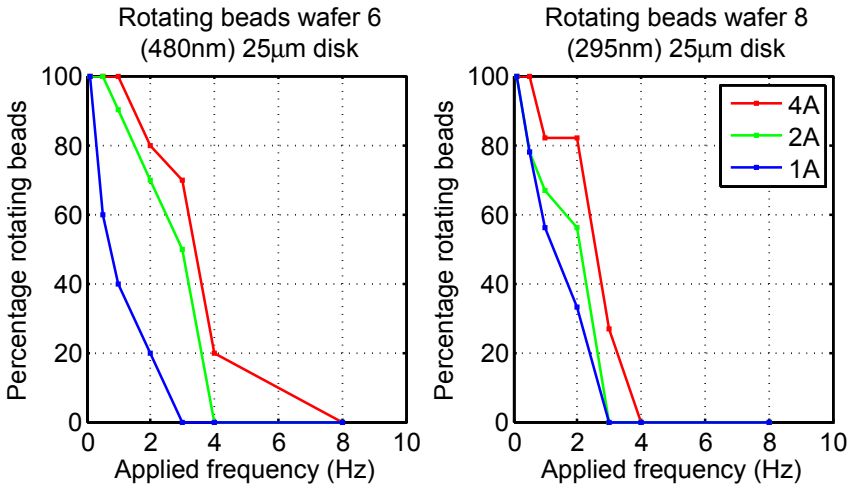

Figure 6.8: The percentage rotating magnetic beads around a 25 μm permalloy disk ($N \geq 8$). The plotted percentage is the part of beads placed near a disk, which rotates at the frequency of 0.1 Hz, and still was rotating for increasing frequencies.

The same measurement was performed for different solenoid currents, the result is shown in Figure 6.8. The maximum rotation frequency for Wafer 6 was higher than that of Wafer 8, however the percentage rotating beads of Wafer 6 decreases faster with the solenoid current than Wafer 8 . This results from the higher required magnetic field to saturate the permalloy of Wafer 6 compared to Wafer 8 (see Figure 6.3). From this it is clear that not only the coercivity field H_c is an important material parameter, but also the required field strength to saturate the material. Both must be as low as possible to still achieve a high maximum rotation frequency with a small magnetic field. The same holds for the magnetization of the magnetic beads.

On the rotating behavior of the 30 μm beads less analyses are performed, due to the small percentage of rotating beads. The maximum rotation frequency of the 30 μm beads was approximately 6 Hz.

6.3 Fluid displacement

To visualize the flow caused by the beads rotating around the disks, non-magnetic indicator beads are added. Assumed is that the beads are small enough to not influence the fluid flow. The video recordings made with the microscope camera are analyzed using a particle tracking script. The fluid displacement in the experiments performed with the 12 μm beads is not shown, because the liquid flow was too low to do a meaningful particle analysis. The results of the experiments performed with the 30 μm beads are more useful, since a frequency of 5 Hz could be achieved in the solution with indicator beads. The velocity of the magnetic bead is the circumference of the disk multiplied by the rotation frequency. The presented results are performed using 25 μm disks. Therefore the bead velocity is

$$u_b = 2\ \pi\ R_d\ f_m = \pi\ 25\ \mu m\ 5\ Hz = 393\ \frac{\mu m}{s} \tag{6.2}$$

According to Section 3.2 the average fluid velocity is expected to be 1 % of the velocity of the bead in one direction. The pumping efficiency is theoretically about 20 %, so the average channel velocity caused by a circulating bead would then be about 0.2 %. According to theory discussed in Chapter 3 the average channel velocity therefore is about 0.8 $\mu m/s$.

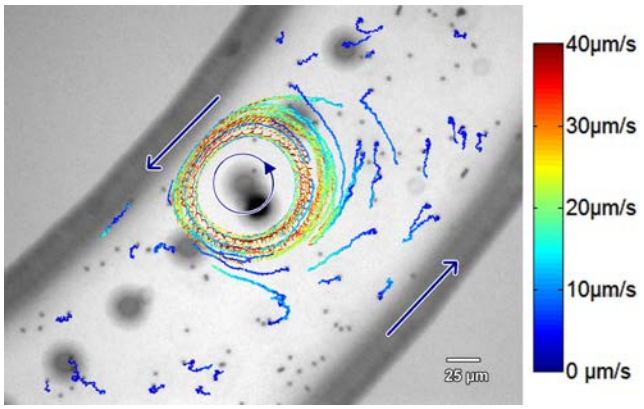

Figure 6.9: The observed motion of the indicator beads caused by one rotating magnetic bead at a magnetic field frequency of 5 Hz, indicating a net liquid flow in the channels.

In MATLAB a particle tracking script was written[1], see Appendix F. The result of the analysis on the video of one rotating bead is shown in Figure 6.9. The maximum velocity of 40 $\mu m/s$, found for some indicator beads near the rotating magnetic beads, is limited by the particle tracking algorithm and the frame rate of the microscope camera. There is some net displacement of fluid, but the asymmetry is very small.

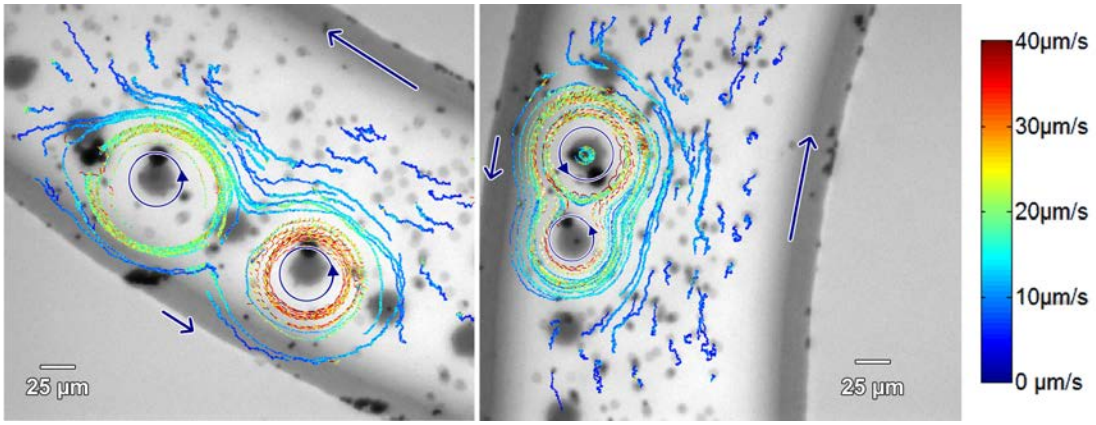

Figure 6.10: The observed motion of the indicator beads caused by two rotating magnetic beads at a magnetic field frequency of 5 Hz, indicating a net liquid flow in the channels.

A better result is obtained with two rotating magnetic beads. In Figure 6.10 the analysis of two beads can be seen, on the left two spaced beads and on the right two beads directly next to each other. The net fluid was much larger, the pumping effect was increased. A part of the non-magnetic indicator beads followed this pumping motion.

[1]For the particle location and tracking an existing script was used [10].

There was a net flow in the middle of the channel with an average velocity of 9 $\mu m/s$. This net flow was observed in about one sixth of the channel width. Based on this the average channel velocity would be 1.5 $\mu m/s$, however this velocity is only based on the moving indicator beads. If a pipe flow with parabolic velocity profile (pressure driven flow) is assumed for the part where the net flow takes place, the average flow is half the maximum flow. So if is assumed that the indicator beads are following the maximum flow, the average channel velocity is the half of their velocity: about 0.75 $\mu m/s$. This is close to the theoretical value of 0.8 $\mu m/s$.

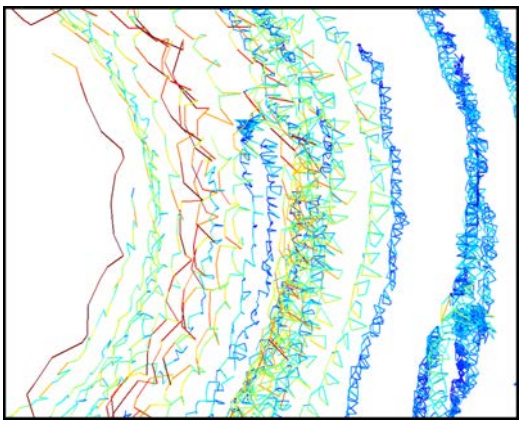

Figure 6.11: The zoomed image of the observed motion of the indicator beads caused by two rotating magnetic bead next to each other, fully showed in Figure 6.10 on left.

The rotating beads performed a pushing and pulling effect on the fluid, this is seen on the motion of the indicator beads in Figure 6.11. The non-magnetic indicator beads performed a hypotrochoidial-like pumping movement. The indicator bead analysis shows some similarity with the simulation result of Figure 3.13. Close to the magnetic beads the highest fluid velocities are achieved. In the middle of the channel, the largest net fluid flow is generated. Close to the opposite wall almost no flow is detected, similar to the flow in the simulation result.

Chapter 7

Conclusion and recommendations

7.1 Conclusion

The purpose of the assignment was to investigate whether it would be possible to pump liquid in a microchannel, using rotating magnetic beads around an array of magnetic disks. The experiments showed that it is possible to create a net flow using an array of permalloy disks. The smaller beads with a diameter of 12 μm showed good array coverage and little sticking problems, but only low rotation frequencies could be achieved. This is due to a low saturation magnetization of the beads. With the larger beads of 30 μm a much higher range of rotation frequencies could be reached, however only partial coverage of the disk array could be obtained due to sticking problems. With a rotation frequency of 5 Hz of the larger magnetic beads a net flow of 9 $\mu m/s$ in the middle of the channel was measured, by following indicator beads. This gives an average channel velocity of approximately 0.75 $\mu m/s$, which fits well with theory. The expectation is that further optimization of the geometry and magnetic bead coverage will lead to a significant increase in flow rate.

Permalloy proved to be a difficult material to handle, the magnetic coercivity is very sensitive to heating steps. The adhesion of the permalloy film to silicon and glass was poor, even when an adhesion layer was applied. Nevertheless it was possible to saturate most of the fabricated magnetic disk arrays by using a relatively small magnetic field of 95 kA/m.

The pumping efficiency is strongly dependent on the distance between the rotating bead and the wall. The highest efficiency could be achieved by minimizing the gap between the rotating bead and the wall. The highest pumping rate is obtained at the maximum rotation frequency, where the movement was still purely circular and not hypotrochoidal-like. Larger beads not only experience more force in the magnetic field generated by the disks, but they also displace more liquid per cycle.

The maximum achievable rotation frequency depents on the magnetic force between the disk and the magnetic beads. To maximize this force, the permalloy disk must be as thick as possible and the magnetization of the disk and the bead must be as high as possible. To achieve a constant rotational movement the beads must be as 'superparamagnetic' as possible.

7.2 Contribution

The principle of the pumping investigated in this work is new and may give rise to a novel microfluidic pumping platform. It has been shown that the pumping principle works, it is possible to create a net flow by rotating magnetic beads around permalloy disks. Earlier studies showed the possibility of pumping, using trapped beads rotating around their axis by optical means. The disadvantage of the complex trapping system used there has been solved by using magnetic disks in the channel. Possible manufacturing methods as well as the magnetic properties of the system are investigated, giving good insight into the operating principle. The abstract of this thesis has been submitted to the MicroTas 2012 conference in Japan, and possibly the results will be presented there too.

7.3 Outlook

The used quadrupole is large and its magnetic field is not used efficiently, the strong magnetic field between the poles could not be fully used since the chip was too large. For further experiments it would be practical to design and build a magnetic quadrupole generating a magnetic field which could be used more efficiently. In this new design the structure of an existing magnetic stirrer actuator for stir bars could be investigated. For better array coverage the beads have to be loaded uniformly into the pumping channel. This could be achieved by placing a spiral channel before the pumping channel, distributing the beads more uniformly using Dean force [6]. Also an improved permalloy array design is required, since the larger beads need more separation distance.

A disadvantage of the quadrupole setup used in this study, is that the generated field can not be applied locally to specific parts of the chip, but instead is present everywhere. An idea is to make the rotating field more local by applying magnetic material on the chip such that only a rotating magnetic field is generated where the local pumping is required. A possible way to generate a more local magnetic field, is by a quadrupole design with very small pole shoes. This would enable the possibility to pump liquid by selecting certain parts of the arrays, giving a controlled programmable way of pumping. This is useful for various biological microfluidic applications. It is also possible to generate magnetic fields using small coils on chip [40]. A useful follow up study would be to investigate how locally the actuating rotating magnetic fields could be generated and controlled on chip.

To improve the magnetization of the magnetic array patterns, the actual magnetization in the disk material can be studied. A possibility is to use magnetooptical microscopy which could be performed in Dresden [27]. The shape of the magnetic array components can be optimized, by investigating the internal magnetization of the disks compared to the ring.

When only pumping into one direction is required, it is possible to bring an asymmetry into the channel walls. One way is to fabricate a sawtooth shape in the channel wall, such that the pumping efficiency is increased. An interesting extra functionality of the microfluidic pumping system as presented here, would be the ability to select individual channels. If magnetic beads could also be used as valves, the programmable selection of channels would be possible. Locally a very concentrated magnetic field could be created to accumulate beads, such that the channel is closed. With this functionality added, all required unit functions for a basic microfluidic platform would be available: pumping, valving and mixing.

7.4 Recommendations

The net flow created by the beads has to be optimized and the sticking problems have to be reduced in order to get a reasonable flow. Therefore magnetic beads with a higher saturation magnetization and less sticking are required. The used magnetic beads mainly consist of a non-magnetic matrix. A larger magnetic force could be achieved by using a bead which consists of a magnetic core with a large saturation magnetization without a significant remanent magnetization. Proper coating could make such a bead biocompatible and prevent sticking.

The magnetic array has to be redesigned such that the distance between the disks is optimal for the chosen beads. The maximum rotation frequency is increased by exerting more force on the beads compared to the torque, which could be achieved by changing the geometry. Therefore a larger disk volume in combination with a large saturation magnetization is required. This could be realized by using permalloy pillars instead of disks. The magnetic quadrupole setup could be made smaller and the generated magnetic field could be used more efficiently. This will also demonstrate that the complete setup could be reduced to a table top system.

It is expected that the most improvement in rotation frequency could be achieved by using beads with better magnetic properties. Therefore the properties of the magnetic bead should be optimized first, and next extra functionalities could be added.

Bibliography

[1] Belgian bioelectromagnetic group (bbemg) - dictionary. http://www.bbemg.ulg.ac.be/UK/00/dictionary.html.

[2] Hysteresis parameters. http://magician.ucsd.edu/essentials/WebBookse50.htmlx60-9200111.

[3] Laminar flow. http://www.youtube.com/watch?v=p08_KlTKP50.

[4] R. Arayanarakool, S. Le Gac, and A. van den Berg. Low-temperature, simple and fast integration technique of microfluidic chips by using a uv-curable adhesive. *Lab Chip*, 10(16):2115–2121, 2010.

[5] ARTIC project. Low reynolds number flows. http://www.hitech-projects.com/euprojects/artic/index/Low%20Reynolds%20number%20flows.pdf.

[6] A. Bhagat, S. Kuntaegowdanahalli, and I. Papautsky. Continuous particle separation in spiral microchannels using dean flows and differential migration. *Lab Chip*, 8(11):1906–1914, 2008.

[7] T. Boyer et al. The force on a magnetic dipole. *Am. J. Phys*, 56(8):8, 1988.

[8] C. Coquaz, D. Challeton, J. Porteseil, and Y. Souche. Memory effects and nucleation of domain structures in small permalloy shapes. *Journal of magnetism and magnetic materials*, 124(1-2):206–212, 1993.

[9] B. Cullity and C. Graham. *Introduction to magnetic materials*. Wiley-IEEE Press, 2008.

[10] E. D. Daniel Blair. The matlab particle tracking code repository. http://physics.georgetown.edu/matlab/index.html.

[11] DoITPoMS. Types of magnetism. http://www.doitpoms.ac.uk/tlplib/ferromagnetic/types.php.

[12] C. C. Doppen. The designing and building of a kerr micrsocope. Master's thesis, University of Twente, 2003.

[13] J. Eijkel. Lab on a chip course 2010 microfluidics: principles and components, April 2010.

[14] D. L. Feucht. Magnetic-electric analogs. http://www.analogzone.com/col_0909.pdf.

[15] R. Feynman, R. Leighton, M. Sands, et al. *The Feynman lectures on physics*, volume 2. Addison-Wesley Reading, MA, 1964.

[16] M. Gijs. Magnetic bead handling on-chip: new opportunities for analytical applications. *Microfluidics and Nanofluidics*, 1(1):22–40, 2004.

[17] R. Goldfarb and F. Fickett. *Units for Magnetic Properties*. US Dept. of Commerce, National Bureau of Standards, 1985.

[18] A. Goldman, R. Cox, and H. Brenner. Slow viscous motion of a sphere parallel to a plane wall–i motion through a quiescent fluid. *Chemical Engineering Science*, 22(4):637–651, 1967.

[19] D. Griffiths and R. College. *Introduction to electrodynamics*, volume 3. prentice Hall New Jersey:, 1999.

[20] K. Gunnarsson, P. Roy, S. Felton, J. Pihl, P. Svedlindh, S. Berner, H. Lidbaum, and S. Oscarsson. Programmable motion and separation of single magnetic particles on patterned magnetic surfaces. *Advanced Materials*, 17(14):1730–1734, 2005.

[21] U. Häfeli, R. Ciocan, and J. Dailey. Characterization of magnetic particles and microspheres and their magnetophoretic mobility using a digital microscopy method. *European Cells and Materials*, 3(2):24–27, 2002.

[22] R. HERTEL. Thickness dependence of magnetization structures in thin permalloy rectangles. *Zeitschrift für Metallkunde*, 93(10):957–962, 2002.

[23] P. Hung, P. Lee, P. Sabounchi, R. Lin, and L. Lee. Continuous perfusion microfluidic cell culture array for high-throughput cell-based assays. *Biotechnology and bioengineering*, 89(1):1–8, 2005.

[24] X. Janssen, A. Schellekens, K. Van Ommering, L. Van Ijzendoorn, and M. Prins. Controlled torque on superparamagnetic beads for functional biosensors. *Biosensors and Bioelectronics*, 24(7):1937–1941, 2009.

[25] P. K. Kundu. *Fluid mechanics / Pijush K. Kundu*. Academic Press, San Diego :, 1990.

[26] J. Leach, H. Mushfique, R. di Leonardo, M. Padgett, and J. Cooper. An optically driven pump for microfluidics. *Lab Chip*, 6(6):735–739, 2006.

[27] Leibniz Institute for Solid State and Materials Research Dresden. Magneto-optical kerr effect microscopy. `http://www.ifw-dresden.de/institutes/imw/sections/24/kerr-microscopy`.

[28] J. Lodder. *Materiaalkunde*, volume deel B. Universiteit Twente, faculteit der elektrotechniek, augustus 2000.

[29] Magnasence. Superparamagnetic nanospheres. `http://magnasense.com/index.php?page=superparamagnetic-nanospheres`.

[30] D. Mark, S. Haeberle, G. Roth, F. Von Stetten, and R. Zengerle. Microfluidic lab-on-a-chip platforms: requirements, characteristics and applications. *Chem. Soc. Rev.*, 39(3):1153–1182, 2010.

[31] MEMS and N. Exchange. Anodic bonding: Page 1 of 1. `https://www.mems-exchange.org/catalog/anodic_bonding/`.

[32] I. Meyvantsson and D. Beebe. Cell culture models in microfluidic systems. *Annu. Rev. Anal. Chem.*, 1:423–449, 2008.

[33] micromod Partikeltechnologie GmbH. Technical data sheet. `http://www.micromod.de/_docs/1334496538.pdf`, december 2010.

[34] micromod Partikeltechnologie GmbH. Technical data sheet. `http://www.micromod.de/_docs/1334497194.pdf`, december 2010.

[35] MicroSense. Vector magnetometer model 10 vsm. `http://www.microsense.net/products-vsm-model-10.htm`.

[36] B. M. Moskowitz. Hitchhiker's guide to magnetism.

[37] M. Okochi, H. Tsuchiya, F. Kumazawa, M. Shikida, and H. Honda. Droplet-based gene expression analysis using a device with magnetic force-based-droplet-handling system. *Journal of bioscience and bioengineering*, 109(2):193–197, 2010.

[38] I. Polyscience. Polybead polystyrene red dyed microsphere 3.00m. `http://www.polysciences.com/Core/Display.aspx?pageId=98&categoryId=346&productId=827`, 2011.

[39] E. Purcell. Life at low reynolds number. *Am. J. Phys*, 45(1):3–11, 1977.

[40] A. Rida, V. Fernandez, and M. Gijs. Long-range transport of magnetic microbeads using simple planar coils placed in a uniform magnetostatic field. *Applied physics letters*, 83(12):2396–2398, 2003.

[41] S. Shevkoplyas, A. Siegel, R. Westervelt, M. Prentiss, and G. Whitesides. The force acting on a superparamagnetic bead due to an applied magnetic field. *Lab Chip*, 7(10):1294–1302, 2007.

[42] TheFreeDictionary.com. ampere. `http://www.thefreedictionary.com/ampere`.

[43] E. W. Weisstein. Hypotrochoid. `http://mathworld.wolfram.com/Hypotrochoid.html`.

[44] E. W. Weisstein. Mks. `http://scienceworld.wolfram.com/physics/MKS.html`, 2007.

[45] WolfgangS. Pulsweitenmodulation zur erzeugung einer sinusfrmigen spannung. `http://nl.wikipedia.org/wiki/Bestand:Pulsweitenmodulation.png`, april 2006.

Appendix A

Supplementary theory

A.1 The H-field

To calculate fields in materials the magnetic field H is used, however there exist different definitions. These definitions and their conversion factors are discussed in this section.

A.1.1 Definition

There exist different definitions for the relation between these fields, which makes comparing literature quite confusing. In principle there are three definitions with different systems of units:

- The SI, adopted by the National Bureau of Standards, based on the mks unit system, is commonly used by engineering and beginning physics. This system is based on the following definition of the H-field: $\vec{H} = \vec{B}/\mu_0 - \vec{M}$. The unit of $\vec{B}$ is tesla (T) or weber per meter (Wb/m^2), the unit of $\vec{M}$ is ampere per meter (A/m) and corresponding to the definition $\vec{H}$ also has the unit of ampere per meter (A/m). The book of Griffiths uses this definition. [19, Page 269]
- The cgs system is mostly used in theoretical physics. The defining relation here is $H = B - 4\pi M$. The unit of $\vec{B}$ is gauss (G) and the unit of $\vec{H}$ is oersted (Oe) which have the same size. The magnetization $\vec{M}$ has the unit of emu per cubic cm (emu/cm^3).
- Feynman uses his own definition of the magnetic field: $\vec{H} = \vec{B} - \vec{M}\frac{1}{\epsilon c^2}$. In his definition $\vec{H}$ and $\vec{B}$ both have the unit weber per square meter (Wb/m^2) and $\vec{M}$ has the unit ampere per meter (A/m). This is the definition which is not recognized under SI and is based on the definition $B = \mu_0 H + J$, where J is the magnetic polarization or intensity of magnetization. [15, Page 36-5] [17, 44]

The first definition is approved by the SI, therefore this definition is used in this report.

A.1.2 Conversion factors

Quantity	Symbol	Gaussian and cgs emu	Conversion factor	SI
Magnetic induction	B	gauss (G)	10^{-4}	T, Wb/m^2
Magnetic field strength	H	oersted (Oe)	$10^3/4\pi$	A/m
Volume magnetization	M	emu/cm^3	10^3	A/m
Mass magnetization	M	emu/g	1	$A \cdot m^2/kg$
Magnetic moment	m	emu	10^{-3}	$A \cdot m^2$

Table A.1: Units for magnetic properties [17].

A.1.3 Magnetic induction

In the report only static analyses are preformed, but to derive the law for induction the time depended Maxwell equation for the electric field is required. The Maxwell-Faraday equation for the electric field associated with a changing magnetic field is

$$\vec{\nabla} \times \vec{E} = -\frac{\partial \vec{B}}{\partial t} \tag{A.1}$$

This equation can be written in integral form using Stokes' theorem

$$\oint_{\Gamma} \vec{E} \cdot \mathrm{d}\vec{l} = -\frac{\partial}{\partial t} \int_{S} \vec{B} \cdot \vec{n} \mathrm{d}a \tag{A.2}$$

Here is Γ any closed curve and S is any surface bounded by it, both fixed in space. The expression at the left-hand side is equal to so called inducted electromotive force, or short emf ϵ in volts. The right-hand side is equal to the rate of change of the magnetic flux Φ_B. [15, p 17-2]

$$\oint_{\Gamma} \vec{E} \cdot \mathrm{d}\vec{l} = \oint_{\Gamma} \frac{\vec{F}_e}{q} \cdot \mathrm{d}\vec{l} = EMF = -\frac{\partial \Phi_B}{\partial t} \tag{A.3}$$

The electric field is equal to the force per charge, therefore is the name of the result of this integral called EMF. On this principle the dynamo is based, there is a voltage generated caused by a changing magnetic field. But it works also the other way around, a changing magnetic field generates a force. The flux-rule shown in Eq. A.3 applies whether the flux changes because the field changes or because the circuit moves or a combination of both. To determine the direction of the force, the right-hand rule is used, which is a simple way to evaluate a cross product. Another option is to calculate the force with the Lorentz force law

$$\vec{F} = q\left(\vec{E} + \vec{v} \times \vec{B}\right) \tag{A.4}$$

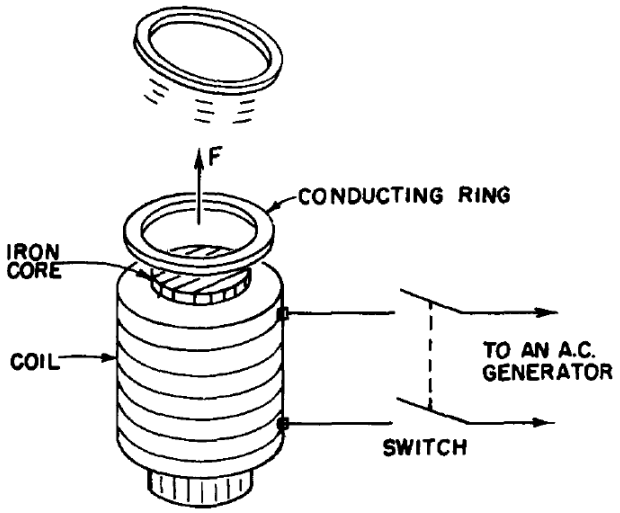

Figure A.1: An example of Lenz's rule, the generated force is opposite to the applied field. [15]

This changing magnetic field can be applied to a closed conducting ring as shown in Figure A.1. The behavior can be explained by Lenz law, see the minus sign in Eq. A.3. This law states that whenever a change in magnetic field occurs, an electric field (an extra current) is generated to oppose the change [15, p 34-2].

A.2 Types of magnetic effects

The magnetic behavior of a material depends on the structure of the electron shells. Most nonmetals are diamagnetic, because they have a closed electron shell. It is more complicated for metals, it depends on the magnetic coupling between the atoms. Next the most important magnetic effects will be discussed.

Diamagnetism

Diamagnetic materials are repulsed from a magnetic field, it will a force to the place where the magnetic field is weaker. In the setup shown in Figure A.2 it is repelled by the sharp pole. In most materials this is a weak force, but in certain materials like superconductors this is a strong force. Diamagnetism can be explained with Lenz law, which states that whenever a change in magnetic field occurs, an electric field (an extra current) is generated to oppose the change (see Eq. A.3). There is no permanent magnetic moment present in absence of an external magnetic field, all moments caused by electron spins and orbital motions balance out. When an external magnetic field is applied, extra little currents are generated inside the atom caused by induction, see Section A.1.3. This external magnetic field changes the motion of electrons in the atom. The material gets magnetized $\vec{M}$ in such a direction as to oppose the increasing magnetic field. This effect is more or less temperature independent. The magnetic susceptibility is generally quite small, in the order of $\chi = \mu_r - 1 \approx -10^{-5}$. Superconductors may be seen as ideal diamagnets with a magnetic susceptibility of -1, they mirror the applied magnetic field perfectly (below their critical temperature T_c). Ordinary diamagnetism is a general property of matter, it is always present. In order to observe diamagnetism, para- and ferromagnetism must be absent, else the diamagnetic effect will be masked by the other more dominant effect. Examples of substances where this can be observed are noble gases, and most organic compounds. [9, 15]

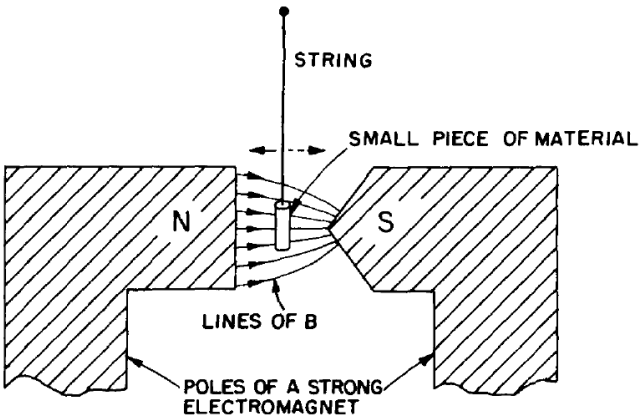

Figure A.2: Diamagnetic materials is weakly repelled by the sharp pole, paramagnetic materials are weaker attracted by the sharp pole and ferromagnetic materials are strongly attracted. [15]

Paramagnetism

Besides the diamagnetic effect, which is always present, there is also the possibility of lining up the individual atomic magnetic moments (see for magnetic moment Section 2.3.3). The induced magnetization tends to enhance the magnetic field, when it is larger than the diamagnetic effect. The substances where this occurs are called paramagnetic. In this case the material is attracted to the external magnetic field, in the setup of Figure A.2 it is attracted to the sharp pole. The magnetic susceptilities are in the order of $\chi = \mu_r - 1 \approx 10^{-5}$. This effect is fairly weak, the lining-up forces are relatively small compared to the forces from the thermal motion which try to derange the order. The magnetic susceptibility scales normally with one

over the temperature $1/T$. So the lower the temperature, the stronger the effect becomes. An exception is paramagnetism arising from the spins of electrons responsible for the conduction in metals, the susceptibility χ can decrease, remain constant or even increase with temperature. It depends on the metal which effect is observed.

Ferromagnetism

In the case of ferromagnetism (almost) all the atomic moments line up. This is due to strong short distance exchange interaction, this causes that the spins tend to align in the same direction. The direct magnetic interaction wants to align the moments such that the net moment is zero. The interaction force is about ten thousand times stronger than the direct magnetic interaction, therefore the moments in ferromagnetic materials line up. This can only be explained by quantum mechanics, which will not be discussed. This effect is temperature depended, above the material dependent Curie temperature it will behave paramagnetic. Three metals are ferromagnetic at room temperature: iron (Fe), cobalt (Co) and nickel (Ni). Chromium (Cr) is antiferromagnetic, see also Figure 2.2. Antiferromagnetic materials have a similar force, but the exchange interaction between neighboring atoms leads to a anti-parallel alignment of the magnetic moments. The net susceptibility of an antiferromagnetic material is in the same order as paramagnetic material $\chi = \mu_r - 1 \approx 10^{-5}$. The susceptibility of a ferromagnetic material is very large, for iron typically several thousand. There are special alloys like *supermalloy* which can have permeabilities as high as a million. This susceptibility is more or less linear up till the saturation magnetization, see Section 2.2.3. Certain ferromagnetic materials are able to retain a large magnetization when the external magnetic field is removed. [15]

Superparamagnetism

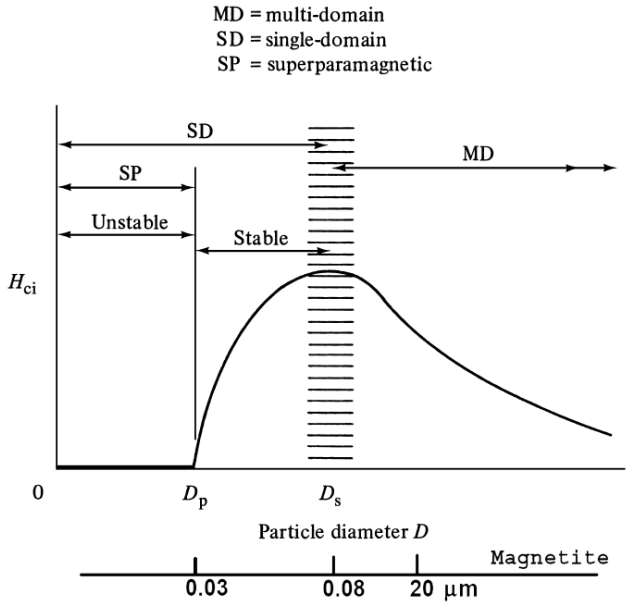

Figure A.3: When the particle diameter is very small, the magnetite Fe_3O_4 particle is behaving superparamagnetic. [9, 36]

If a particle is made small than a certain diameter D_s it will consist of only one magnetic domain, single domain SD, see Section 2.2.2 for a discussion about magnetic domains. This magnetic domain is still able to retain a magnetization without an external field. When it becomes even smaller than a certain diameter D_p, than this remanent magnetization will disappear. The particle becomes superparamagnetic. The volume of the particle is small enough that the thermal energy is sufficient to overcome the energy of the magnetization states. The

thermal energy can cause a spontaneous reversal of magnetization, this is a statistical process. In an applied field there will be a net statistical alignment of magnetic moments. This is analogous to paramagnetism, except now the magnetic moment is not that of a single atom, but to an single domain *SD* particle containing 10^5 atoms. Hence the term superparamagnetism, which denotes a much higher susceptibility than paramagnetism. In response to a change in the applied field or temperature, an ensemble of superparamagnetic *SPM* particles will approach an equilibrium value of magnetization with a characteristic relaxation time known is the Néel relaxation time. This assumes a certain anisotropy in the particle, this means that there exist an easy axis where there is less energy needed to magnetize the particle. Therefore will this easy axis be oriented parallel to the applied field. For the Néel relaxation time holds

$$\frac{1}{t_r} = f_0 \mathrm{e}^{\frac{-K_u V}{k_b T}} \tag{A.5}$$

where t_r is the relaxation time, f_0 is a constant frequency factor ($10^9 Hz$), K_u is anisotropy constant, V is the particle volume, k_b is the Boltzmann constant and T is the absolute temperature. If the superparamagnetic particles are randomly distributed through a non-magnetic matrix, there will be no net anisotropy, although there is a time needed for the particle to reach a equilibrium. So when the external magnetic field is switched off, the magnetic moment will disappear with the Néel relaxation time. Ideally this time will be very short for one particle (in the nanosecond range), however it is possible that there is an interaction between particles which causes a longer relaxation time [36].

A.3 Magnetic charge

To evaluate this equation an example of a bar magnetic is chosen. Suppose a long bar magnet with a surface A_p where a magnetization M_b points out the bar. The magnetization M_b is assumed to be constant over the whole bar magnet and parallel with the length axis (the x-axis). According to Eq. 2.8 there is a surface charge $\pm\rho_s$ at the poles of the magnet

$$\rho_s = -\vec{\nabla} \cdot \vec{M}|_{\text{on surface}} = -M_x \tag{A.6}$$

To simplify the calculations for the magnetic induction $\vec{B}$, a very simple model is constructed. In this model the poles of a magnetized object are presented as point charges, so in total there are two opposite point charges, a dipole. The magnitude of this mathematical magnetic point charge q_m is the magnetic moment m divided by the dipole distance d integrated over the pole surface. Because the distance d is constant, the magnetic point charge q_m is equal to the surface charge ρ_s times the pole area A_p.

$$q_m = \iiint_V \rho_m \, dV = \iint_S -M_x \, dA = -M_x \, A_p \tag{A.7}$$

Based on this magnetic charge q_m the field can be calculated. The electric field of a point charge is known, using the analogy it can be converted to a magnetic variant.

$$\vec{E} = \frac{1}{4\pi} \frac{1}{\epsilon_0} \frac{q_e}{r^2} \vec{e_r} \Rightarrow \vec{B} = \frac{1}{4\pi} \mu_0 \frac{q_m}{r^2} \vec{e_r} \tag{A.8}$$

When the two previous equations are combined, a rather simple equation can be derived for the magnetic induction $\vec{B}$ in free air, in case of a simple magnetized object

$$\vec{B}_{air} = \frac{1}{4\pi} \mu_0 \frac{q_m}{r^2} \vec{e_r} = \frac{4\pi 10^{-7}}{4\pi} \frac{q_m}{r^2} \vec{e_r} = \frac{-M_x \, A_p \, 10^{-7}}{r^2} \vec{e_r} \tag{A.9}$$

The two magnetic fields of the poles can be added to make an estimation for the whole field of the dipole (superposition principle) which is shown in Figure A.5.

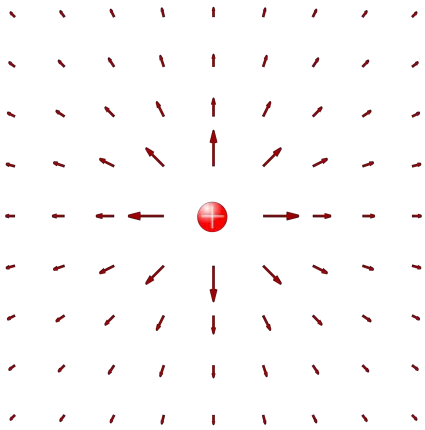

Figure A.4: The electric field of a point charge.

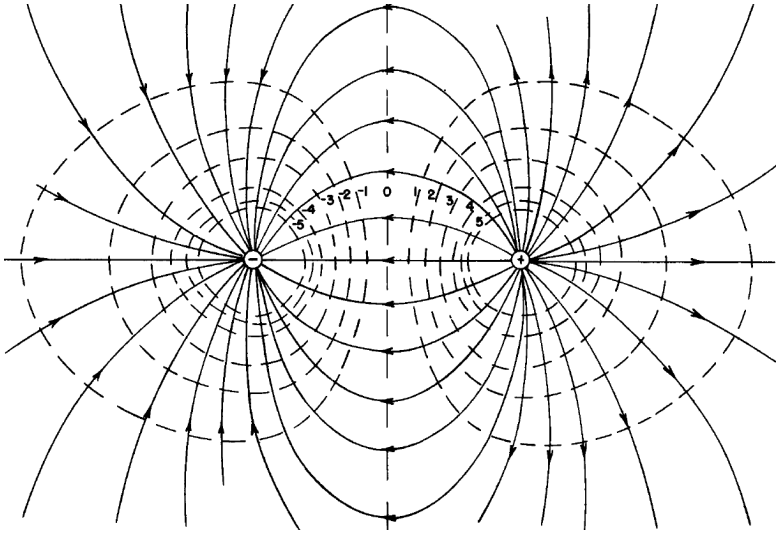

Figure A.5: The field lines and equipotentials for two equal and opposite point charges for a object with a certain magnetization in the x-direction ($M_x > 0$). [15]

A.4 Magnetic moment magnetized disk

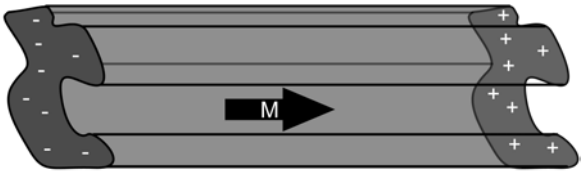

Figure A.6: A random magnetized object with flat pole surfaces.

In Figure A.6 is a uniform magnetized object shown with a flat pole surfaces A_p. The magnetic charge q_m can be calculated by multiplying this magnetization by the surface area, as shown in Eq. A.7. The magnetic field produced by this magnetized object can be calculated by filling in the area in Eq. A.9. For a disk which is magnetized in plane, like shown in Figure A.7, it is more complicated to calculate the magnetic moment m. To do this all the magnetic moment has to be integrated over the surface of the disk. After that a effective magnetic charge can be calculated by choosing a certain distance. This way the field is approximated by a dipole.

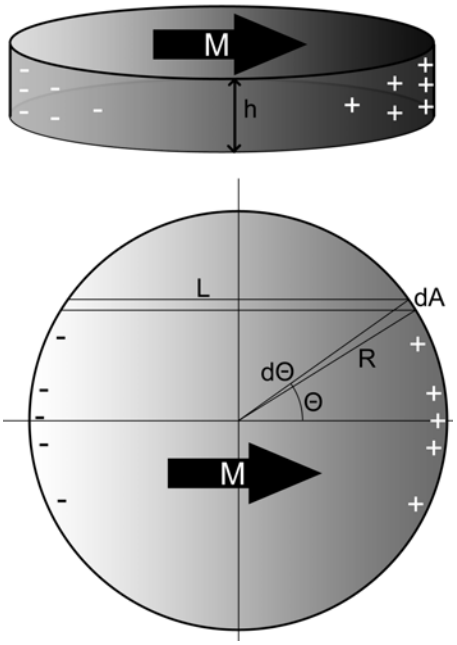

Figure A.7: A in plane magnetized disk.

To calculate the total magnetic moment m, the symbols of Figure A.7 are used. On a certain surface $\mathrm{d}A$ there is a surface charge $\mathrm{d}\rho_s$ present. The surface size is equal to the length of the arc ($\mathrm{d}\Theta\ R$) times the height (h). The surface charge is equal to the magnetization (M) times a cosine of the angle ($\cos(\Theta)$).

$$\mathrm{d}\rho_s = \mathrm{d}A\ \sigma(\Theta) = \mathrm{d}A\ M\ \cos(\Theta) = M\ \cos(\Theta)\ h\ R\ \mathrm{d}\Theta \tag{A.10}$$

Each positive magnetic charge has a negative counter charge on the other side. The magnetic moment $\mathrm{d}m$ is therefore the magnetic charge $\mathrm{d}\rho_s$ times the charge distance L.

$$\mathrm{d}m = \mathrm{d}\rho_s\ L = \mathrm{d}\rho_s\ 2\ R\ \cos(\Theta) = 2\ M\ h\ R^2\ \cos^2(\Theta)\mathrm{d}\Theta \tag{A.11}$$

From this the total magnetic moment m (in ampere square meter $A\ m^2$) can be calculated by integrating over all angles: from $\frac{-\pi}{2}$ to $\frac{\pi}{2}$.

$$m = 2\ M\ h\ R^2 \int_{\pi/2}^{-\pi/2} \cos^2(\Theta)\mathrm{d}\Theta = M\ h\ R^2\ \pi \tag{A.12}$$

In this equation it can be seen that the magnetic moment m is also equal to the volume of the disk times the magnetization M. The most charge is most left and right of the disk, like shown in Figure A.7. The effective magnetic dipole charge q_m can be calculated if the assumption is made that the distance d is equal to two times the radius

$$q_m = \frac{m}{d} = \frac{m}{2\ R} = M\ h\ R\ \pi\ \tfrac{1}{2} \tag{A.13}$$

A.5 Near-field force bead

$$\vec{H} = \frac{1}{2\ \pi} \int_{all\ \rho_s} \frac{\rho_s}{r_{12}}\ \vec{e}_{r_{12}}\ \mathrm{d}A \tag{A.14}$$

The part magnetic charge of the disk which interacts with the sphere is also assumed to be uniform (2d calculation) and is called l_d. The value of this variable will be discussed later. The vector $\vec{r}_1$ is the vector to a certain place in space (x_1, y_1) where the magnetic field is calculated. The vector $\vec{r}_2$ is the vector which points to the place where the magnetic charge is located $(0, y_2)$. Subtracting these two vectors gives the vector $\vec{r}_{12}$ which points from the magnetic charge to a certain place $(x_1, y_1 - y_2)$. To calculate the magnetic field $\vec{H}$ the two components are calculated separately.

$$H_x = \frac{\rho_s}{2\ \pi} \int_0^h \frac{x_1}{x_1^2 + (y_1 - y2)^2}\mathrm{d}y_2 \tag{A.15}$$

$$H_y = \frac{\rho_s}{2\ \pi} \int_0^h \frac{(y_1 - y2)}{x_1^2 + (y_1 - y2)^2}\mathrm{d}y_2 \tag{A.16}$$

The solution to these two integrals can be evaluated with some calculus, this gives the following expression for the magnetic field:

$$H_x = \frac{\rho_s}{2\ \pi} \left(\arctan\left(\frac{y_1}{x_1}\right) - \arctan\left(\frac{y_1 - h}{x_1}\right) \right) \tag{A.17}$$

$$H_y = \frac{\rho_s}{2\ \pi} \frac{1}{2} \left(\ln\left(x_1^2 + y_1^2\right) - \ln\left((h - y_1)^2 + x_1^2\right) \right) \tag{A.18}$$

This solution is plotted in Figure A.8. Close to the sheet, so for very small x_1, the magnetic field in the x-direction H_x is equal to the surface charge divided by two ($\frac{\rho_s}{2}$). This is equal to the field for a infinite plate with a certain surface charge ρ_s.

The force on a magnetic charge can be calculated by multiplying the charge with the magnetic field (see Eq. 2.9). To calculate the force on a sheet of charge, the force on each segment of charge has to be calculated. Since the surface charge ρ_s is uniform assumed over the second sheet and the system is symmetric, the force in the x-direction (F_x) is zero. For the force in the y-direction the magnetic field has to be integrated over the line and could then be multiplied with the surface charge.

$$\begin{aligned} F_y = \mu_0\ l_d \int_{-h/2}^{h/2} -\rho_s\ H_y(x1, y2)\mathrm{d}x|_{y_1=0} &= -\rho_s\ \mu_0\ l_d \int_{-h/2}^{h/2} H_y(x_1, y_1)\mathrm{d}x|_{y_1=0} \\ &= \frac{-\mu_0\ \rho_s^2\ h\ l_d}{2\ \pi} \left(2\ \arctan\left(\frac{1}{2}\right) + \frac{1}{2}\ \ln(5) \right) \approx \frac{\mu_0\ \rho_s^2\ h\ l_d}{2\ \pi}\ 1.73 \end{aligned} \tag{A.19}$$

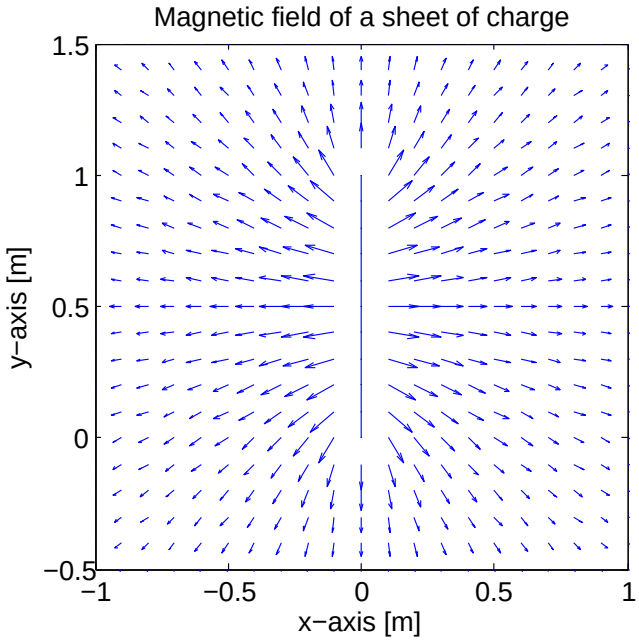

Figure A.8: The calculated magnetic field of a sheet of charge.

The surface charge ρ_s is equal to the saturation magnetization of the disk. The equation for the attraction force becomes then the quite simple expression:

$$F_y = \frac{\mu_0 \ M_s^2 \ h \ l_d}{2 \ \pi} \ 1.73 \tag{A.20}$$

A.6 Magnetic field wire and solenoid

A.6.1 Current carrying wire

To model the magnetic problem, static analyses will be performed. This means that only static or slow changes of the magnetic are considered, so that the derivative with respect to time is zero or negligible small. Suppose the simple case of a current carrying wire. The assumption of a uniform current density through the wire is made. Based on this the magnetic induction $\vec{B}$ can be calculated. We start with the Maxwell's equation for the rotation of the magnetic field $\vec{B}$. This is equal to the magnetic permeability μ_0 multiplied by the current density $\vec{J}$.

$$\vec{\nabla} \times \vec{B} = \mu_0 \ \vec{J} \tag{A.21}$$

$$\vec{\nabla} \cdot \vec{B} = 0 \tag{A.22}$$

The first equation relates the curl (or rotation) of the magnetic field to the current density. The second equation means that the field lines follow closed loops, and that there are no magnetic point sources.

Stokes' theorem says that the integral around any closed path of any vector field is equal to the surface integral of the normal component of the curl of the vector [15, page 13-4]. If this theorem for the magnetic field vector is applied and using the symbols as shown in Figure A.9 this gives

$$\oint_\Gamma \vec{B} \cdot d\vec{s} = \int_S (\vec{\nabla} \times \vec{B}) \cdot \vec{n} \ dS \tag{A.23}$$

When previous equation is combined with Eq. A.21 this gives

$$\oint_\Gamma \vec{B} \cdot d\vec{s} = \mu_0 \int_S \vec{J} \cdot \vec{n} \ dS \tag{A.24}$$

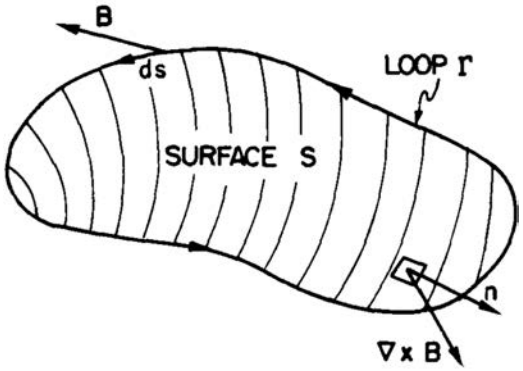

Figure A.9: The line integral of the tangential component of the magnetic field is equal to the surface integral of the normal component of the curl of the magnetic field [15].

From this equation the magnetic field inside and outside a round wire can be derived. For the magnetic field outside the wire, the boundary Γ becomes a circle that is outside the wire, which has the same center as the wire. The current density is only present inside the wire. If we integrate over all the current density J in the wire this gives the current I which flows through the wire.

$$B_{outside} \cdot 2 \cdot \pi \cdot r = \mu_0 \cdot J \cdot \pi \cdot R_0^2 = \mu_0 \cdot I \tag{A.25}$$

Here is r the distance from the center of the wire and R_0 the radius of the wire. This equation can be rewritten to an expression for the magnitude of the magnetic field outside the round wire.

$$B_{outside} = \frac{\mu_0 \cdot I}{2 \cdot \pi \cdot r} \tag{A.26}$$

The strength of the magnetic field drops off with $1/r$, the distance from the center of the wire.

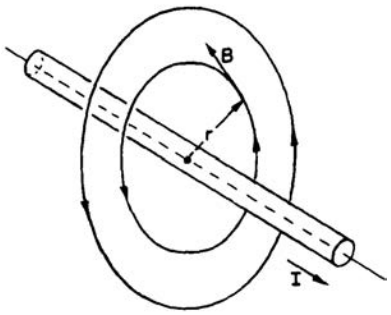

Figure A.10: The magnetic field outside of a long wire [15].

In Figure A.10 can be seen that $\vec{B}$ is at right angles to both $\vec{I}$ and $\vec{r}$. Therefore the magnetic field becomes

$$\vec{B}_{outside} = \frac{\mu_0}{2 \cdot \pi} \frac{\vec{I} \times \vec{e_r}}{r} = \frac{\mu_0}{2 \cdot \pi} \frac{\vec{I} \times \vec{r}}{r^2} \tag{A.27}$$

So the magnetic field is always at right angles to $\vec{I}$ and $\vec{r}$, the magnitude is proportional with the current I and it drops with $1/r$. [15]

A.6.2 Long solenoid

The magnetic field of a long solenoid can be calculated in a similar way. In order to handle the direction of the magnetic field a iron core is inserted, which is being magnetized. This is calculating by evaluating the magnetic field $\vec{H}$, which can be multiplied with the permeability in case of linear media (see Eq. 2.6). Iron is a ferromagnetic material, this will be explained in Section A.2. The consequence is that iron is no linear media, which makes calculating the response of these materials quite complicated. To make very rough calculations possible the assumption of small magnetic fields will be made, this means that the relative permeability can be approximated with a linear constant μ_r (see also Figure 2.8). The permeability of ordinary irons is typically from several thousand to lower values for higher magnetic fields. [15]

In matter holds, in a static situation, the following equation

$$\vec{\nabla} \times \vec{H} = \vec{J}_f \tag{A.28}$$

Here is J_f the free current, this free current might flow through wires embedded in the magnetized substance or, if the material is a conductor, through the material itself. In common, the total current $\vec{J}$ can be split into two parts: the bound current and the free current.

$$\vec{J} = \vec{J}_b + \vec{J}_f \tag{A.29}$$

The two separate currents parts have a different meaning. The free current is there because somebody hooked up a wire to a battery, it involves actual transport of charge. The bound current is there because of magnetization, it results from the addition of many aligned atomic dipoles. According to Ampère's law (for static analyses) each of these currents relates to another field. The relation between the magnetic induction, magnetization and the magnetic field from Eq. 2.4 can be rewritten to an equation with three times Ampère's law

$$\frac{1}{\mu_0}(\vec{\nabla} \times \vec{B}) = \vec{J} = \vec{J}_b + \vec{J}_f = \vec{\nabla} \times \vec{M} + \vec{\nabla} \times \vec{H} \tag{A.30}$$

So the bound current relates to the magnetization $\vec{M}$, the free current to the magnetic field $\vec{H}$ and the total current to the magnetic induction $\vec{B}$.

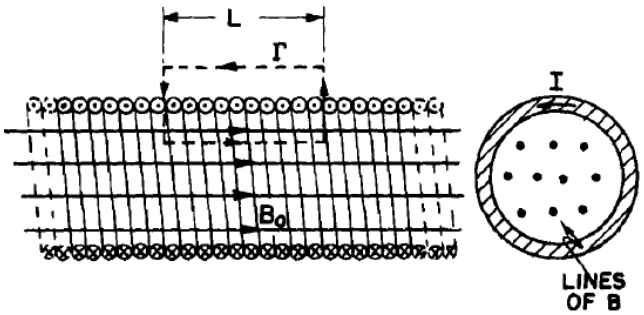

Figure A.11: The magnetic field of a long solenoid. [15]

Applying Stokes' theorem to Ampère's law for the magnetic field $\vec{H}$, shown Eq. A.28, the following equation is obtained

$$\oint_\Gamma \vec{H} \cdot d\mathbf{s} = \int_S \vec{J_f} \cdot n \; dS \tag{A.31}$$

On the left-hand side the magnetic field $\vec{H}$ is integrated over the contour Γ. This contour goes the distance L inside the solenoid, where the field is a certain value H. Then it goes at

right angles with the field, and outside the solenoid is the field zero or negligible. In the surface S enclosed by the contour Γ, there are N turns of the solenoid. From this follows that the turn density times the current is equal the magnetic field strength H.

$$H \cdot L = I \cdot N \tag{A.32}$$

This can be rewritten an expression for the magnetic field

$$H = \frac{N \cdot I}{L} \tag{A.33}$$

In a linear media can this be written to the magnetic induction B (see Eq. 2.6) and to the magnetization M (see Eq. 2.5) with the magnetic permeability μ or the magnetic susceptibility χ_m.

A.7 Quadrupole gap field strength

The magnetomotive force MMF, equal to number of turns N times the current I, can be seen as a voltage V_{eq}, the magnetic flux Φ_B as a current I_{eq} (see also Section A.1.3). From this follows also a magnetic reluctance R_m, which can be seen as a resistance R_{eq}. The magnetic analog of Kirchoff's Law says that the sum of fluxes of a node is zero and that the magnetomovitive forces of a loop are zero. [14, 15] Based on these rules for the equivalent circuit analyses follows the following equation

$$V_{eq} = I_{eq} \cdot R_{eq1} + I_{eq} \cdot R_{eq2} \Rightarrow MMF = \Phi_B \cdot R_{m1} + \Phi_B \cdot R_{m2} \tag{A.34}$$

The source force MMF is the number of turns of the solenoid N times the current through the solenoid I. The magnetic flux Φ_B is equal to the magnetic field B times the cross-sectional area A, assuming a constant magnetic field. The magnetic reluctance R_m is equal to the physical circuit length l divided by the permeability μ and the cross-sectional area A. The magnetic loop of Figure 2.17 can be written as

$$4 \cdot N \cdot I = \phi \cdot R_{core} + \phi \cdot R_{air} \tag{A.35}$$

The magnetomotive force is equal to two times $N \cdot I$ (two solenoids in one half) times two half circuits, these may be added because of symmetry. The resistance of the core will be neglected, since the relative permeability of iron is approximately one thousand. This is allowed when the air gap is not too small, because then R_{air} gets small compared to R_{core}. If all the variables are filled in the previous equation, this gives an expression for the magnetic field in the air gap.

$$4 \cdot N \cdot I = B_g \cdot A_g \cdot \frac{l_g}{\mu_0 \cdot A_g} \tag{A.36}$$

which can be rewritten to an equation for the magnetic field in the gap

$$B_g = \frac{4 \cdot N \cdot I \cdot \mu_0}{l_g} \tag{A.37}$$

A.8 Stokes flow sphere

The velocity components of Stokes flow around a sphere, with velocity u_b along the x-axis, are

$$u_r = u_b \; cos(\theta) \left(1 - \frac{3R_b}{2r} + \frac{R_b^3}{2r^3}\right) \tag{A.38}$$

$$u_\theta = -u_b \; sin(\theta) \left(1 - \frac{3R_b}{4r} - \frac{R_b^3}{4r^3}\right) \tag{A.39}$$

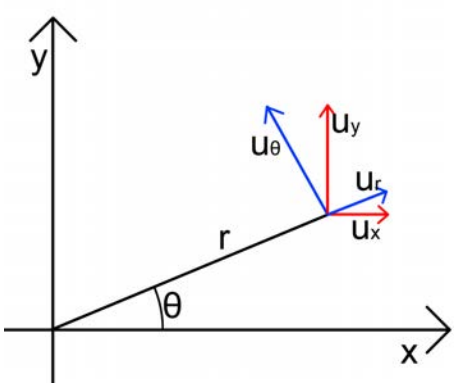

Figure A.12: Velocity vectors in cartesian and polar vector systems.

The two velocity components (u_r, u_θ) are shown in Figure A.12. [25, Page 289-291] Since the channel is rectangular, it is more convenient to perform the integration in the cartesian coordinate system. The polar velocity vector could be converted to cartesian coordinates using the following equations

$$u_x = u_r\ cos(\theta) - u_\theta\ sin(\theta) \tag{A.40}$$
$$u_y = u_r\ sin(\theta) + u_\theta\ cos(\theta) \tag{A.41}$$

where r is the distance from the origin

$$r = \sqrt{x^2 + y^2 + z^2} \tag{A.42}$$

and θ is the angle to the x-axis (see also Figure A.12)

$$\theta = \text{atan2}(\sqrt{y^2 + z^2}, x) \tag{A.43}$$

The atan2 function with two arguments, the x- and the y-value. The result is the angle in the range of $(-\pi, \pi]$. Hence holds for the cartesian velocity components

$$u_x = u_b - u_b\ cos^2(\theta)\left(1 - \frac{3R}{2r} + \frac{R^3}{2r^3}\right) + u_b\ sin^2(\theta)\left(1 - \frac{3R}{4r} - \frac{R^3}{4r^3}\right) \tag{A.44}$$
$$u_y = u_b\ sin(2\theta)\ \frac{3\ a^3 - 3\ a\ r^2}{8r^3} \tag{A.45}$$

Appendix B

Mask design

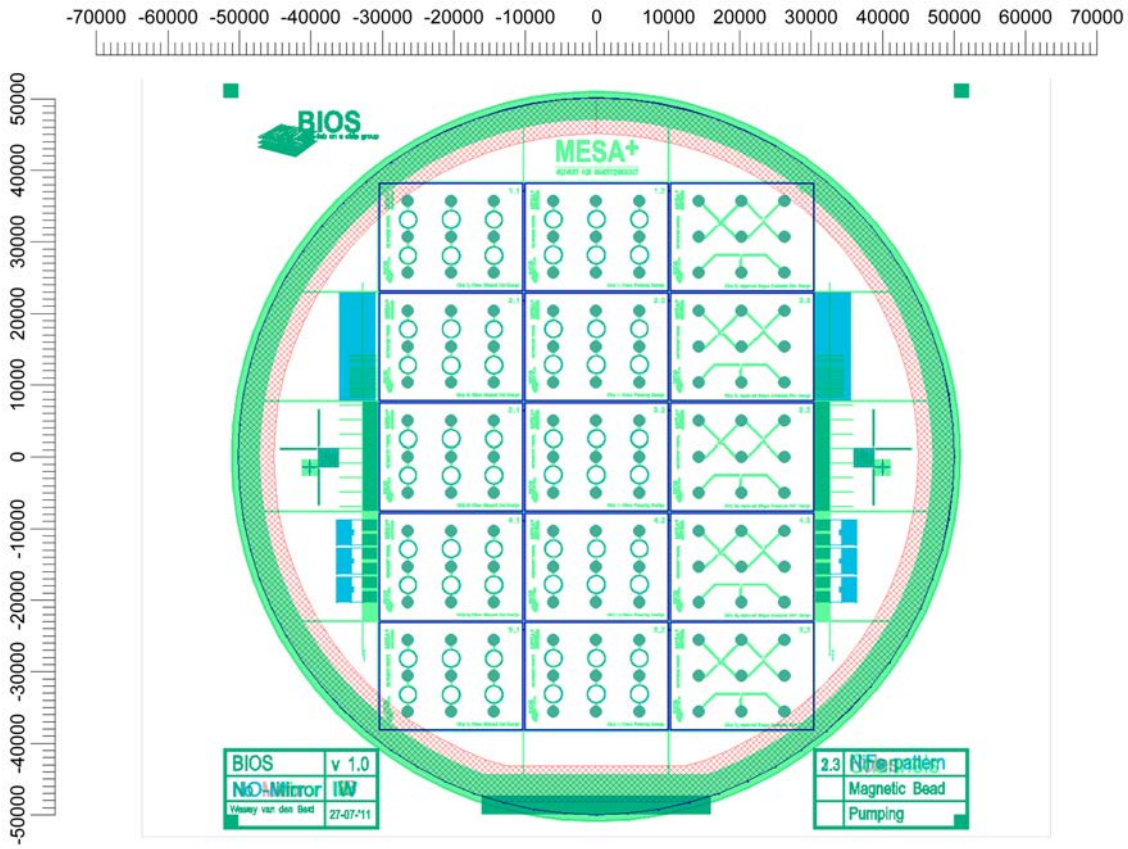

Figure B.1: First wafer design.

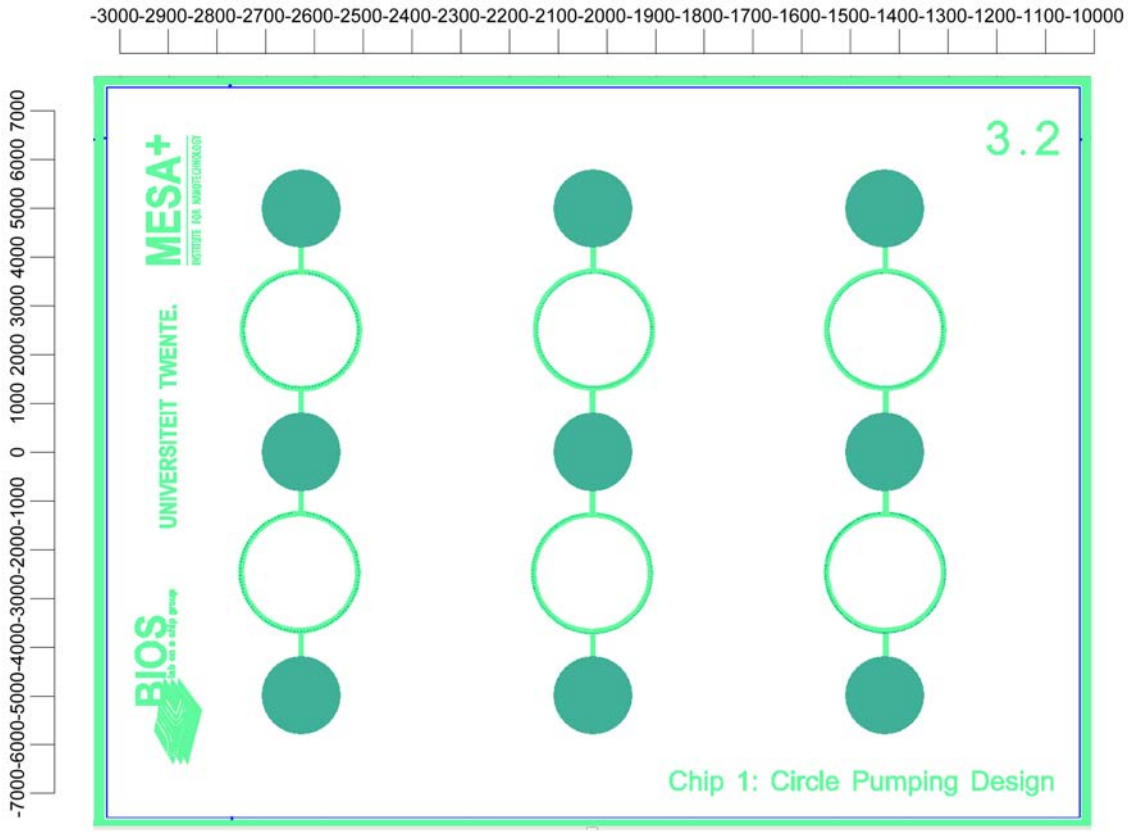

Figure B.2: Type 1 chip design of first wafer design.

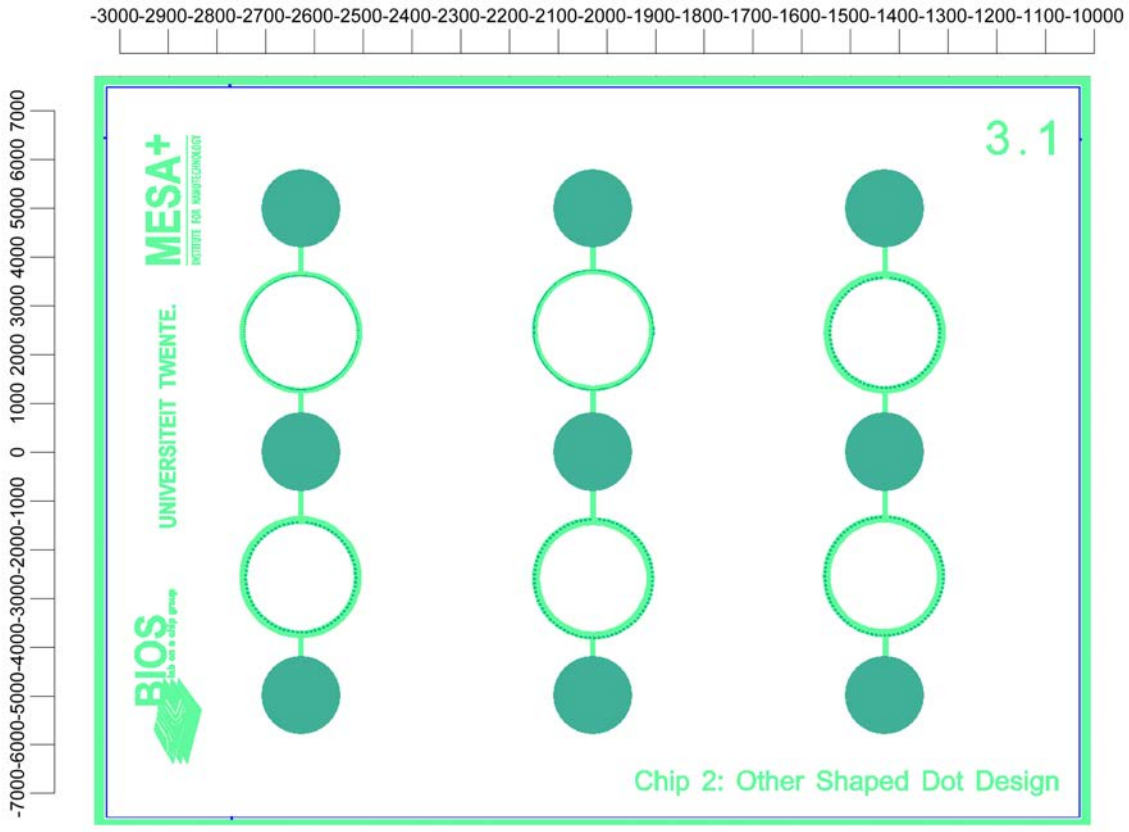

Figure B.3: Type 2 chip design of first wafer design.

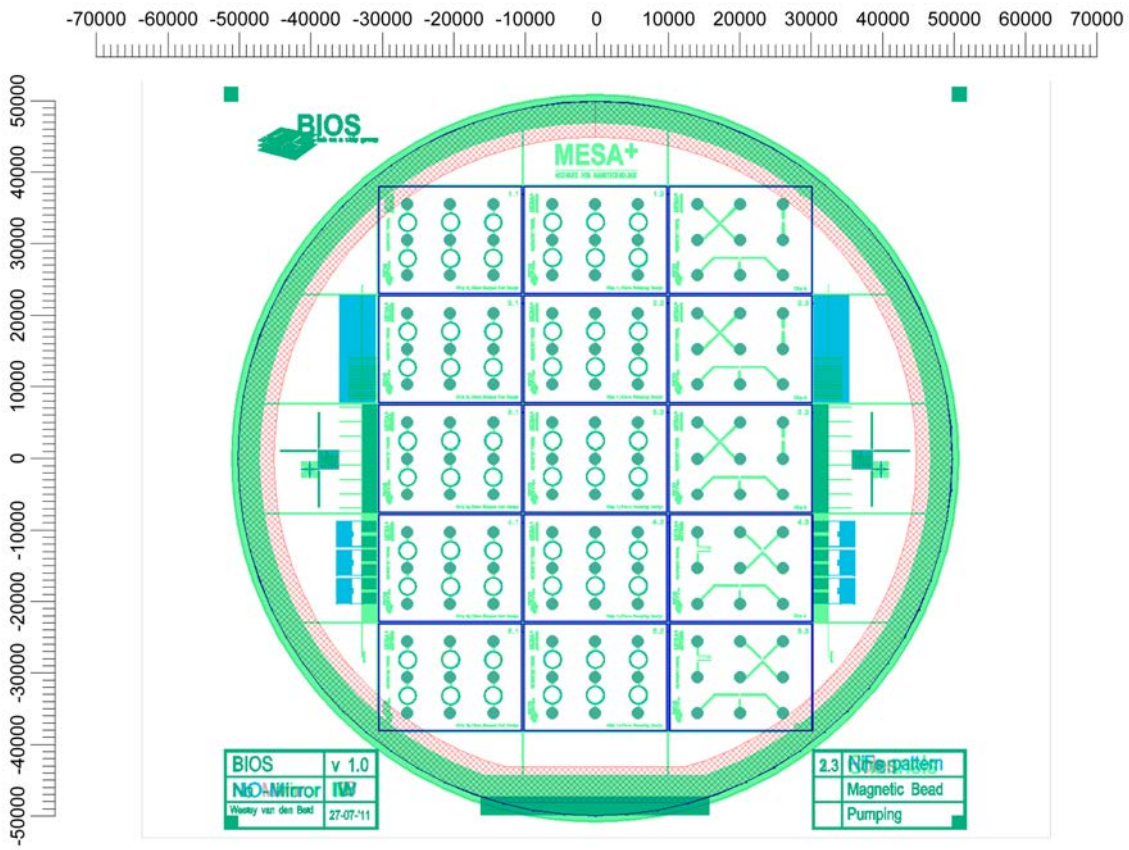

Figure B.4: Second wafer design.

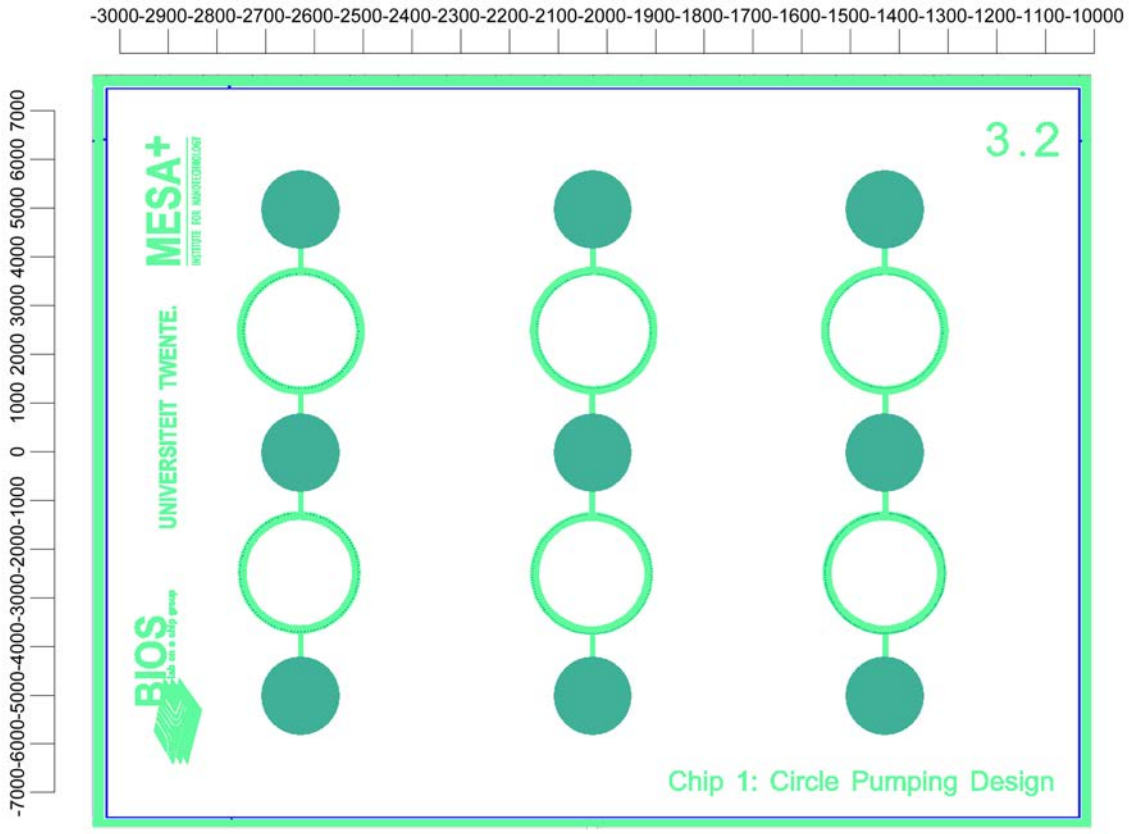

Figure B.5: Type 1 chip design of second wafer design.

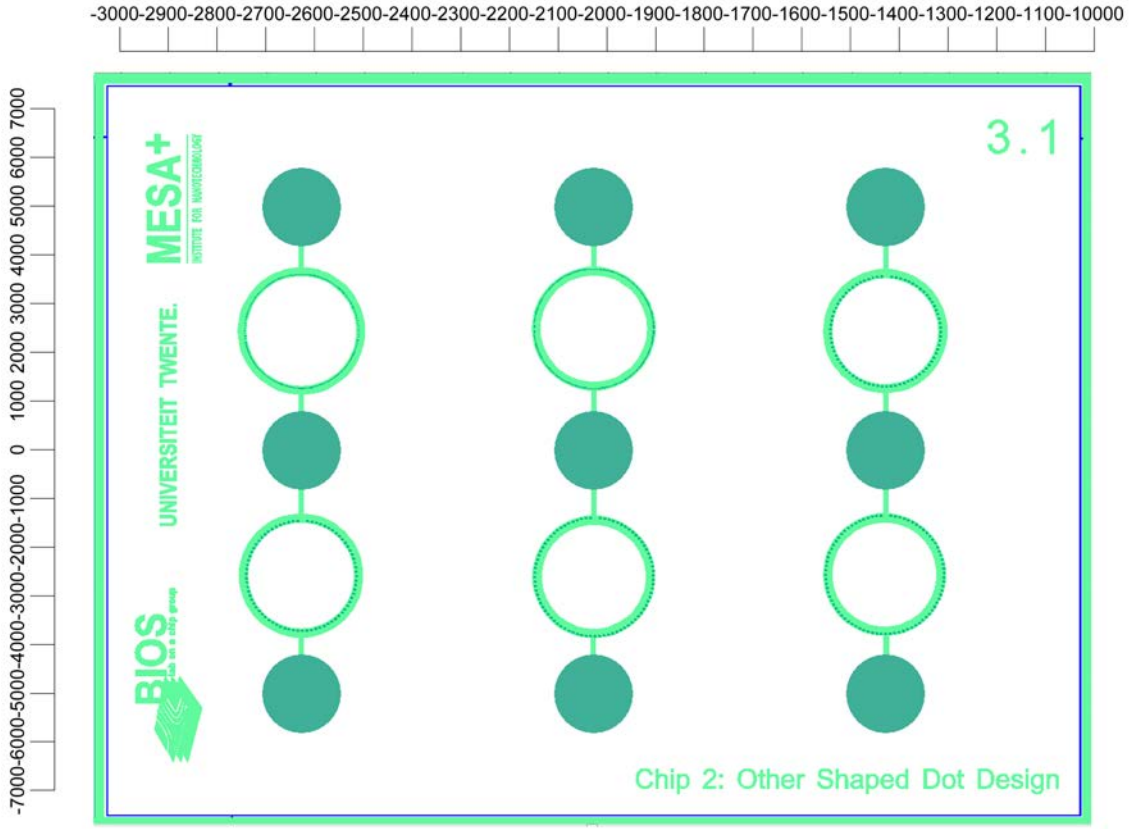

Figure B.6: Type 2 chip design of second wafer design.

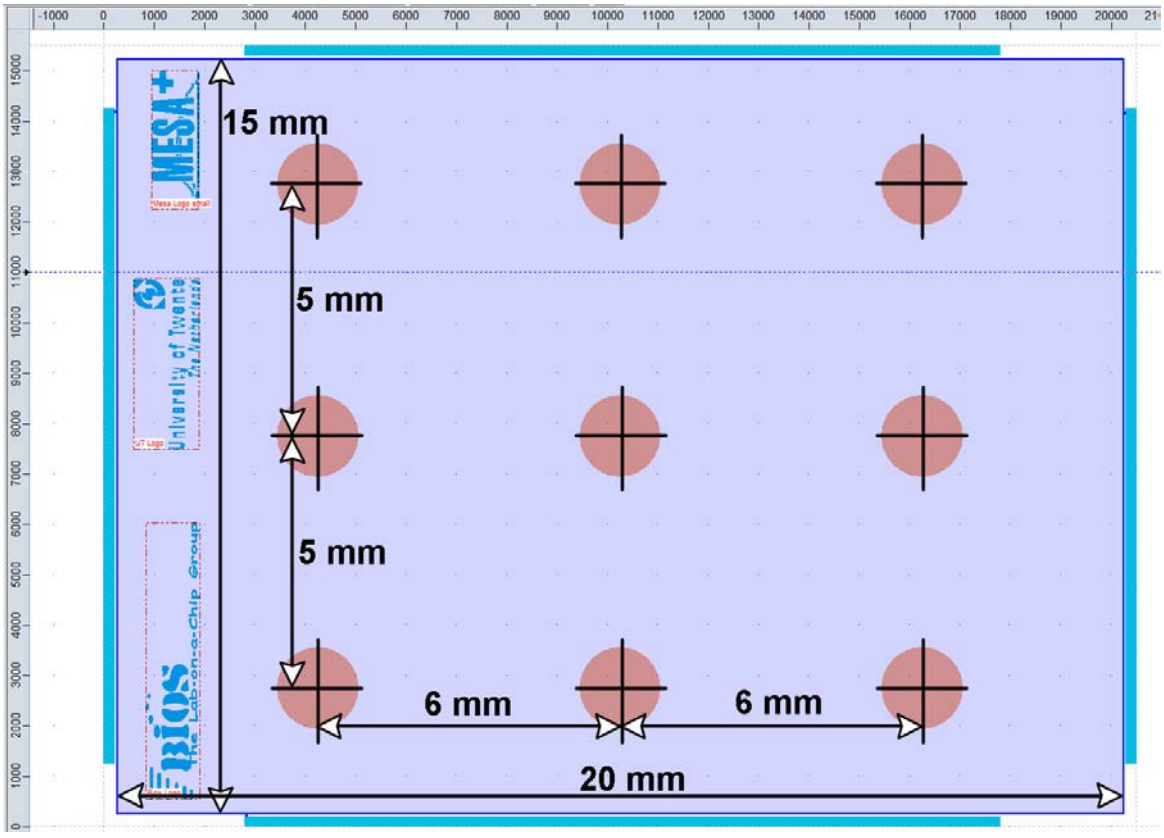

Figure B.7: Chip size with powderblasted holes for the loading in- and outlets.

Appendix C

Manufacturing

C.1 Process A

Glass or silicon on glass wafer with the permalloy pattern on the bottom of the channel patterned using lift-off.

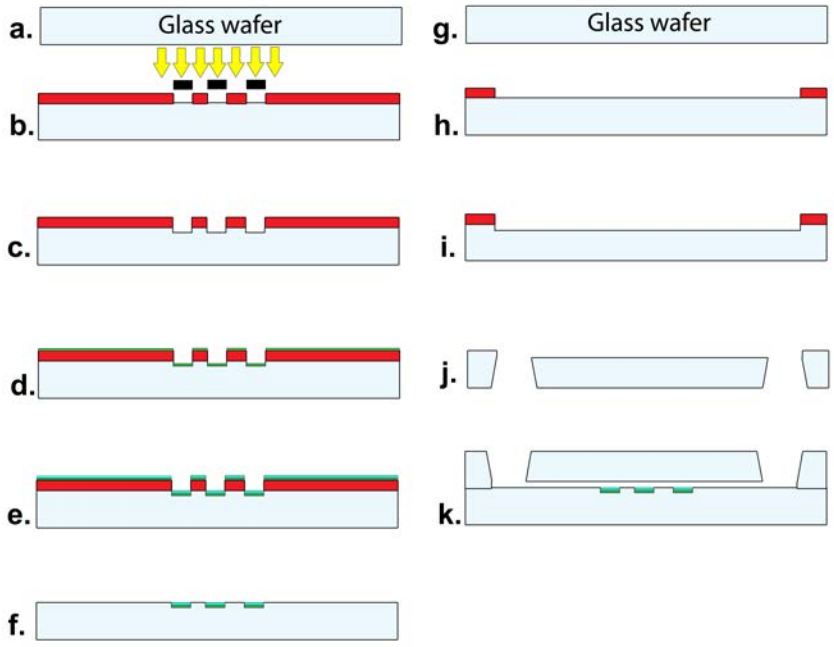

Figure C.1: Glass bonded on glass with permalloy pattern on bottom.

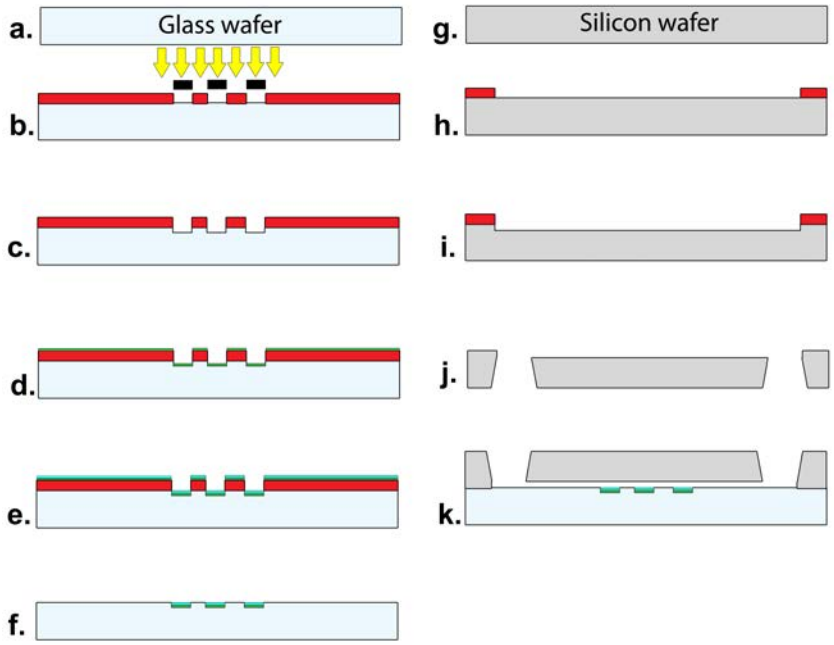

Figure C.2: Silicon bonded on glass with permalloy pattern on bottom.

C.2 Process B

Silicon on glass with permalloy pattern on the top of the channel patterned using wet etching

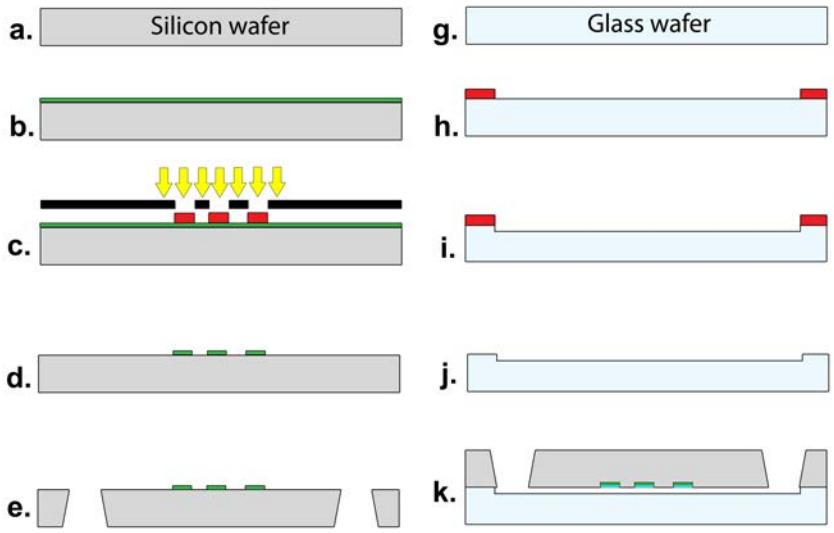

Figure C.3: Silicon bonded on glass with permalloy pattern on top.

C.3 Wafer information

General		Wafer type		Permalloy process			Extra layers		Channel and bonding	
No.	Date	Bottom	Top	Array wafer	Thickness[a]	Method	Adhesive layer	Top layer	Channel depth	Bonding type
1	12-9-2011	Borofloat[b]	-	Bottom	500nm	Deposition	-	-	-	-
2	19-10-2011	Borofloat	-	Bottom	132nm	Sputtering[c]	-	-	-	-
3	11-11-2011	Borofloat	Borofloat	Bottom	100nm	Sputtering and lift-off	-	-	15 μm anisotropic[d]	fusion 625 °C
4	18-11-2011	Borofloat	Silicon	Bottom	120nm	Sputtering and lift-off	-	-	15 μm anisotropic	anodic 425 °C[e]
5	28-11-2011	Borofloat	Silicon	Bottom	90nm	Sputtering and lift-off	-	30nm Pt	15 μm anisotropic	anodic 425 °C
6	17-2-2012	Borofloat	Silicon	Top	480nm	Sputtering and wet etching	20nm Cr/Ta	-	40 μm isotropic	anodic 425 °C
7	24-2-2012	Borofloat	Silicon	Top	460nm	Sputtering and wet etching	20nm Cr/Ta	-	40 μm isotropic	-
8	2-3-2012	Borofloat	Silicon	Top	295nm	Sputtering and wet etching	20nm Cr/Ta	-	40 μm isotropic	-

Table C.1: Wafer information with different manufacture parameters.

[a]The uniformity of the permalloy film (NiFe) is 10 %
[b]The borofloat and silicon wafers have a thickness of 500 μm
[c]Sputtering is performed with TCOater
[d]DRIE-process is used for anisotropic etching
[e]All anodic bonding is performed in vacuum

C.4 Chip assembly

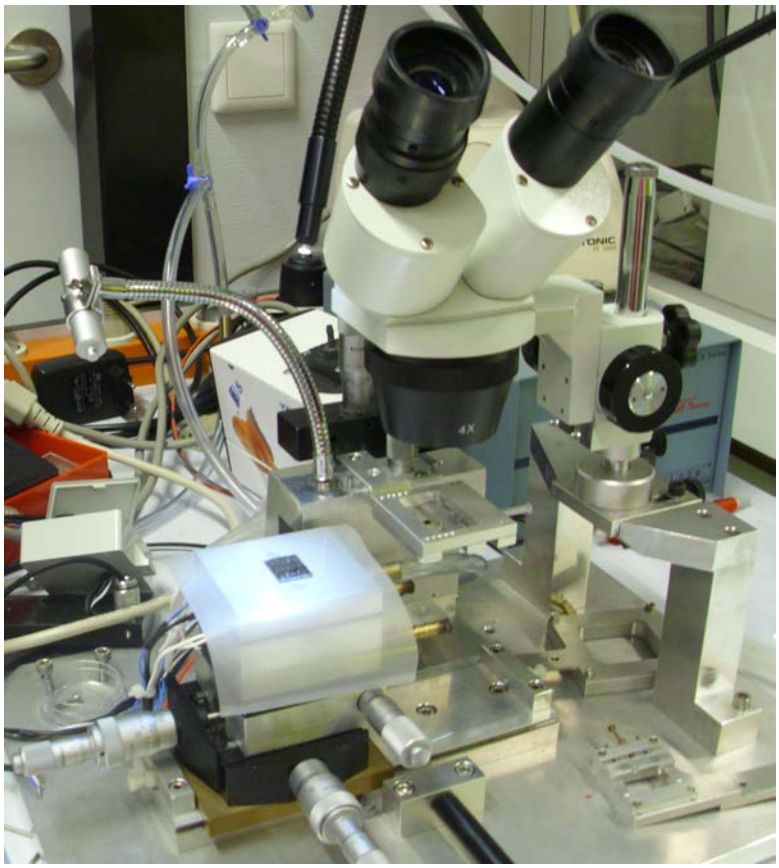

Figure C.4: Chip aligner with silicon side of chip on foil.

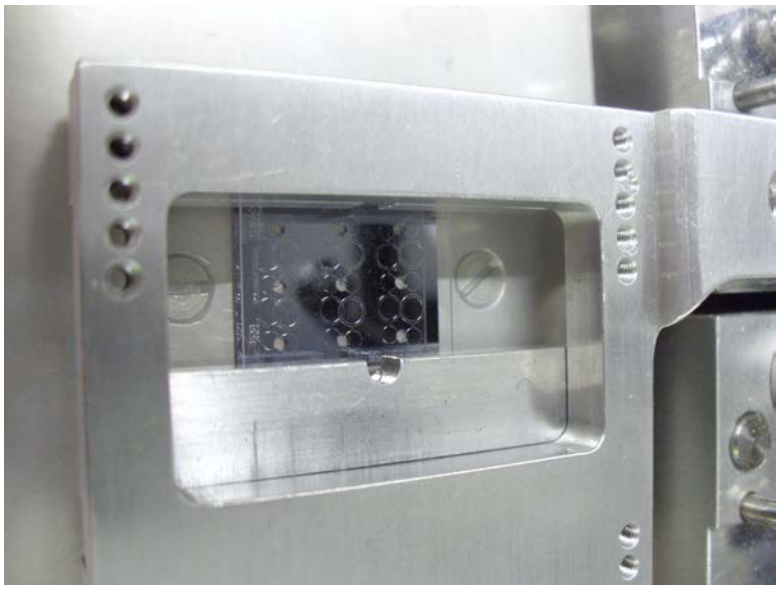

Figure C.5: Chip parts aligned in chip aligner.

Appendix D

Pictures of VSM

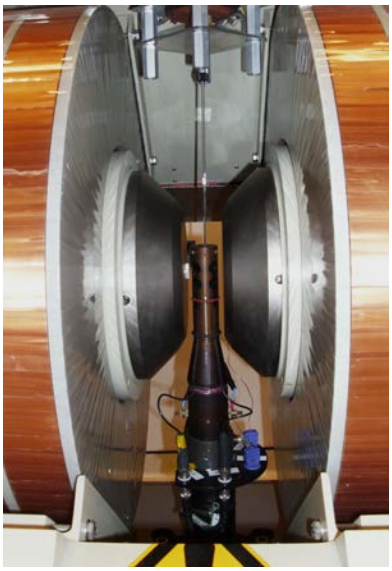

Figure D.1: Close-up of the sample in the pickup coils between the two electromagnets of the VSM.

Figure D.2: VSM control Close-up of the sample in the pickup coils between the two electromagnets of the VSM.

Appendix E

H-bridge circuit

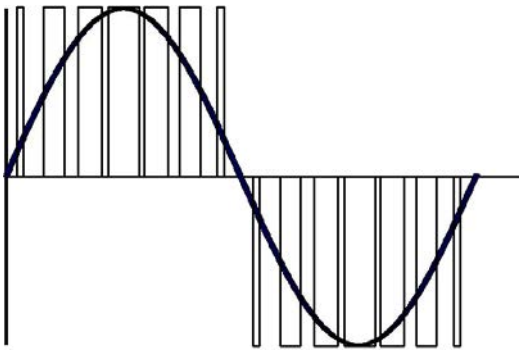

Figure E.1: Pulse Width Modulated sinusoidal signal, showing the amplification principle [45].

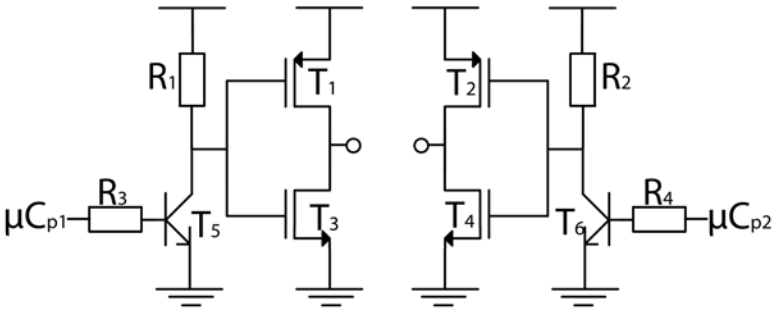

Figure E.2: The used H-bridge circuit. On the left and the right the control signals of the microcontroller are connected, in the middle the connections for the solenoid are drawn.

Designator	Description
R1 = R2	500 Ω
R3 = R4	220 Ω
T1 = T2	PMOS, IRF9530NPbF
T3 = T4	NMOS, IRF530NPbF
T5 = T6	NPN, BC550
Vdd	12V PC power supply
Microcontroller	PIC 18F452
Microcontroller supply	5V Voltage regulator ka7805a
Optocouplers	PC017

Table E.1: Bill of Materials for H-Bridge circuit.

Appendix F

Particle tracking script

```
%load video in workspace
video_filename = '5hz disk -500nm 30um16.avi';

video = importdata(video_filename);
video_object = VideoReader(video_filename);
%get video info
video_time = video_object.Duration; %video duration in seconds
fps = video_object.FrameRate; %framerate in frames per second
%analyse video data
video_size = size(video(1,1).cdata)
%optional cropping of video
Xmin = 1; Xmax = video_size(1);
Ymin = 1;  Ymax = video_size(2);
%deterime number of frames of video
video_length = length(video);

%parameters for analysis of the video:
threshold = 0;                      %optional threshold for nois filtering
ana_frame_start = 1;
ana_frame_stop = video_length;
ana_frame_total = ana_frame_stop-ana_frame_start
pk_threshold = 10;                  %peak threshold for particle tracking
max_movement = 4;                   %max movement of a particle, decrease ...
    when
                                    %particle tracking gives
                                    %errors-confusement with different
                                    %particles
frames_found = 5*fps;               %time that a particle is followed in ...
    seconds
cross_size = 0;                     %drawing...
line_width = 2;
line_max_speed = fps*max_movement/0.85*0.4;
colorarray = jet(255); %alternatives: cool, jet, hsv

%add all frames and devide by the number of frames to get an average frame
%of the whole video
image_sum = uint64(zeros(Xmax-Xmin+1,Ymax-Ymin+1));
for frame = 1:video_length
    image_sum = image_sum + ...
        uint64(video(1,frame).cdata(Xmin:Xmax,Ymin:Ymax));
end
image_avg = uint8(image_sum/video_length);

%analysis of the video with given parameters
for ana_frame = ana_frame_start:ana_frame_stop
    %the progress is displayed in the command window
    progress = (ana_frame-ana_frame_start)/ana_frame_total*100
```

```
45
46      %the frame is substracted from the earlier calculated average frame
47      substract_pic = ...
48      (imsubtract(image_avg,video(1,ana_frame).cdata(Xmin:Xmax,Ymin:Ymax)))...
49      -threshold;
50
51      %the peaks are found with the function below
52      pk = pkfnd(substract_pic,pk_threshold,5);
53
54      %the peaks are more precisely determined in double format
55      cnt = cntrd(cast(substract_pic,'double'),pk,5);
56      pk = cnt(:,1:2);
57
58      %the peak data is saved in the array pk_time
59      pk_size = size(pk);
60      if ana_frame == ana_frame_start
61          pk_time = [pk ones(pk_size(1),1).*ana_frame];
62      else
63          %the found peaks are collected in the matrix pk_time
64          pk_time = vertcat(pk_time,[pk ones(pk_size(1),1).*ana_frame]);
65      end
66  end
67
68  %the tracking of the peaks is performed in this function
69  tr = track(pk_time,max_movement);
70  %output format: X_data, Y_data, Frame_number, Particle_id
71
72  %the number of particles which are found with the tracking function
73  particles_found = max(tr(:,4));
74
75  %==================================
76  % draw figure
77  %==================================
78  %start drawing the found particle data
79
80  close all
81  figure %create new figure
82  %plot the last substract_pic as a background for the particle data
83  colormap(video(1,1).colormap)
84  image(video(1,frame).cdata(Xmin:Xmax,Ymin:Ymax))
85
86  distance_counter = 1;
87  speed_array = [0];
88  %loop through all the found particles
89  for b=1:particles_found
90      %filter on the particle_id == b
91      tr_found = find(tr(:,4) == b);
92      %deterime howlong this specific particle is tracked, if this is long
93      %enough then plot the data of this particle
94      if length(tr_found) ≥ frames_found;
95          %determine the total travelled distance
96          ΔX = tr(tr_found(1),1)-tr(tr_found(length(tr_found)),1);
97          ΔY = tr(tr_found(1),2)-tr(tr_found(length(tr_found)),2);
98          totdistance = sqrt(ΔX^2+ΔY^2);
99          %filter the moving particles for the drawing sequence
100         if totdistance > 5
101             speed = 0;
102             %loop through the indexes which are found in tr_found
103             for i=1:length(tr_found)-1
104                 %calculate a moving average for the speed color
105                 for j=1:5
106                     ΔX = tr(tr_found(i),1)...
```

```
107                     -tr(tr_found(min(i+j,length(tr_found))),1);
108                     ΔY = tr(tr_found(i),2)...
109                     -tr(tr_found(min(i+j,length(tr_found))),2);
110                     distance(j) = sqrt(ΔX^2+ΔY^2)/j;
111                 end
112                 %0.85 pixels/um
113                 speed = fps*mean(distance)/0.85;
114                 clear distance
115                 %select the drawing color
116                 colorvalue = ...
                        colorarray(int16(min(speed/line_max_speed,1)*254)+1,:);
117                 %draw a line between the different coordinates
118                 line([tr(tr_found(i),1) tr(tr_found(i+1),1)],video_size(1)...
119                 -[tr(tr_found(i),2) ...
                        tr(tr_found(i+1),2)],'Color',colorvalue,...
120                 'LineWidth',line_width);
121             end
122         end
123     end
124 end
```